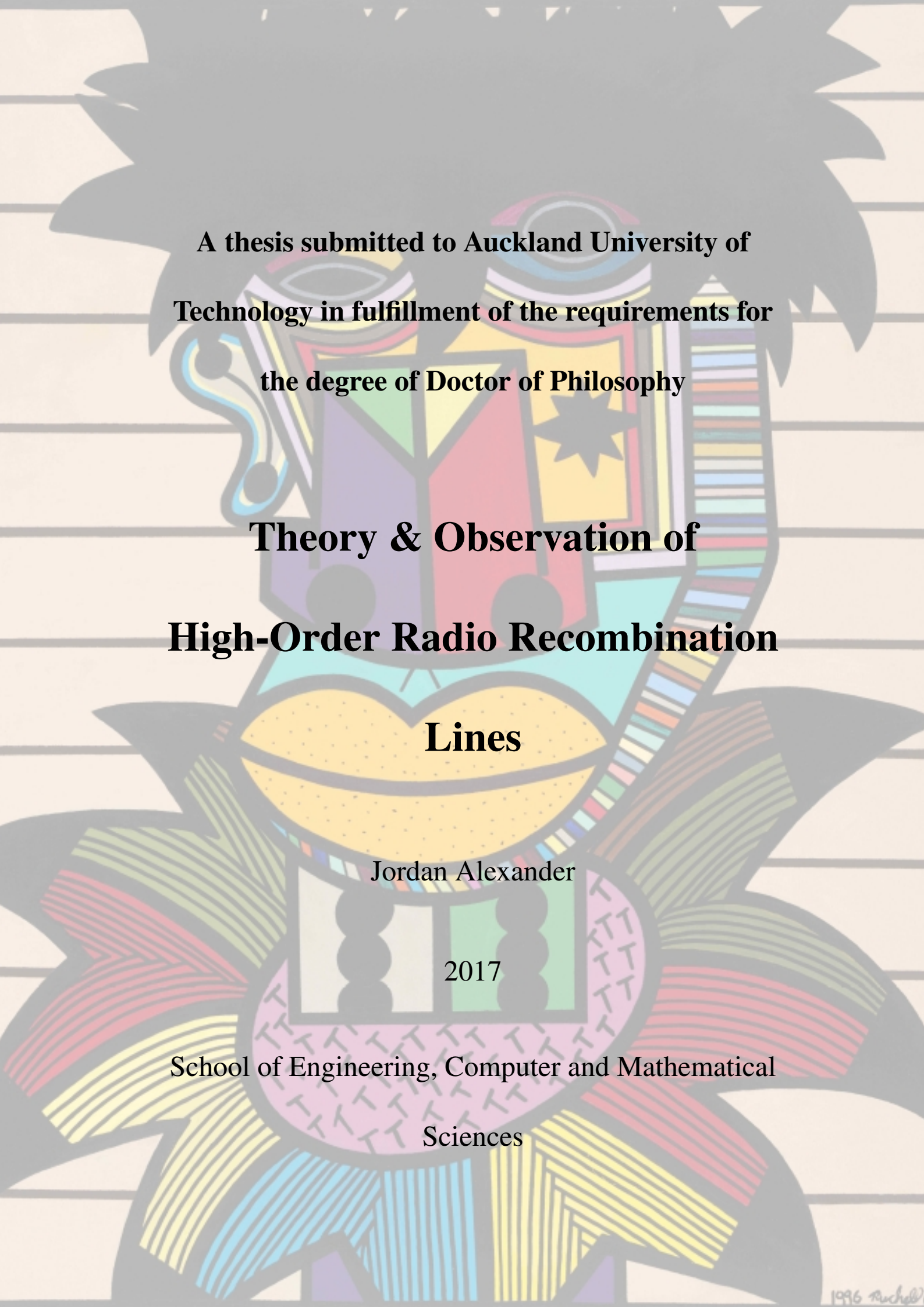

A thesis submitted to Auckland University of Technology in fulfillment of the requirements for the degree of Doctor of Philosophy

# Theory & Observation of High-Order Radio Recombination Lines

Jordan Alexander

2017

School of Engineering, Computer and Mathematical Sciences

# Contents

# Declaration

I hereby declare that this submission is my own work and that, to the best of my knowledge and belief, it contains no material previously published or written by another person (except where explicitly identified in the acknowledgements), nor material which to a substantial extent has been submitted for the award of any other degree or diploma of a university or other institution of higher learning.

# Abstract

This dissertation resolves a mystery in cosmic radio recombination line observations reported by Bell et al. (2000). This is accomplished by rigorously "reverse-engineering" the novel data processing technique they used and through independent observations of high-order RRLs (radio recombination lines) of cosmic origin to test the theory of Stark broadening in plasmas. The findings of this dissertation are summarized in two papers published during the dissertation and reproduced in Chapter 4.

I discovered that the apparent hydrogen RRL narrowing first reported by Bell et al. is an artifact of their data processing. I accomplished this by creating a theoretical model of the multiple FS (frequency shifting) technique, originally developed by Bell (1997), which I then implemented as a computer simulation. This technique copies a spectral line bandpass, shifts it in frequency by an offset, and adds it to the unshifted bandpass. The output of this process is then fed back

to itself multiple times. I then co-created a theoretical model of the Orion nebula which includes mechanisms of spectral line broadening and non-equilibrium thermodynamics effects. This model is used to numerically solve the radiative transfer problem to simulate hydrogen RRLs. These simulated lines are then processed through the multiple FS model, the results of which are called "processed" lines. Finally, I used Monte Carlo simulation to estimate how noise influences the processed line widths and amplitudes.

From these models and simulations, I discovered that multiple FS does not preserve broadening when the original line width is greater than the FS-offset. In this case, I find the processed results manifest the narrowing reported by Bell et al., by reducing broad spectral wings characteristic of Stark broadened RRLs. I also discovered that the S/N of processed lines *reduces* weakly with the number of overlaps as a result of adding *dependent* samples. This means the S/N of processed lines as a function of $\Delta n$ (transition-order), at fixed frequency, decreases faster than for unprocessed lines, such that a given statistical insignificance level is reached more quickly.

Given this analysis, I argue Bell et al.'s $\Delta n > 11$ lines are artifacts of their technique. I conclude that their reported findings, upon re-examination of their novel data processing technique, do not indicate a need to change Stark broadening theory.

I present original observations of high-order RRLs from the Orion nebula to test the theory of Stark broadening in cosmic plasmas. I use a wide 1 GHz bandpass centered at 6 GHz to significantly improve the accuracy of measurements by stacking up to eleven hydrogen RRLs of the same $\Delta n$ and find no evidence of spectral line narrowing. I show that all statistically significant data from my observations and four-sets of previous observations of high-order hydrogen RRLs (Smirnov et al., 1984; Bell et al., 2011) are in agreement and demonstrate how Stark broadening theory is consistent with these observations. I find that Lockman and Brown (1975)'s RRL model of the Orion nebula over a large range of radio frequencies and $\Delta n \leq 2$ requires the addition of small-scale density inhomogeneities (clumps) and turbulence to adequately predict my observed hydrogen RRLs for $\Delta n \leq 5$.

I demonstrate that the power law predicted by electron-impact Stark broadening theory is consistent with the five-sets of high-order hydrogen RRLs analyzed here. My data do not allow distinguishing between two approaches to the cut-off parameters (nearest neighbor versus Debye radius) when predicting line broadening from electron impacts. Specifically, the data does not allow an unambiguous choice between the theoretical results of Griem (1967); Gee et al. (1976) and Watson (2006); Peach (2015). This ambiguity arises from small differences in the radiative transfer nebula model parameters. It is currently impossible to independently determine turbulent velocities and other physical & geomet-

ric parameters of the Orion nebula with enough accuracy to choose between the two predications of electron-impact broadening theory. This situation represents an ill-posed inverse problem that is currently unsolvable (Brown et al., 1978). However, I am able to show that Peach's model for electron-plus-proton impacts significantly deviates from the Lorentz-width trend in my data.

# Dedication

To six wondrous creatures,

named in the order

of their appearance

on this planet:

Babe in the Woods

Perfect Nurse

Sweet Pea

Ninster

Nuggets

Mongoose

# Acknowledgments

It has taken a village to raise this child, as the following acknowledgments attest.

This dissertation would never have begun, nor been successfully completed, without Professor Sergei Gulyaev, my supervisor. From the moment we met, through to the end, there has been scientific symbiosis. For a decade, he has masterfully navigated me through the many rapids and calms of this voyage, finally bringing our ship back to port after many great storms of scientific and personal exploration. I remain, throughout it all, in awe of his deep and methodical approach to all aspects of this life. I will inspire those that follow, as you have inspired me — thank you for everything you said, did not say, did, and did not do. Sergei, you are a lion, quietly roaring.

I thank Morley Bell, the founding father of this dissertation topic. Like adversaries who keep pushing one another to greater heights of performance, Morley has never let up for a moment; as this dissertation goes to print, he is in top-form

pointing out mistakes and what has not been achieved. And for this, I thank him. In the beginning, we sorely needed help to understand his novel data processing technique that, in my opinion, was cryptically explained and sparsely distributed over too many published works. Like a good teacher, he patiently answered my questions, but little more, and even shared some of his original data. With this approach, Sergei and I slowly, ever so slowly, came to understand its mathematical basis, reaching a point where a complete mathematical model was developed and published to accurately account for its known behavior. But like any useful model, it also predicted unexpected behaviors, which turned out to be the beginning of the end for the novel technique when applied to increasingly broadened RRLs . Undaunted, Morley immediately published a paper contradicting our findings, which I found even less convincing, but rightfully suggested new observations are needed to resolve the matter. After doing just that, and finally publishing our results, he remains unconvinced. And so it goes. Once this dissertation is done and covered in dust, I look forward to finally meeting Morley in his native Canada over more than one beer...

I thank Miller Goss and Peter Thomasson for many challenging discussions on the art and science of radio interferometry, and Maxim Voronkov for much help with the complexities of interferometry observations and associated data processing, particularly calibration. I thank the Commonwealth Scientific and Industrial Research Organisation's Astronomy and Space Science for providing

2012 and 2013 observational time on the Australia Telescope Compact Array.

I recognize Professor Dave Westpfahl of the New Mexico Institute of Technology, Socorro, for not only being my first teacher of radio astronomy as a graduate student, but for helping me appreciate, years later, that a radio spectrum is only as good as its passband calibrator when observing with an interferometer.

Tim Natusch is here recognized for his encyclopedic knowledge of and experience in practical radio astronomy, which he patiently shared with me when often seeking his advice. I thank Tim for his persistent support over the years while teaching courses together in physics and astronomy. I recognize Tim's early advocacy in our successful acquisition of physics laboratory equipment and its integration into our courses.

Doctor Alla Shymanska, my second supervisor, has been a source of constant encouragement and belief in me as a fellow scientist in the making. Thank you, Alla, for radiating warmth and joy during our episodic encounters throughout this dissertation.

I hereby recognize the amazing talent and close friend, Mahmoud Mahmoud, a fellow graduate student soon to finish his doctorate on high performance computing in radio astronomy. Together, we have scaled many mountains of thought, plumbed great depths of humanity & its history, debated our philosophies, namely politics & teaching, and shared in many struggles as graduate

students. I thank Mahmoud for joining or taking me on myriad rivers and down twisting rabbit holes. Finally, I thank Mahmoud for his graphic design skills that helped realize my poster reproduced in Figure 4.1.

I thank fellow doctoral student Stuart Weston for his early and successful RRL observational campaigns with the Warkworth 12 m telescope and then later efforts with the ATCA during "duty astronomer" duties, where he offered and then carried-out "green" time RRL observations. Although analysis and results of these observations did not reach this dissertation, they represent a significant period of training that informed my subsequent efforts presented here.

To my postgraduate office mates Asif Rasha and Vicky Liu, I thank you for the experiences we have had together, particularly around solving math, physics and statistics related exercises. We have helped each other in personal ways, too, and for this I am grateful. Seeing you complete your master's degrees at the end of my dissertation has been inspirational.

I thank Patricia Sallis for juggling all matters of bureaucracy throughout the dissertation, particularly organizing travel to observatories, workshops and conferences and keeping me well supplied with staples. Patricia's leadership, during lunch, in solving the daily paper's "code-cracker" and "word wheel" puzzles has been a healthy and fun distraction throughout the dissertation. I thank her for the gentle pushes applied throughout.

Professor Albert Yeap is a rare philosopher in this academic universe who has followed my work with critical interest. That he invited me, years ago, into his graduate seminars on artificial intelligence was all it took and we have benefited ever since. I thank Albert for many inspired and challenging exchanges and look forward to breaking with convention in future collaborations.

Graham Bidois, may your spirit of generosity and love inspire my remaining days in these all too brief moments we call life on this planet — you are greatly missed, taken from us too quickly. You believed in me and alternative approaches, unlike anyone else I know, when it came to my first physics teaching role within AUT's pre-degree program. Under your guidance, we inspired many young minds across cultures through mathematics, physics, food, and music — I continue implementing and evolving these approaches now in degree and pre-degree programs with great success. Thank you for appreciating that science is fundamentally an evidence-based activity and for supporting the first significant re-acquisition of physics laboratory equipment for student explorations of physics concepts. Finally, Graham, thank you for promoting me as a candidate for employment — it worked!

Doctor Murray Black has gently administered the majority of my teaching efforts at AUT during this dissertation. I recognize Murray for his ability to gracefully balance bureaucratic demands with my passion for innovative teaching. Together, we have given students ownership in their learning, which has been

consistently reflected in their enthusiasm for my courses. As a leader, Murray has consistently made me feel part of something greater than myself. Finally, I thank Murray for selecting me, year after year, to deliver "inspirational astronomy" lectures to bright New Zealand high school students from across the country participating in Rotary's National Science & Technology Forum.

Danish computer "whiz" Boris Féron came into my life as a student in the first tutorial class I ever taught in New Zealand. He soon re-appeared as a postgraduate student in a shared office and then too soon departed with an impressive master's degree on the related topic of numerical computation of the distribution of excited electronic atomic states for arbitrarily high-order RRL transitions using arbitrary precision arithmetic. We became fast friends, collaborators and greatly aided and pushed one another through myriad challenges associated with translating complex ideas into logical statements consumable by computers.

I recognize all my students who have passed through courses I have facilitated during this dissertation. It is a privilege and distinct pleasure to propose my insights in physics/astronomy, mathematics, history and philosophy to you, our future. I particularly thank my astrophysics students for their enthusiastic response to my seminar series on the history & philosophy of science, modeled after the innovative Evergreen State College, Olympia, my alma mater.

Finally, I thank Beverly Barnett and John Barnett-Goodman, for renting their

amazing Valley View homestead to my family. The home is well-built, well-loved, and dry! This, with its peaceful and secluded woodland surrounds and impressive diversity of mature fruit trees, has greatly aided my final year of writing the dissertation. You are kind, totally down-to-earth, folks that give me hope.

Now I recognize my relations, gifted by fate...

I wish to thank Robert Alexander, my free-thinking father, for his life long nurturing of and engagement in my philosophical passions. As I child, he gave me books on space travel that totally captured my imagination. I wanted to be an astronaut, but not via the military. It was my father's passion for truth (ancient and modern), dialogue, writing/journalism and for civil rights & justice that helped guide me into academia. Throughout my studies, he was there exploring diverse and fundamental ideas, helping me translate complex ideas into written form. I recognize and greatly appreciate the significant financial contributions he made throughout my undergraduate and graduate studies. Into his eighties, he continues to request written forms of my research to read and correct my grammar — thank you, Babe, my greatest life-long advocate.

I recognize Linda Pickett Friedman, my mother, for raising my brothers and me on Lama mountain at the Magic Tortoise commune. This unusual, self-sufficient upbringing is a deep source of my curiosity, joy and persistence in this

life. Thank you, Linda, for patiently supporting my family and me from afar, both financially and spiritually, since we immigrated to New Zealand a decade ago. It brings me happiness in knowing that you experience joy in seeing me pursue my life's passion of exploring the unknown.

I thank Justin Eliot Friedman, my stepfather, for his substantial role in my formative years where I worked at his side from the late 1970s to the late 80s building our impressive adobe family home. As a self-taught craftsman and artist, you helped me appreciate that the hand is the cutting edge of the mind. I recognize your financial support of my family during the early years in New Zealand and consistently inquiring about my PhD progress. To both of you and Linda, thank you for advice on parenting Nina, Desmond & Lillian and having your grandchildren, for an extended visit, to experience the magic of Northern New Mexico in winter.

Kate, my partner, where would I be without you? It has been the greatest equatorial-crossing roller coaster ride of our adult lives and we did it together, with young and older children, dogs, generations of puppies, cats and chickens! Your tireless dedication to the cause has amazed and comforted me through the ups and downs. Joining and inspiring me along many lines of teaching has brought me endless joy. The many gourmet feasts, treats and snacks made for our family, colleagues and hundreds of students is nothing short of amazing, like those heady days at your San Juan island restaurant, Katrina's, where we

first met. Your perseverance in all aspects of our lives has given me the will to finally complete this, my greatest academic undertaking to date. Thank you, my beloved Kate, from the entirety of my being.

Well, Lillian, my daughter, here it is, Daddy's completed "scientific diary", as you once so aptly named it. You and your brother, Desmond, have brought me so much joy and laughter in this period of our lives — thank you. It is with fondness that I recollect all the times we "played hooky" and I brought you to my physics/astronomy lectures and we selected favorite musical tracks for the students to guess at during "music appreciation hour". And, Desmond, well, you asked me to share the following, politically incorrect, acknowledgement, so, here it is, in the original:

"But, most of all, I wish to thank Desmond Ganty Alexander and Lillian Pickett Alexander for their complete tormenting of my soul throughout this hellish quest :)"

I now thank Nina Stone, my step daughter, for teaching me about patience during the majority of this dissertation. You came to us in a time of need from the old country and challenged us in ways I never knew possible. We have all come a long way together; let's keep on trucking, baby!

Julian, my youngest brother, is hereby recognized for coming a long way throughout the period of this work; your success makes me very proud. Thank you for

teaching your nephew and niece to enjoy downhill skiing.

Ruchell, my younger and closest, brother, has helped keep my New Mexico spirit alive and well throughout this dissertation. His painting, my favorite "Dennis Brown: at the ganja gardens", has graced my work space for years. I have gazed upon it many times while contemplating the mysterious cosmos. It is reproduced in Figure 4.2.

Nicholas, my older brother, is recognized for many pep talks over the years that helped propel me over the finish line.

James Alexander, my eldest brother and first to complete a PhD in our family, is hereby recognized as a trail-blazer. His proof-reading of this dissertation and many suggestions for clarifying its exposition is greatly appreciated.

# Prologue[1]

There is little in our daily experience to condition ourselves to think in terms of the universality of space-time. Each year we become more dependent on clearly defined boundaries within which we may live comfortably. We want to know exactly what to expect and when. A life span of so many years, a speed limit of so many km/hr. A salary bracket of so much money.

Space and time does not fit this pattern. It breaks down all boundaries of thought. As a result, it is ignored by most and misunderstood by many, even those who take time to consider it. It is accepted and understood by a relative handful of pioneers willing to start from a mental jumping-off place beyond which most refuse to venture.

Consider, for a moment, some statistics of space and time:

We inhabit a tiny planet about an average star which is one in a galaxy of some

[1] Adapted from Bell (1960).

100 billion stars. If we had started counting at a rate of 100 stars a minute at the time Christ was born, we would just now be finishing the count.

Traveling at 10,000 km/hr, it would take us two days to reach the Moon, two years to reach the Sun and 80 years to arrive at Pluto. And it would take 470,000 years to reach Alpha Centauri, our next closest star system. This system is three gravitationally-bound stars — two similar to our sun, the third a red dwarf — with a growing number of detected planets, including an Earth-sized one in its habitable zone. There is now nearly 3000 confirmed planetary systems within 2000 light years of us. About one in five Sun-like stars have an Earth-sized planet in the habitable zone. Assuming there are 200 billion stars in the Milky Way, we can hypothesize that there are 11 billion potentially habitable Earth-sized planets in the Milky Way, rising to 40 billion if planets orbiting the numerous red dwarf stars are included. So, where is everybody?

These facts should not be considered prosaically, like this weeks grocery list or mortgage payment. These are incredible statistics requiring enhanced thinking, a mental gear-shifting necessary for the new age, the Space Age. And for a few, this thinking has preceded the space age. This is the stuff of pioneers.

Space alone is one of the great unknowns to be explored. A dictionary tells us that it is the interval between objects. What interval? What objects?

When scientists talk of space, they usually refer to a volume beyond 100 km al-

titude, below which lies the majority of Earth's atmosphere. Earth's gravitation is slight enough and its atmosphere thin enough that relatively low velocities will permit escape. And space is a vacuum far greater than any attainable on Earth.

It is from this last fact that the present dissertation begins an exploration of *giant cosmic atoms*...

# List of Figures

# List of Tables

# 1 Introduction

"No problem can be solved from the same level of consciousness that created it." *Albert Einstein (1879-1955)*

## 1.1 Goal

The goal of this dissertation is to deepen our understanding of matter at the highest electron excitations, known as Rydberg atoms.[1] This has been done by resolving a mystery about cosmic atoms detected from an enormous volume of ionized gas $\sim$1000 times that of our solar-system known as the Orion nebula, located, as we are, in the Orion arm, a minor spiral arm of our Milky Way galaxy (Brunthaler et al., 2011).[2] In resolving this mystery, I have *tested* the theory of spectral line broadening at the highest measurable changes in principal quantum

[1] Named after the Swedish physicist Johannes R. Rydberg (1854–1919) who predicted the frequencies of light emitted/absorbed by a change in the energy level of an electron in a hydrogen atom (Rydberg, 1890; Martinson and Curtis, 2005).

[2] $\sim$460 pc from Earth, this nebula is a stellar nursery containing stars $\sim$0.01% of the age of our Sun.

number, $\Delta n$, where atomic dimensions reach $\sim 10^5$ times that of hydrogen atoms in terrestrial laboratories and the spectral emission frequencies occur within the radio range of the electromagnetic spectrum.

## 1.2 A cosmic laboratory

Danish pioneer of quantum theory, Neils Bohr (1885-1962) anticipated that the most highly excited atoms will be cosmic in origin: "Only at very low pressures, large electronic orbits will not be disturbed by electrical forces of neighboring atoms... We can propose the existence of hydrogen in celestial bodies, and it could occupy huge areas" (Bohr, 1914). It was not until just after the end of his life that these most highly excited atoms were detected by radio astronomy techniques. Today, we know that such cosmic atoms have up to approximately 1000 distinctly observable electronic quantum levels (Gordon and Sorochenko, 2009).

The mean density between stars is $\sim 1$ atom per cubic centimeter (Kaplan and Pikel'ner, 1970). That is eight orders-of-magnitude lower than that attainable in the greatest vacuums created in terrestrial laboratories (van Atta et al., 1991). Thus, the ISM (interstellar medium) represents a unique "laboratory" to reveal phenomena of, and relationships between, atoms impossible to detect on Earth. The medium is subjected to radiation and energetic particles from astro-

physical objects and their associated processes, including stars, galactic corona, supernova explosions, cooling supernova remnants, shock-waves driven by supernova explosions, expanding H II (ionized hydrogen) regions, stellar winds, colliding interstellar-clouds and supersonic gas flows from forming stars. As a result, most of the matter in the ISM is a plasma characterized by populations of electrons, ions and neutral atoms in various states of excitation. In these voluminous and rarefied environments, atoms attain measurable dimensions approaching 0.1 mm, the width of a human-hair (Gordon and Sorochenko, 2009).

Such atoms, termed Rydberg atoms, are formed from radiative recombinations of electrons with ions into energy-levels $n \gg 1$, with subsequent de-excitations (cascades) producing photon emission. Such Rydberg states of atomic carbon have been observed in absorption against the supernova remnant Cassiopeia A from levels as large as $n = 1009$, $\Delta n = 4$, where the exciting-photon wavelength is $\lambda \sim 12\,\mathrm{m}$; a frequency of $\nu \sim 26\,\mathrm{MHz}$ (Stepkin et al., 2007). Here, $\Delta n$ is the transition order and represents the number of levels transited by electrons which absorb the photons, the lack of which is detectable in absorption spectra measured using radio telescopes.

Recombination lines are a powerful diagnostic of the environments they are excited by and in which they radiate from. Spanning eight-orders in wavelength, line-transition radiation from Rydberg atoms have been detected between $\lambda \sim 10^{-7}\,\mathrm{m}$ (ultraviolet) and 10 m (radio). Cosmic hydrogen, helium,

carbon and sulfur atoms have been detected by the observations of RRLs (radio recombination lines) (Gordon and Sorochenko, 2009). These are observed from galactic HII regions, planetary nebulae, diffuse interstellar gas, molecular clouds, and other galaxies, both in emission and absorption. RRLs address questions about the theory of star formation, structure & evolution of our galaxy, and primordial nucleosynthesis, as well as plasma physics & spectroscopy (Tsivilev et al., 2016).

In addition to identifying the chemistry of the ISM, recombination lines probe temperature and density of recombining plasmas. RRLs provide a relatively simple and precise method of determining the electron temperature $T_e$ in HII regions. Contrasted with optical emission lines, RRLs do not suffer from absorption by interstellar dust (Carroll and Ostlie, 1996). We can measure RRLs even in weak astronomical sources due to population-inversion of atomic states that produce spectral-line amplification, the basis of the "partial maser effect" (Goldberg, 1966; Strelnitski et al., 1996a,b). The population of atomic states and the degree of ionization, which determines the population ratio of bound to unbound quantum domains, are specified by a single parameter, $T_e$.[3] Because the temperature dependence of these two domains are different, the intensity ratio of spectral-line to continuum emission enables an accurate determination of $T_e$.

[3]This is valid for high-frequency RRLs, where radiative mechanisms dictate the distribution of bound states.

The electron density $N_e$ of an HII region may be found by measuring line-width broadening of RRL-profiles emanating from the same volume of gas. This broadening, known as impact Stark broadening, occurs when emitting atoms collide with other constituents, including electrons and ions. These impacts disrupt the electromagnetic wave of an emitting atom, causing effective reductions in atomic level lifetimes. The resulting spectral line profile is broadened as function of transition levels $(n, \Delta n)$ and $N_e$. Fitting this function to a series of observed Stark-broadened spectral lines and analyzing their relative line intensities enables the determination of $N_e$.

Finally, Rydberg atoms are currently attracting the attention of those working to realize quantum computing (Cooper, 2016). Atomic nuclei are roughly femtometres in size, while the excited valance electron can travel micrometers from the nucleus while still remaining bound. With such reach, Rydberg atoms interact with nearby atoms via an electric dipole moment millions of times larger than that of unexcited atoms. This interactive ability — controllable with a single carefully chosen photon — makes Rydberg atoms an attractive candidate for logic gates, the basis of modern computers (Goldschmidt et al., 2015).

## 1.3 Detection of cosmic radio recombination lines

In 1945, Dutch radio astronomer van de Hulst first considered the possibility of detecting RRLs from highly-excited states of atoms in the ISM, but concluded they will be too weak to observe due to significant weakening of emission-line intensity from Stark-broadening (van de Hulst, 1945). However, a mistake in these calculations showed Stark-broadening to be significantly larger than the correctly estimated thermal-broadening.

Soviet astronomer Kardashev reached the opposite conclusion for excited hydrogen RRLs in HII regions (Kardashev, 1959). He showed Stark-broadening will contribute insignificantly to line broadening for an electron temperature of $T_e = 10^4\,\mathrm{K}$ and density $N_e = 10^2\,\mathrm{cm}^{-3}$ at frequencies $\nu > 7\,\mathrm{GHz}$ ($\lambda < 4\,\mathrm{cm}$).

Soviet astronomers Sorochenko and Borodzich made the first definitive RRL detection in 1964. Using a 22 m telescope located near Moscow, they detected the transition between principal quantum numbers $n = 91$ and $n = 90$ (spectral line H90$\alpha$ according to RRL notation) at 8.9 GHz from M17 (Omega nebula) (Sorochenko and Borodzich, 1965). At about the same time, working independently, another Soviet astronomy group marginally detected the H104$\alpha$ transition at 5.8 GHz from M17 and M42 (Dravskikh and Dravskikh, 1964).

This and other detected RRL emissions gave surprising results regarding their line intensities (Höglund and Mezger, 1965; Lilley et al., 1966). The derived electron temperatures averaged $\sim 5000\,\mathrm{K}$, while the accepted temperature of HII regions in our galaxy based on forbidden optical lines was twice this (O'Dell, 1966).

The resolution of this discrepancy came from physics developed in the 1930s to explain anomalous optical line intensities from nebulae and stellar atmospheres by accounting for departures of a plasma from thermodynamic equilibrium, $b_n = N_n/N_n^{\mathrm{LTE}}$, where $N_n$ is the population of level $n$ and $N_n^{\mathrm{LTE}}$ is the population of this level predicted from thermodynamic equilibrium (Baker and Menzel, 1938). Leo Goldberg showed the observed RRL intensities are explained by accounting for these departures (Goldberg, 1966). In particular, he showed that RRL intensities are sensitive to the logarithmic derivative $\frac{\mathrm{d}\ln b_n}{\mathrm{d}n}$; see Chapter 2.

Another surprising result that emerged from the early observation of RRLs was the absence of Stark broadening in detected line profiles (Sorochenko and Borodzich, 1965; Höglund and Mezger, 1965; Lilley et al., 1966), which contradicted the theory of spectral line broadening (Griem, 1960). Specifically, all RRLs observed in M17 with principal quantum numbers up to $n = 166$, had constant ratios of line-width to frequency, indicating pure Doppler broadening (Sorochenko and Borodzich, 1965; McGee and Gardner, 1967).

The explanation of this discrepancy was found through revision of the impact broadening theory (Griem, 1967; Minaeva et al., 1967) and by accounting for the non-homogeneous density structure in the observed ISM (Hoang-Binh, 1972; Brocklehurst and Seaton, 1972; Simpson, 1973a,b; Gulyaev and Sorochenko, 1974; Lockman and Brown, 1975). The latter effect was overlooked when applying the theory of spectral line broadening based on the laboratory condition of homogeneous densities. The absence of Stark broadening for a non-homogeneous density distribution results from the fact that optical depth in a plasma increases with decreasing frequency, gradually leading to complete opaqueness of high-density areas. This increase in gas opacity means that observed lines at lower frequencies increasingly manifest themselves in the more transparent, lower density outer areas of an HII region, where they are minimally Stark broadened. For high $n$ RRLs, which occur at lower frequencies, the core of an HII region becomes opaque, and therefore, contribution of these highly Stark broadened lines becomes negligible and Stark broadening can be observationally undetectable (Gulyaev and Sorochenko, 1974).

The changing opacity as a function of frequency & location in HII regions and the variations in beam-width of radio-telescopes as a function of frequency prevented the detection of the predicted increase in Stark broadening as a function of $n$. In order to verify the Stark broadening theory, it was suggested to observe RRLs of increasing transition order $\Delta n$, while maintaining a constant observing

frequency, and thus a constant beam-width (Minaeva et al., 1967). In this case, as $\Delta n$ increases, $n$ also increases and lines exhibit increasing amounts of Stark broadening compared with the contribution of pure Doppler broadening in these line profiles.

Suitable choices of $n$ are obtained from the Rydberg formula (Rydberg, 1890), where emission frequency $\nu$ is related to $n$ and $\Delta n$ as

$$\nu = cR\left(\frac{1}{n^2} - \frac{1}{(n+\Delta n)^2}\right) \approx \frac{2cR\Delta n}{n^3},\ \Delta n \ll n, \tag{1.1}$$

where $c$ is the speed of light and $R$ is the Rydberg constant.

For example, when $\nu = 6\,\mathrm{GHz}$ and $\Delta n = \{1,2,3\}$, Equation 1.1 predicts the series: H103$\alpha$, H129$\beta$, H147$\gamma$.

The observational challenge with this suggestion is that RRL intensities rapidly weaken with increasing $\Delta n$ as $I \propto \Delta n^{-k}$. From the intensity data presented in Section 3.5 on the Orion nebula at 6 GHz, I find $2 < k < 3$ and it grows with increasing $\Delta n$ at fixed frequency. For example, at 6 GHz, the peak intensity of the H$n\delta$ line is about ten-times less than the intensity of the H$n\alpha$ line. This situation made it impossible, until the early 1970s, to detect a sufficiently-long series of higher-order lines, with adequate sensitivity, using a single telescope to test line broadening theory.

Leveraging these theoretical and observational RRL insights, R. Davies pub-

lished remarkable high-order RRL observations at 5 GHz, that included detections of H RRLs from M42 for $\Delta n = 1...3$ and for $\Delta n = 1...5$ from M17 using the 140ft Greenbank telescope in West Virginia (Davies, 1971). Figure 1.1 (green triangles) shows the variation in the observed line-widths as a function of $n$ for M42.[4]

A novel observing technique using two radio telescopes of differing diameters enabled detections of H RRLs from M42 for $\Delta n \leq 6$ (Smirnov et al., 1984). The two telescopes observed at differing frequencies such that a series of higher-order lines were observed with the same beam-width and hence from the same volume of plasma. Figure 1.1 (red circles) shows the variation in the observed RRL widths as a function of $n$ at 5 GHz. Taken together, Davies' and Smirnov et al.'s data clearly indicate broadening of RRLs with increasing $n$.

[4]These data are extracted from Davies' published spectral line profiles using Dexter (a software tool for extracting data from scanned figures, (GAVO Data Center, 2008) and Gaussian profile fitting.

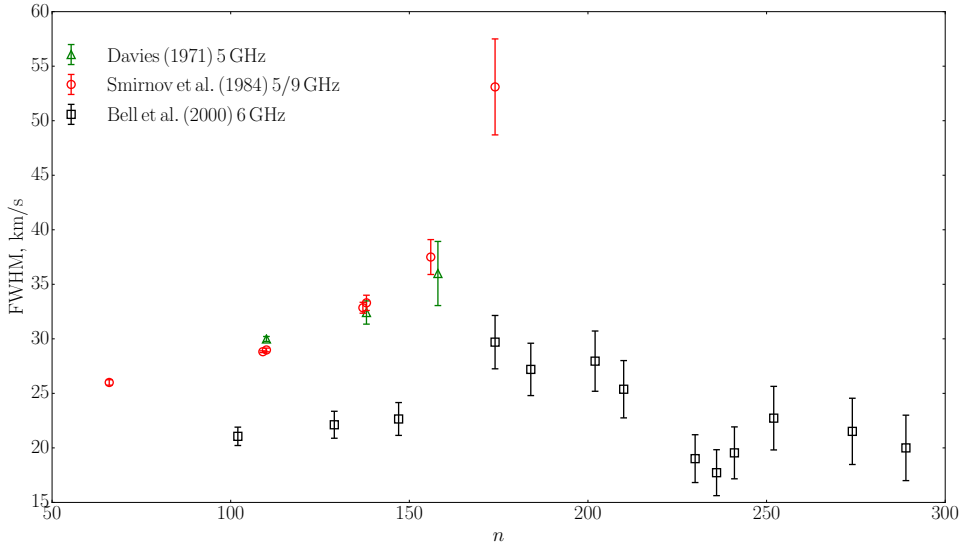


**Figure 1.1:** RRL widths versus principal quantum number for M42 reported by Davies (1971) (green triangles), Smirnov et al. (1984) (red circles) and Bell et al. (2000) (black squares).

## 1.4 Solving a radio recombination line mystery

Figure 1.1 (black squares) also shows published RRL widths from an even greater- and higher-range of H$n\Delta n$ transitions at 6 GHz, using the same 140 ft Greenbank used by Davies (Bell et al., 2000, 2011). It suggests that, not only is there a limit to Stark broadening, which is not predicted by the theory, but that the established theory of Doppler broadening is in doubt. These results, referred to as "processed" widths by the authors, were obtained from a single telescope using a novel technique based on *multiple* frequency-switching with small frequency offsets which gives flat spectral baselines without having to fit and remove polynomials or sinusoids (Bell, 1997).

The first published response to these unexpected results appeared in 2002 as a footnote in the first edition of the "bible", *Radio Recombination Lines* (Gordon and Sorochenko, 2002). There, it is stated, "These results are so different from what had been expected, and the observing technique is so new, that prudence requires independent confirmation before accepting a fault in the present theory of RRL Stark broadening."

In response to Bell et al.'s claims, Oks (2004) suggested that the model of Stark broadening may need to change from an impact regime to a quasi-static one, where Bell et al.'s results indicate the onset of decreasing RRL widths with increasing $n$ — see Figure 1.1. Although this is consistent with the quasi-static model, it has been argued by Griem (2005) that Oks' suggestion is based on an inappropriate choice of the Weisskopf radius, which quantifies the strength of interactions between perturbers and the emitting atom's electromagnetic wave-train (Gordon and Sorochenko, 2009). As a result, this choice falsely indicates a breakdown of the impact model. Also in response to Bell et al.'s claims, numerical calculations of electron-impact broadening of RRL of hydrogen for different $\Delta n$ has been done by Watson (2006). Results indicate that widths increase monotonically up to $n > 300$, as expected from electron-impact broadening theory. The puzzle regarding the observed narrowing of the lines therefore remained unsolved in the literature.

Bell (1997)'s data reduction technique is an extension of the frequency-switching

technique developed by Dicke (1946) to reduce inherent receiver gain fluctuations. It is used to detect weak spectral lines in the presence of baseline variations by switching the local oscillator in the receiver hardware to produce two passbands, one slightly shifted in frequency from the other. Assuming the presence of a single spectral line feature, subtracting one passband from the other produces an *overlapped* spectrum containing two lines — of equal and opposite strength — separated by a small *frequency-offset*. Baseline variations with "periods" greater than the frequency-offset are significantly minimized in the subtraction, thereby flattening the baseline. In conventional frequency-switching, the two lines are then co-aligned and subtracted to obtain a $\sqrt{2}$ improvement in S/N (signal-to-noise ratio).

Bell's novelty is recognizing that additional overlaps of the original overlapped spectrum further flattens the base-line. Though more line pairs are created by these iterative overlaps, they are systematically removed based on the number of overlaps applied. My investigations (in Section 4.1) find that, in the presence of baseline variations, Bell's technique is able to accurately recover spectral lines with residuals approaching that of the original thermal noise limit. However, my investigations also show that application of their technique fails to accurately recover spectral line parameters when the frequency-offset becomes less than the width of the spectral line itself (Alexander and Gulyaev, 2012); see also Liszt (1997). In this case, recovered line-widths depend on the frequency-offset

only, i.e., a constant, instead of actual line-widths. I argue in Section 4.1 that this finding explains Bell et al.'s published line-narrowing as an artifact of their processing technique and indicates that electron-impact Stark broadening theory remains valid.

In Section 4.2 I summarize five series of RRL observations, including my original observations conducted with the highest (at this time) precision (Alexander and Gulyaev, 2016). I demonstrate that Stark broadening theory is consistent with all of these statistically significant results. I also show that (at this time) it is not possible to distinguish between the theoretical results of Griem (1967) & Gee et al. (1976) and Watson (2006) & Peach (2015).

## 1.5 Dissertation roadmap

Chapter 2 reviews the physics of plasmas and RRLs. This sets the stage for exploring an apparent RRL mystery published by Bell et al. (2000) that is thoroughly explored in my first publication, reproduced in Section 4.1. Chapter 3 details the processing and analysis of my ATCA (Australia Telescope Compact Array) radio frequency interferometry observations, which forms the basis of all original results presented in this dissertation and which are not presented in my second publication reproduced in Section 4.2. Chapter 4 begins with a summary of the findings of my publications and ends with the publications

themselves. Section 4.1 is the 2012 publication on the "reverse-engineering" of Bell (1997)'s data processing technique and the associated findings (Bell et al., 2000, 2011) that initiated testing models of RRL intensities and widths at the highest detectable principal quantum number changes using observations of cosmic plasmas. Section 4.2 is the 2016 publication which focuses on the widths of high-order RRL detections from my 2013 Orion nebula observations. Chapter 5 summarizes the findings of this dissertation and suggests future work in the detection and analysis of high-order RRLs.

## 1.6 Approbation

The findings of this dissertation are published as two papers in the Astrophysical Journal (Alexander and Gulyaev, 2012; Alexander and Gulyaev, 2016). These findings were presented in seminars at AUT's Institute for Radio Astronomy and Space Research and at international conferences: Astronomical Society of Australia's annual scientific meeting (with a poster reproduced in Figure 4.1), Sydney 2012; International Conference on Spectral Line Shapes, St. Petersburg 2012; Serbian Conference on Spectral Line Shapes in Astrophysics, Srebrno jezero 2015. These findings are generally accepted by international experts in Stark broadening and RRLs, including Goss, Griem, Peach, Smirnov, Sorochenko and Watson.

# 2 Radio recombination lines in cosmic plasmas

"If you want to find the secrets of the universe, think in terms of energy, frequency and vibration." *Nicola Tesla (1856-1943)*

## 2.1 Intensity of radio recombination lines

The intensities, i.e., line-strengths, of RRLs emanating from a plasma at frequencies predicted by Rydberg's formula (Equation 1.1) depend essentially on the relative populations of the atomic energy levels and probability of transition between these levels. First, we need to determine the distribution of electrons as a function of energy, both for free electrons (positive energy states) and electrons bound in atoms (negative discrete energy states).

### 2.1.1 Population of highly-excited atomic levels

The observed velocity distribution of electrons in plasma is accurately modeled by a Maxwell-Boltzmann velocity distribution when electron-electron collisions dominate (Maxwell, 1860; Boltzmann, 1868; Chapman and Cowling, 1970). Such collisions are much more efficient at energy-redistribution than radiative processes and inelastic collisions. Therefore, the distribution function for free electrons is assumed to be a Maxwell-Boltzmann distribution. For bound states, it is assumed that the level populations are determined by radiative and collisional processes. At low-$n$ levels, the probabilities of radiative processes are much greater than the probabilities of collisional processes. However, this assumption is not correct in the limit of highly excited states ($n \gg 1$), where the populations are determined by collisional processes, resulting in a distribution similar to that of the distribution for free electrons (Seaton, 1964).

For a plasma at a given temperature and pressure, the number of atoms in a given principal quantum level $n$ is given by

$$N_n = b_n N_n^{\mathrm{LTE}}, \tag{2.1}$$

where $b_n$ accounts for the plasma's departure from LTE (local thermodynamic

equilibrium). $N_n^{\mathrm{LTE}}$ is given by the Saha-Boltzmann equation,

$$N_n^{\mathrm{LTE}} = \frac{N_e N_i}{T^{3/2}} \frac{n^2 h^3}{(2\pi mk)^{3/2}} \exp\left(\frac{Z^2 E_n}{kT}\right), \tag{2.2}$$

which relates the equilibrium number density of atoms $N_n^{\mathrm{LTE}}$ in bound-level $n$ to the population density of electrons and ions of the unbound states of hydrogenic atoms, $N_e$ and $N_i$; $h$ is Plank's constant, $m$ is the mass of the electron, $k$ is Boltzmann's constant, $Z$ is the number of protons in the atom's nucleus ($Z = 1$ for hydrogen) and $E_n$ is the energy difference between level $n$ and the continuum.

Departure coefficients $b_n$ are found by solving the system of equations (for all $n$ levels) describing the statistical equilibrium of a plasma, known as the equation for statistical equilibrium (Aller, 1963). All the ways out of a quantum level $n$ are equated to all ways into that level,

$$N_n \sum_{n \neq n'} P_{n,n'} = \sum_{n \neq n'} N_{n'} P_{n',n} \,, \tag{2.3}$$

where $P$ represent the rates of physical processes in the directions indicated by the subscripts. The left-hand-side of Equation 2.3 includes all processes that depopulate level $n$, while the right-hand-side includes all processes that populate it. In LTE, each rate into a level must balance exactly with the same kind of rate out of that level. This is known as the principle of "detailed balance" (Landau

and Lifshitz, 1980).

The physical processes of importance in a thermal plasma are radiative and collisional. An excited level $n$ is populated by,

1. collisional transitions from other bound levels,
2. spontaneous radiative cascade transitions from higher levels,
3. recombination from the continuum through radiative and three-body recombination processes,

and depopulated by,

1. spontaneous radiative transitions to lower levels,
2. electron collisions that cause transitions to other atomic levels,
3. collisional ionization.

Accounting for these processes leads to the following equation of statistical equilibrium for level $n$,

$$N_n \left(A_n + C_{n,n\pm1} + C_{n,i}\right) = N_{n+1} C_{n+1,n} + N_{n-1} C_{n-1,n} + \sum_{n'>n} N_n A_{n',n} + N_i N_e \left(a^r_{i,n} + C_{i,n}\right) \tag{2.4}$$

where collisional transitions only to adjacent levels are accounted for (Dupree, 1969).

Using words, Equation 2.4 states: in statistical equilibrium, the number of transitions per unit volume per unit time out of level $n$ from radiative, collisional, and ionization processes equals the number of transitions into level $n$ per unit volume per unit time from recombination and from radiative & collisional processes from other levels.

$A_n(\mathrm{s}^{-1})$ is the rate of spontaneous emission to lower levels $< n$, and $C_{n,n'}(\mathrm{s}^{-1})$ is the rate of inelastic collisions between levels $n$ and $n'$ or the ionization rate when $n' = i$. The rate coefficient for radiative recombination is $a^r_{i,n}(\mathrm{cm}^3\,\mathrm{s}^{-1})$.

Following Dupree (1969), Equation 2.4 is written as

$$\sum_{n'=n-1}^{n+1} R_{n,n'}\, b_{n'} = S_n \tag{2.5}$$

for each level $n$, where

$$R_{n,n-1} = \frac{\omega_{n-1}}{\omega_n} C_{n-1,n} \exp\left(X_{n-1} - X_n\right) \,, \tag{2.6}$$

$$R_{n,n} = A_n + C_{n,n\pm1} + C_{n,i} \,, \tag{2.7}$$

$$R_{n,n+1} = \frac{\omega_{n+1}}{\omega_n} \left(C_{n+1,n} + A_{n+1,n}\right) \exp\left(X_{n+1} - X_n\right) \,, \tag{2.8}$$

$$S_n = 2\left(2\pi mkT_e\right)^{3/2} h^{-3} \frac{1}{\omega_n} a^r_{i,n} \exp\left(-X_n\right) + C_{n,i} + \sum_{n'>n+1} b_{n'} A_{n',n} \frac{\omega_{n'}}{\omega_n} \exp\left(X_{n'} - X_n\right) \,, \tag{2.9}$$

and

$$X_n = \frac{hcRZ^2}{n^2 kT_e} \,, \tag{2.10}$$

where $\omega_n = 2n^2$ is the statistical weight of level $n$.

The cascades from levels $n' > n+1$ are contained in the $S_n$ term, while interactions with adjacent levels $n' = n \pm 1$ are contained in the $R_{n,n\pm1}$ terms.

Expanding Equation 2.4 for an atom with $n_{\max}$ levels results in a system of $\Delta = (n_{\max} - n_{\min}) + 1$ equations that form a tri-diagonal square matrix in $R$,

$$\begin{pmatrix}
R_{n_{\min},n_{\min}} & R_{n_{\min},n_{\min}+1} & & & & & 0 \\
R_{n_{\min}+1,n_{\min}} & R_{n_{\min}+1,n_{\min}+1} & R_{n_{\min}+1,n_{\min}+2} & & & & \\
 & R_{n_{\min}+2,n_{\min}+1} & R_{n_{\min}+2,n_{\min}+2} & R_{n_{\min}+2,n_{\min}+3} & & & \\
 & & \ddots & \ddots & \ddots & & \\
 & & & R_{n_{\max}-1,n_{\max}-2} & R_{n_{\max}-1,n_{\max}-1} & R_{n_{\max}-1,n_{\max}} & \\
0 & & & & R_{n_{\max},n_{\max}-1} & R_{n_{\max},n_{\max}} &
\end{pmatrix}$$

$$= \begin{pmatrix} b_{n_{\min}} \\ b_{n_{\min}+1} \\ b_{n_{\min}+2} \\ \vdots \\ b_{n_{\max}-1} \\ b_{n_{\max}} \end{pmatrix} \begin{pmatrix} S'_{n_{\min}} \\ S_{n_{\min}+1} \\ S_{n_{\min}+2} \\ \vdots \\ S_{n_{\max}-1} \\ S'_{n_{\max}} \end{pmatrix} , \tag{2.11}$$

where

$$S'_{n_{\min}} = S_{n_{\min}} - R_{n_{\min},\, n_{\min}-1}\, b_{n_{\min}-1}, \tag{2.12}$$

$$S'_{n_{\max}} = S_{n_{\max}} - R_{n_{\max},\, n_{\max}+1}\, b_{n_{\max}+1}, \tag{2.13}$$

and $b_{n_{\min}-1}$, $b_{n_{\max}+1}$ are the lower and upper boundary-values of the departure coefficient spectrum $b_n$.

Equation 2.11 is solved using a simplified form of Gaussian elimination that reduces the number of required operations from $\Delta^3$ to $\Delta$ (Riley et al., 2006). A complication in the solution arises from the presence of $b_n$ in the cascade term, $S_n$. This is addressed by an iterative procedure in which all $b_n$ are initially set to unity and after each iteration the new $b_n$ are used to re-compute $S_n$. This is repeated until successive sets of $b_n$ agree to within a percent.

The resulting $b_n$ spectrum is insensitive to the choice of the lower boundary-condition $b_{n_{\min}-1}$ and $n_{\min}$, given $n_{\min}$ is chosen where radiative rates dominate and collisions with degenerate angular momentum states $l$ are insignificant (Gordon and Sorochenko, 2009). For the plasma conditions typical of HII regions $\left(N_e \sim 10^4\,\mathrm{cm}^{-3},\ T_e \sim 10^4\,\mathrm{K}\right)$, this is the case for $n_{\min} \sim 40$. In this case, an asymptotic form of $b_n$ is used (Seaton, 1959):

$$b_n\,(\text{radiative}) = \frac{3\ln n - 4.84}{3\ln n - 1.84}. \tag{2.14}$$

However, the choice of the upper boundary-condition $b_{n_{\max}+1}$ and the value of $n_{\max}$ strongly effects the shape of the calculated $b_n$ spectrum. This fundamentally affects the behavior of our plasma model, i.e., RRL intensities and widths.

Above $n_{\max}$, it is assumed the levels will be in equilibrium due to collisional coupling with the continuum. From Dupree (1969), $n_{\max}$ is estimated from when the collisional ionization rate is much greater than the rate of spontaneous emission, i.e., when $C_{n,i} \gg A_n$. Using Shaver (1975), $C_{n,i} \approx 10^{-5} n^2 N_e$ and $A_n \approx 10^{10} n^{-5}$, leading to the condition $n_{\max} \gg 10^2 N_e^{-1/7}$. For $N_e = 10^4\,\mathrm{cm}^{-3}$, this gives $n_{\max} \gg 10$. Another approach to estimating $n_{\max}$, which assumes atomic dimensions are no greater than the mean distance between particles, is to calculate the mean distance between electrons from $N_e$ and equate this to the atomic radius at level $n$. Thus, $\bar{r} \approx N_e^{-1/3}$ and $r_n \approx a_0 n^2$ gives $n_{\max} \approx 10^4 N_e^{-1/6}$, which predicts $n_{\max} \approx 10^4$ when $N_e = 10^4\,\mathrm{cm}^{-3}$.

Together, these two approaches imply that the size of atoms and their corresponding number of available/observable energy levels are huge in the ISM relative to laboratory plasmas, such as those produced in a fusion reactor where $N_e \geq 10^{13}\,\mathrm{cm}^{-3}$ (Garabedian, 2003).

However, there is a significant problem that arises as $n$ grows large, namely that

the partition function for hydrogenic atoms

$$Z = \sum_{n=1}^{n_{\max}} 2n^2 \exp\left[\frac{-(E_1 - E_n)}{kT}\right] \tag{2.15}$$

diverges because the Boltzmann factor approaches the constant value $\exp\left(\frac{-E_1}{kT}\right)$, while $n^2$ grows.

This physically implies that the number of atoms $N_n$ having an electron in a given level $n$, as $n$ tends to infinity, also tends to infinity. This appears to be unphysical. Instead, it should tend to zero. That is, the probability of finding atoms with electrons in such an excited state should decrease the farther it is from its nucleus.

The second approach to estimating $n_{\max}$ assumes that beyond $n_{\max}$, atoms cease to have more energy-levels available to populate, meaning that the probability of bound-electrons existing beyond $n_{\max}$ is zero. This suggests that $b_{n_{\max}+1} = 0$ is more physically plausible than $b_{n_{\max}+1} = 1$ in describing the relative populations of atomic energy levels at large $n$, because now the transition from bound states to the continuum is "lowered" from infinity to $n_{\max}$.

The convergence problem of atomic partition functions and its termination is connected with the phenomena of "lowering of the ionization potential", which accounts for non-ideal, collective effects in a plasma due to perturbations from nearby charges, neutral atoms, and plasma Debye interactions (Cowley, 1970;

Gündel, 1970, 1971). These non-ideal effects were explored in Gulyaev (1990) to extend the theory of Stark broadening to observations of cosmic plasmas at large principal quantum numbers.

### 2.1.2 Radiative transfer

A radiative transfer model is used to predict the continuum and spectral line emission from a plasma, given its geometry, density and temperature structures. The radiative transfer equation

$$\mathrm{d}I_\nu = -I_\nu \, \kappa(\nu) \, \mathrm{d}x + j(\nu) \, \mathrm{d}x \tag{2.16}$$

describes the change in intensity of radiation $\mathrm{d}I_\nu$ as it traverses a distance $\mathrm{d}x$ through the plasma. The first term on the right-hand-side accounts for absorption of radiation by the plasma. The second term accounts for its emission. Integrating/Iterating Equation 2.16 from the "back" to the "front" of the plasma calculates the emerging radiation (Chandrasekhar, 1960). Figure 2.1 illustrates the transfer equation.

$\kappa(\nu)$ is the linear absorption coefficient in units of inverse-length. It accounts for *reductions* of intensity along the line of sight of a detector. $j(\nu)$ is the linear emission coefficient. It accounts for all the *gains* in intensity along the line of sight of a detector. $\kappa(\nu)^{-1}$ is the mean free-path of a photon before

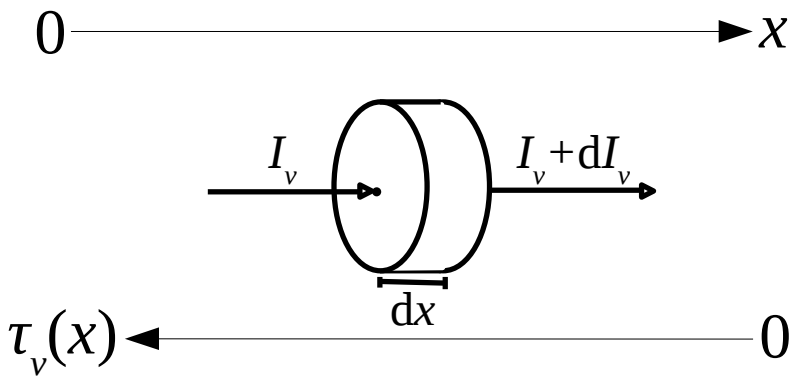


**Figure 2.1:** Radiation transfer

it is absorbed in the plasma. The product of $\kappa(\nu)$ and distance is defined as "optical depth" or $\tau_\nu$, such that $\tau_\nu \equiv \int_{x_1}^{x_2} \kappa(\nu)\, dx = 1$ for a traversed-distance of one mean free path. If $\tau_\nu \gg 1$ when integrated from back-to-front through the plasma at given frequency $\nu$, it is known as "optically-thick". If $\tau_\nu \ll 1$ when integrated in the same way, it is known as "optically-thin".

$\kappa(\nu)$ and $j(\nu)$ are physically related. Their ratio, $j(\nu)/\kappa(\nu)$, is an intrinsic property of an emitting plasma. A solution of the radiative transfer Equation 2.16 requires specifying this ratio as a function of location and frequency. In thermodynamic equilibrium, where the radiation field is specified by a single parameter $T$ (defined as *temperature*), this ratio is related through the Planck function $B_\nu(T)$ as

$$j(\nu)/\kappa(\nu) = B_\nu(T) \tag{2.17}$$

from Kirchhoff's law of thermal radiation (Kirchhoff, 1860), where $B_\nu(T)$ is a function only of frequency and temperature.

The Planck function (Planck, 1901) is

$$B_\nu(T) = \frac{2h\nu^3}{c^2}\frac{1}{e^{h\nu/kT}-1}. \tag{2.18}$$

When $h\nu/kT \ll 1$, which often occurs at radio frequencies in astronomy, the Rayleigh-Jeans approximation (Rayleigh, 1900; Jeans, 1905) of $B_\nu(T)$ is

$$B_\nu(T) \approx \frac{2\nu^2 kT}{c^2}, \tag{2.19}$$

given $e^{h\nu/kT} \approx 1 + h\nu/kT$ in Equation 2.18.

A plasma is populated by ions, free electrons, and neutral atoms in various states of excitation. These components interact through collisional and radiative excitation and de-excitation processes. Radiation absorbed and emitted from these processes is usefully divided into continuous (classical) and quantum domains. $\kappa(\nu)$ and $j(\nu)$ are then written as

$$\kappa(\nu) = \kappa_{\rm C}(\nu) + \kappa_{\rm L}(\nu) \;\text{ and }\; j(\nu) = j_{\rm C}(\nu) + j_{\rm L}(\nu), \tag{2.20}$$

where $\kappa_{\rm C}(\nu)$ is the continuum absorption coefficient, $\kappa_{\rm L}(\nu)$ is the line absorption coefficient, $j_{\rm C}(\nu)$ is the continuum emission coefficient, and $j_{\rm L}(\nu)$ is the

line emission coefficient.

### 2.1.3 Continuum emission

At radio frequencies, Bremsstrahlung or "free-free" radiation between electrons and ions is the dominate mechanism producing and absorbing continuum radiation in HII (ionized hydrogen) plasmas typical of nebulae (Gordon, 1988; Condon and Ransom, 2016). Calculating $\kappa_{\mathrm{C}}(\nu)$ requires accounting for the electrical interactions between two charged particles and their velocity distributions. $\kappa_{\mathrm{C}}(\nu)$ is determined by integrating the emission produced during each encounter over the velocity distribution of the particles, which is assumed to be Maxwell-Boltzmann distribution. Equation 2.94 of Gordon and Sorochenko (2009), gives an expression for $\kappa_{\mathrm{C}}(\nu)$ that is used in the plasma model of the Orion nebula used in this dissertation,

$$\kappa_{\mathrm{C}}(\nu) = 9.770 \times 10^{-3} \frac{N_e^2}{\nu^2 T_e^{3/2}} \left[ 17.72 + \ln\left( \frac{T_e^{3/2}}{\nu} \right) \right], \tag{2.21}$$

giving $\kappa_{\mathrm{C}}(\nu)$ in units of $\mathrm{cm}^{-1}$ when the electron density $N_e$ is in units of $\mathrm{cm}^{-3}$, electron temperature $T_e$ is in Kelvins and $\nu$ in Hz.

An approximation to Equation 2.21 given by Altenhoff et al. (1960) is

$$\kappa_{\mathrm{C}}(\nu) \approx \frac{0.2120 N_e^2}{\nu^{2.1} T_e^{1.35}}. \tag{2.22}$$

and $j_C(\nu)$ is obtained using Kirchhoff's law, Equation 2.17.

The continuum radiation as a function of frequency from an HII region is predicted by the radiative transfer equation. Assuming a homogeneous ($N_e =$ constant) and isothermal ($T_e =$ constant) slab of H plasma of thickness $L$, the resulting radiation intensity $I_\nu$ is found by numerically iterating Equation 2.16. Assuming the initial intensity on the far-side of the region is zero $I_\nu^{(0)} = 0$, then after a small distance d$x$ into the region along the line of sight toward the observer, the intensity is

$$I_\nu^{(1)} = I_\nu^{(0)} + \mathrm{d}I_\nu^{(0)} = \mathrm{d}I_\nu^{(0)} \tag{2.23}$$

$$\mathrm{d}I_\nu^{(0)} = -I_\nu^{(0)}\kappa(\nu)\,\mathrm{d}x + j(\nu)\,\mathrm{d}x = j(\nu)\,\mathrm{d}x \tag{2.24}$$

$$I_\nu^{(1)} = j(\nu)\,\mathrm{d}x \tag{2.25}$$

which means the intensity at this point has increased due to emission, $j(\nu)\,\mathrm{d}x$.

After the next differential step toward the observer, the intensity becomes

$$\begin{aligned} I_\nu^{(2)} &= I_\nu^{(1)} + \mathrm{d}I_\nu^{(1)} = j(\nu)\,\mathrm{d}x - I_\nu^{(1)}\kappa(\nu)\,\mathrm{d}x + j(\nu)\,\mathrm{d}x \\ &= 2j(\nu)\,\mathrm{d}x - j(\nu)\,\kappa(\nu)\,(\mathrm{d}x)^2, \end{aligned} \tag{2.26}$$

whereby it *increases* by another unit of emission $j(\nu)\,\mathrm{d}x$, while *decreasing* by $I_\nu^{(1)}\kappa(\nu)\,\mathrm{d}x = j(\nu)\,\kappa(\nu)\,(\mathrm{d}x)^2$.

Continuing in this way for $L/\mathrm{d}x$ steps, the intensity emerging from the near-side of the HII region is what is seen by the observer, assuming no other intervening sources of significant emission and absorption.

Figure 2.2 shows a plot of intensity versus frequency numerically predicted by the radiative transfer Equation 2.16 using parameters typical for HII regions at radio frequencies: $N_e = 10^4\,\mathrm{cm}^{-3}$, $T_e = 10^4\,\mathrm{K}$, $L = 10^{18}\,\mathrm{cm}$. It can be seen that the continuum intensity rises rapidly at low frequencies as $I_\nu \propto \nu^2$ and falls slowly at high frequencies as $I_\nu \propto \nu^{-0.1}$. This behavior emerges, as follows, when solving the radiative transfer equation for an isolated slab of homogeneous plasma at a single temperature.

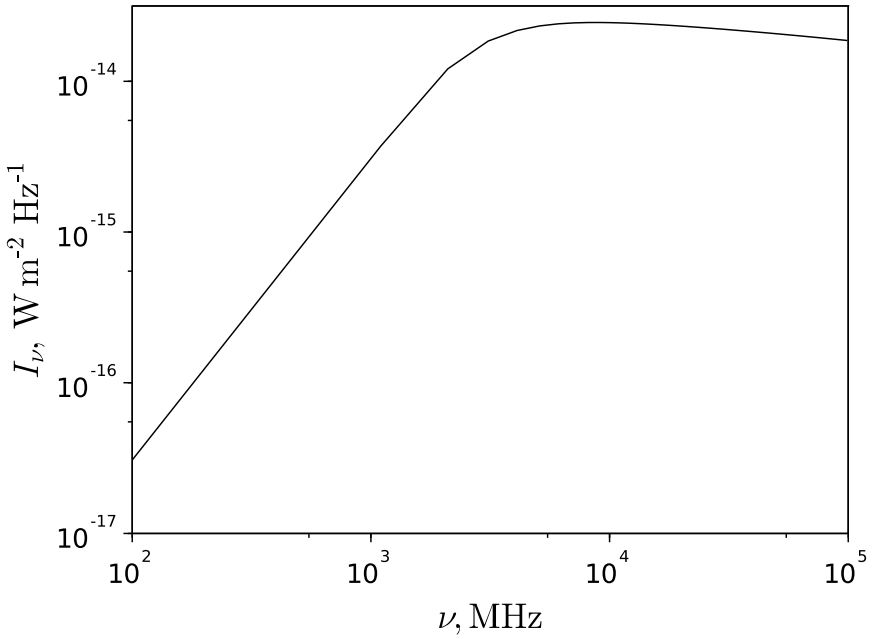


**Figure 2.2:** Continuum emission model. Numerical simulation result of the radiative transfer equation predicting brightness $I_\nu$ versus frequency $\nu$ for a typical HII region. Model parameters are $N_e = 10^4\,\mathrm{cm}^{-3}$, $T_e = 10^4\,\mathrm{K}$ and $L = 10^{18}\,\mathrm{cm}$.

Begin by re-arranging Equation 2.16 as

$$\frac{\mathrm{d}I_\nu}{\kappa(\nu)\,\mathrm{d}x} = -I_\nu + \frac{j(\nu)}{\kappa(\nu)}. \tag{2.27}$$

Given optical depth[1] is $\mathrm{d}\tau_\nu = -\kappa(\nu)\,\mathrm{d}x$ and $\dfrac{j(\nu)}{\kappa(\nu)} = B_\nu(T)$ is the a source function which assumes a radiation field in local thermodynamic equilibrium, then

$$\frac{\mathrm{d}I_\nu}{\mathrm{d}\tau_\nu} = I_\nu - B_\nu(T). \tag{2.28}$$

This equation is solved by integrating *from* the far-side *to* the near-side of the plasma using integration-by-parts $\int_a^b p\frac{\mathrm{d}q}{\mathrm{d}r}\mathrm{d}r = pq|_a^b - \int_a^b q\frac{\mathrm{d}p}{\mathrm{d}r}\mathrm{d}r$, where $p = e^{-\tau_\nu}$ and $\frac{\mathrm{d}q}{\mathrm{d}r} = \frac{\mathrm{d}I_\nu}{\mathrm{d}\tau_\nu}$. This leads to

$$\int_{\tau_\nu}^{0} e^{-\tau_\nu}\frac{\mathrm{d}I_\nu}{\mathrm{d}\tau_\nu}\mathrm{d}\tau = e^{-\tau_\nu}I_\nu|_{\tau_\nu}^{0} - \int_{\tau_\nu}^{0} I\,\frac{\mathrm{d}(e^{-\tau_\nu})}{\mathrm{d}\tau_\nu}\mathrm{d}\tau_\nu = \int_{\tau_\nu}^{0} e^{-\tau_\nu}\left(I_\nu - B_\nu(T)\right)\mathrm{d}\tau_\nu. \tag{2.29}$$

Further simplification gives

$$I_\nu(\tau_\nu = 0) - e^{-\tau_\nu}I_\nu(\tau_\nu) = -\int_{\tau_\nu}^{0} e^{-\tau_\nu}B_\nu(T)\,\mathrm{d}\tau_\nu \tag{2.30}$$

[1] The negative sign indicates that from the observer's point-of-view $\tau_\nu$ decreases as $x$ increases — see Figure 2.1

or

$$I_\nu(\tau_\nu = 0) = e^{-\tau_\nu} I_\nu(\tau_\nu) + \int_0^{\tau_\nu} e^{-\tau_\nu} B_\nu(T)\, \mathrm{d}\tau_\nu \tag{2.31}$$

or explicitly in terms of depth within the plasma (see Figure 2.1),

$$I_\nu(x) = e^{-\tau_\nu(x)} I_\nu(x = 0) + \int_0^{\tau_\nu(x)} e^{-\tau_\nu(x)} B_\nu(T)\, \mathrm{d}\tau_\nu. \tag{2.32}$$

If there is far-side background radiation $I_\nu(x = 0)$, the first term on the right-hand-side of Equation 2.32 accounts for its attenuation as it traverses the plasma. The second term accounts for the emission and attenuation of radiation from the plasma itself. Given this plasma is isothermal, the integral in Equation 2.32 is a difference equation resulting in

$$I_\nu = e^{-\tau_\nu} I_\nu(x = 0) + B_\nu(T)\left(1 - e^{-\tau_\nu}\right). \tag{2.33}$$

Ignoring background radiation, we have, finally, the simplest radiative transfer model of an HII region,

$$I_\nu = B_\nu(T)\left(1 - e^{-\tau_\nu}\right). \tag{2.34}$$

For an optically thick plasma, $\tau_\nu \gg 1$ and Equation 2.34 simplifies to

$$I_\nu = B_\nu(T), \tag{2.35}$$

predicting that the observed brightness is Planck's brightness distribution, Equation 2.18. Using Rayleigh-Jeans' approximation of this distribution (Equation 2.19) predicts $I_\nu \propto \nu^2$, consistent with the low-frequency portion of Figure 2.2.

For an optically thin plasma, $\tau_\nu \ll 1$ and Equation 2.34 simplifies to

$$I_\nu = \tau_\nu B_\nu(T). \tag{2.36}$$

Combining Equation 2.19 and the approximation to the continuum absorption coefficient Equation 2.22 predicts $I_\nu \propto \nu^{-0.1}$, which is consistent with the high-frequency portion of Figure 2.2.

### 2.1.4 Spectral line emission & absorption

Equations 2.116, 2.130, 2.131 and 2.132 of Gordon and Sorochenko (2009) give an expression for the non-LTE line absorption coefficient $\kappa_L(\nu)$ at radio

frequencies used by our Orion nebula model,

$$\kappa_{\mathrm{L}}(\nu) = \kappa_{\mathrm{L}}^{*}(\nu)\, b_{n_1} \beta \tag{2.37}$$

$$\kappa_{\mathrm{L}}(\nu) = \kappa_{\mathrm{L}}^{*}(\nu)\, b_{n_1} \left[ \frac{1 - \left( \frac{b_{n_2}}{b_{n_1}} \right) e^{-h\nu/kT_e}}{1 - e^{-h\nu/kT_e}} \right] \tag{2.38}$$

$$\kappa_{\mathrm{L}}(\nu) \approx \kappa_{\mathrm{L}}^{*}(\nu)\, b_{n_1} \left[ 1 - \frac{kT_e}{h\nu} \frac{\mathrm{d} \ln b_{n_2}}{\mathrm{d}n} \Delta n \right] \tag{2.39}$$

where

$$\kappa_{\mathrm{L}}^{*}(\nu) \approx 3.469 \times 10^{-12} \phi(\nu) \Delta n \frac{f_{n_1,n_2}}{n_1} \left( 1 - \frac{3\Delta n}{2n_1} \right) \frac{N_e^2}{T_e^{5/2}} \exp\left( \frac{E_{n_1}}{kT_e} \right), \tag{2.40}$$

is the LTE line absorption coefficient and $\phi(\nu)$ is the line profile, $\Delta n = n_2 - n_1$ is the principal quantum number transition-order, $f_{n_1,n_2}$ is the oscillator strength of the transition, $n_1$ is the lower electronic quantum state and $E_{n_1}$ is the energy of this state, where (Bohr, 1913)

$$E_{n_1} = -\frac{2\pi^2 m e^4}{(nh)^2}. \tag{2.41}$$

From Equation 2.133 of Gordon and Sorochenko (2009), the non-LTE line emission coefficient is

$$j_{\mathrm{L}} = \kappa_{\mathrm{L}}^{*}(\nu)\, b_{n_2} B_{\nu}(T_e).$$

A useful approximation for $f_{n_1,n_2}$ is given by Menzel (1968) as

$$f_{n_1,n_2} \approx n_1 M_{\Delta n} \left(1 + 1.5\frac{\Delta n}{n_1}\right), \tag{2.42}$$

where $M_{\Delta n}$ is given in Table 2.1 for $\Delta n \leq 10$.

**Table 2.1:** Oscillator strengths $f_{n_1,n_2} \approx n_1 M_{\Delta n} \left(1 + 1.5\frac{\Delta n}{n_1}\right)$

| $\Delta n$ | $\log_{10}(M_{\Delta n})$ |
|---|---|
| 1 | -0.7194788 |
| 2 | -1.5795145 |
| 3 | -2.0912138 |
| 4 | -2.4569656 |
| 5 | -2.7418778 |
| 6 | -2.9753214 |
| 7 | -3.1730976 |
| 8 | -3.3446790 |
| 9 | -3.4962080 |
| 10 | -3.6318861 |

A more accurate expression for $f_{n_1,n_2}$ is given by Menzel and Pekeris (1935) as

$$f_{n_1,n_2} = g_{n_1,n_2} f'_{n_1,n_2}, \tag{2.43}$$

where $g_{n_1,n_2}$ is a correction factor for $f'_{n_1,n_2}$,

$$f'_{n_1,n_2} = \frac{2^6}{3\sqrt{3}\pi} \frac{1}{\omega'_n} \frac{1}{\left(\frac{1}{n_1^2} - \frac{1}{n_2^2}\right)} \left(\frac{1}{n_1 n_2}\right)^3. \tag{2.44}$$

An approximation for $g_{n_1,n_2}$ that corrects $f'_{n_1,n_2}$ to within 0.5% of the exact solution is given by Burgess and Summers (1976) as

$$g_{n_1,n_2} \approx 1 - T_4 \left( T_1 G_1 + T_2 G_2 + T_3 G_3 \right), \tag{2.45}$$

where

$$G_1 = \left( 0.203 + \frac{0.256}{n_2^2} + \frac{0.257}{n_2^4} \right) n_2, \tag{2.46}$$

$$G_2 = 0.17 n_2 + 0.18, \tag{2.47}$$

$$G_3 = \left( 0.2214 + \frac{0.1554}{n_2^2} + \frac{0.37}{n_2^4} \right) n_2, \tag{2.48}$$

$$T_1 = \left( 2n_1 - n_2 \right) \left( n_1 - n_2 + 1 \right), \tag{2.49}$$

$$T_2 = 4 \left( n_1 - 1 \right) \left( n_2 - n_1 - 1 \right), \tag{2.50}$$

$$T_3 = \left( 2n_1 - n_2 - 0.001 \right) \left( n_1 - 0.999 \right), \tag{2.51}$$

$$T_4 = \frac{1}{\left( n_2 - 1.999 \right)^2} \frac{1}{n_2 n_1^{2/3}} \left( \frac{n_2 - 1}{n_2 - n_1} \right)^{2/3}. \tag{2.52}$$

Feron (2013) has verified the 0.5% claim for $\Delta n < 10^3$ using arbitrary precision arithmetic (Fousse et al., 2007) to exactly calculate the hypergeometric function that arises when finding $f_{n_1,n_2}$ (Hoang-Binh, 1990).

## 2.2 Broadening mechanisms of radio recombination lines

Three known spectral line broadening mechanisms determine the shapes and widths of spectral lines, whether in emission or absorption. In the following sections I review natural, Doppler, and Stark broadening mechanisms. It is shown that the contribution of natural broadening to the measured widths of RRLs is negligibly small compared with the other two mechanisms.

### 2.2.1 Natural broadening

Before the development of quantum mechanics theory, atoms were modeled as oscillating electric dipoles. The energy of an oscillator decreases as $E(t) = E_0 \exp(-\Gamma t/2)$, where the damping constant is $\Gamma = \dfrac{8\pi^2 e^2}{3 m_e c^3} \nu_0$ and $\nu_0$ is the oscillation frequency. Lorentz (1906) showed that this damping determines the frequency spectrum of the oscillator to be

$$\phi(\nu) \propto \frac{\Gamma/\pi}{\pi \left[ 4(\nu - \nu_0)^2 + \left( \dfrac{\Gamma}{2\pi} \right)^2 \right]}, \tag{2.53}$$

where the FWHM (full width at half maximum) of this profile is $\Delta\nu_{\rm L} = \Gamma/2\pi$.

Quantum mechanics predicts that spectral lines have a *natural width* imposed by

Heisenberg's uncertainty principle (Heisenberg, 1927). This principle predicts that the uncertainty in time and energy measurements are related by

$$\Delta E \Delta t \gtrsim \hbar. \tag{2.54}$$

If the lifetime of an excited electronic state is $\Delta t$, the energy of this state can be determined with an uncertainty of $\Delta E \approx \frac{\hbar}{\Delta t}$. The uncertainty in the energy depends on the lifetimes of the upper *and* lower states, $n_2$ and $n_1$. The natural width of a spectral line is defined as

$$\gamma = \frac{\Delta E_{n_2}}{\hbar} + \frac{\Delta E_{n_1}}{\hbar} = \frac{1}{t_{n_2}} + \frac{1}{t_{n_1}} \equiv \Gamma_{n_2} + \Gamma_{n_1} \tag{2.55}$$

The total spontaneous rates out of levels $n_2$ and $n_1$ are

$$\Gamma_{n_2} = \sum_{n_1=1}^{n_2-1} A_{n_2,n_1}, \tag{2.56}$$

$$\Gamma_{n_1} = \sum_{n_0=1}^{n_1-1} A_{n_1,n_0}, \tag{2.57}$$

where $A_{n',n}(\mathrm{s}^{-1})$ is the rate of spontaneous emission from upper level $n'$ to lower level $n$.

The FWHM is

$$\Delta\nu_{\rm L} = \frac{\Gamma}{2\pi} = \frac{1}{2\pi}\left(\Gamma_{n_2} + \Gamma_{n_1}\right) = \frac{1}{2\pi}\left(\sum_{n_1=1}^{n_2-1} A_{n_2,n_1} + \sum_{n_0=1}^{n_1-1} A_{n_1,n_0}\right), \tag{2.58}$$

which is the quantum mechanical form of the Lorentz width found by Weisskopf and Wigner (1930). Given $\Gamma_n$ are approximately the same for lower and upper levels of RRLs at large $n$, with $(n_2 - n_1) \ll (n_2, n_1)$, Equation 2.58 can be approximated as

$$\Delta\nu_{\rm L} \approx \frac{1}{\pi}\sum_{n_1=1}^{n_2-1} A_{n_2,n_1}. \tag{2.59}$$

From Sobel'man et al. (1995), the sum in this equation can be approximated as

$$A_n = \sum_{n_1=1}^{n_2-1} A_{n_2,n_1} \approx 2.4\times10^{10}\frac{\ln n}{n^5},\ \ n > 20. \tag{2.60}$$

Using this equation and Equation 1.1 with $\Delta n = 1$ as an approximation for RRL frequency $\nu_0$, then Equation 2.59 estimates the natural width of RRLs:

$$\frac{\Delta\nu_{\rm L}}{\nu_0} \approx \frac{2.4\times10^{10}}{2\pi Rc}\frac{\ln n}{n^2} \approx 1.2\times10^{-6}\frac{\ln n}{n^2},\ \ n > 20. \tag{2.61}$$

As an example, this predicts that the fractional natural width for the H100$\alpha$ line is $\Delta\nu_{\rm L}/\nu_0 \approx 5.3\times10^{-10}$. Using Equation 2.63, the natural width of this line is

$\Delta v_{\mathrm{L}} = 1.6 \times 10^{-4}\,\mathrm{km/s}$, which, as is shown below, is negligibly small compared with Doppler and Stark broadening.

### 2.2.2 Doppler broadening

#### 2.2.2.1 Thermal broadening

Excluding turbulence, cosmic thermal gases are modeled as Maxwell-Boltzmann velocity distributions. Given the high rate of collisions between electrons and ions, any perturbation in the velocity distribution will get thermalized in minutes for typical HII regions, $T_e = 10^4\,\mathrm{K}$ and $N_e = 10^4\,\mathrm{cm}^{-3}$ (Gordon and Sorochenko, 2009).

For a Maxwell-Boltzmann velocity distribution, the probability of a gas atom having a velocity component between $v_x$ and $v_x + \mathrm{d}v_x$ along a line of sight through the nebula is

$$N(v_x)\,\mathrm{d}v_x = N\sqrt{\frac{M}{2\pi kT}}\exp\left(-\frac{Mv_x^2}{2kT}\right)\mathrm{d}v_x, \tag{2.62}$$

where $N$ is the total number of atoms contributing spectral line photons and $M$ is the atom mass (Gordon and Sorochenko, 2009). Using the Doppler formula

to relate the observed frequency shift to the line-of-sight velocity shift

$$\mathrm{d}v_x = c\,\frac{\mathrm{d}\nu}{\nu_0}, \tag{2.63}$$

Equation 2.62 is converted to line intensity $I_\nu$. This assumes that the total intensity in the line is proportional to the number of emitters $N$ in the antenna beam and that the gas is optically thin, which means the intensity $\mathrm{d}I_\nu$ is proportional to $\mathrm{d}N(v_x)$. The result is $I_\nu = I_0\phi_\mathrm{G}(\nu)$, where the line profile $\phi_\mathrm{G}$ of the Doppler-broadened line is

$$\phi_\mathrm{G}(\nu) = \sqrt{\frac{4\ln 2}{\pi}}\frac{1}{\Delta\nu_\mathrm{G}}\exp\left(-4\ln 2\left(\frac{\nu_0-\nu}{\Delta\nu_\mathrm{G}}\right)^2\right), \tag{2.64}$$

where $\Delta\nu_\mathrm{G}$ is the FWHM of the thermally broadened Gaussian line.

$\Delta\nu_\mathrm{G}$ is found by equating the exponential arguments of Equation 2.62 and Equation 2.64. Using Equation 2.63 to relate velocity to frequency, the width is

$$\Delta\nu_\mathrm{G} = \sqrt{4\ln 2}\sqrt{\frac{2kT}{Mc^2}}\nu_0. \tag{2.65}$$

For a typical HII region of $T = 10^4$ K and using the mass of hydrogen, Equation 2.65 gives a fractional Doppler width of $\Delta\nu_\mathrm{G}/\nu_0 \approx 7\times10^{-5}$. This is 100,000 times greater than the corresponding fractional natural width of the H100$\alpha$ line calculated above and corresponds to a Doppler width of $\Delta v_\mathrm{G} \approx 21\,\mathrm{km/s}$ using

Equation 2.63.

#### 2.2.2.2 Turbulence

Turbulence also contributes to the Doppler component of RRLs (Strelnitski et al., 2002). HII regions contain cells of gas moving relative to one another. If these cells are unresolved by a radio telescope, it is called microturbulence. Given that the velocity distribution of these cells are found to be Gaussian, the observed width can be modeled as the convolution of thermal and turbulence Gaussians. This results in another Gaussian profile whose width is

$$(\Delta v_{\mathrm{G}'})^2 = (\Delta v_{\mathrm{G-thermal}})^2 + (\Delta v_{\mathrm{G-turbulence}})^2, \tag{2.66}$$

such that the Doppler line width can be expressed as

$$\Delta V_{\mathrm{G}} \equiv \Delta v_{\mathrm{G}'} = \sqrt{4\ln 2}\sqrt{\frac{2kT}{M} + V_{\mathrm{T}}^2}, \tag{2.67}$$

where $V_{\mathrm{T}}$ is turbulence velocity (Gordon and Sorochenko, 2009). For example, if $V_{\mathrm{T}} = 15\,\mathrm{km/s}$ and $T = 10^4\,\mathrm{K}$, the resulting FWHM of H100$\alpha$ due to the Doppler mechanism is $\Delta V_{\mathrm{G}} \approx 25.8\,\mathrm{km/s}$, instead of $\approx 21\,\mathrm{km/s}$ calculated in the previous subsection.

### 2.2.3 Stark broadening

Also known as pressure broadening, Stark broadening arises from the Stark effect discovered by Stark (1913). When an atom is in the presence of an external electric field, it's atomic energy levels are observed to split and displace. The Stark effect appears differently depending on the strength of the electric field. When a bound electron is in a non-circular orbit (a Rydberg state), an electric dipole moment results which interacts with the electric field. This is called a *linear* Stark effect when the observed displacement of emission lines is linearly proportional to the electric field strength. It is called a *quadratic* Stark effect when the displacement is proportional to the square of the electric field strength. Weak fields produce a linear Stark effect, while strong fields produce a quadratic Stark effect.

If the atomic energy levels $n$ of an atom are based on the quantization of the orbital angular momentum of its electrons, Bohr (1913) showed that

$$E_n = \frac{2\pi^2 me^4}{h^2}\frac{Z^2}{n^2}, \tag{2.68}$$

where $m$ is the mass of the electron, $e$ is its charge and $Ze$ is the charge of the nucleus.

Using Equation 2.68, Bohr (1922) predicted that an applied external electric

field $\mathscr{E}$ causes the energy level of an atom to change by

$$\Delta E = \frac{3h^2\mathscr{E}}{8\pi^2 em} n n_{\rm f}, \tag{2.69}$$

where $n_{\rm f} = 0, \pm 1, \pm 2, \ldots, \pm n$. This leads to $2n-1$ sublevels with the maximum energy change proportional to $n^2$ for each energy level $E_n$. Stark shifted lines are modeled as transitions from the split upper-energy levels $E_{n_u} \pm \Delta E$ to the split lower-energy levels $E_{n_l} \pm \Delta E$ (Gulyaev, 1976).

In the ISM, Stark broadening is more complex. Plasmas associated with the ISM are characterized by ultra low density compared with terrestrial plasmas and stellar cores. The electric field experienced by emitting atoms in the ISM is modeled as a series of brief, weak and time varying transient fields induced by successive collisions with electrons,[2] instead of a constant field as described above. The former scenario is called *electron-impact* Stark broadening and the latter is called *quasi-static* Stark broadening. Here, I focus on impact broadening.[3]

[2] The importance of electron collisions in many environments is well known, arising from the fact that electrons are always the most abundant charged particle and have a much higher thermal velocity than atoms, leading directly to a higher collision rate (Barklem et al., 2011).

[3] In-depth discussion of the quasi-static Stark broadening approximation is found, among others, in Peach (1975); Mihalas (1978).

#### 2.2.3.1 Impact broadening

Impact broadening can be interpreted as a consequence of finite lifetimes in quantum states owing to collisions. In subsection 2.2.1 I considered natural broadening and showed that the lifetime for an unperturbed atom in state $n$ is determined by the probability of spontaneous decay $A_n$, Equation 2.60. When collisions are important, it is the probability of collisions that determines the lifetime of an atom in a given state, i.e., the coefficients $C_{n,n'}$ and $C_{n,i}$ in Equation 2.7.

Considering collisions with radiating atoms, not only strong collisions that interrupt radiation should be taken into account, but also multiple weak collisions, which cause deformation of the wave train in the sense of its phase disruption.

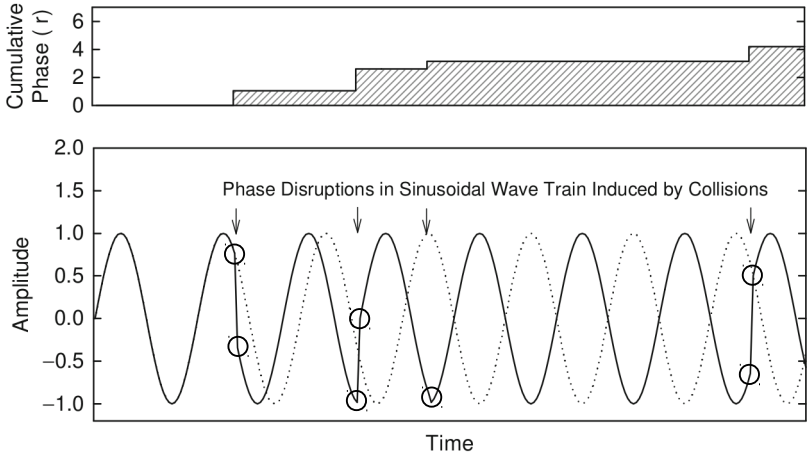


**Figure 2.3:** Impact broadening model. *Bottom*: the dotted line is an unperturbed sinusoidal wave train as function of time. The solid line is the wave train perturbed by brief collisions. *Top*: cumulative phase shifts in radians as a function of time. Figure from Gordon and Sorochenko (2009). The circles are added showing when collisions occur.

Figure 2.3 shows the effect of brief small phase shifts upon a sinusoidal wave-train. The effect of these collisions redistributes power about the central frequency of the electromagnetic wave, thereby increasing the associated spectral line width. The Fourier transform relationship between the phase-shift time-history and frequency dispersion is the spectral line profile.

As an example, consider the spectral line shape resulting from an oscillator of constant amplitude that is briefly interrupted due to successive collisions. If the oscillation is $f(t) = \exp(i2\pi\nu_0 t)$ over the duration $T$ between successive collisions that briefly halt the oscillator, then the frequency spectrum of the os-

cillation is the Fourier transform of $f(t)$:

$$F(\nu) = \int_{-\infty}^{\infty} f(t) e^{-i2\pi\nu t} \mathrm{d}t = \int_{0}^{T} e^{i2\pi\nu_0 t} e^{-i2\pi\nu t} \mathrm{d}t = \int_{0}^{T} e^{i2\pi t(\nu_0-\nu)} \mathrm{d}t$$
$$= \frac{e^{i2\pi T(\nu_0-\nu)} - 1}{i2\pi(\nu_0-\nu)}, \tag{2.70}$$

where $F(\nu)$ is the complex spectrum for the duration $T$.

If collisions are Gaussian distributed during time $T$ with a mean time $\tau$ between collisions, then the probability of a collision is $P(T) = \exp(-T/\tau)/\tau$. The resulting spectral profile $\phi(\nu)$ is the average power spectrum $\left|F^2 P\right|$ over the distribution of $T$:

$$\phi(\nu) \propto \int_{0}^{\infty} F^*(\nu,T) F(\nu,T) \frac{e^{(-T/\tau)}}{\tau} \mathrm{d}T = \frac{2\Delta\nu_\mathrm{L}}{\pi\left[4(\nu-\nu_0)^2 + (\Delta\nu_\mathrm{L})^2\right]} \tag{2.71}$$

after normalization, $\int_{-\infty}^{\infty} \phi(\nu)\,\mathrm{d}\nu = 1$.

Like Equation 2.53, Equation 2.71 is a Lorentz profile with FWHM $\Delta\nu_\mathrm{L} = \dfrac{\Gamma}{2\pi}$, where $\Gamma$ is related to probabilities of collisional transitions $C_{n,n'}$ and $C_{n,i}$ (see subsection 2.1.1 and Equation 2.7). Therefore, this model of an emitting atom disrupted by collisions predicts a Lorentzian spectral line profile.

The phase disruption $\Delta\phi$ induced by a perturber is modeled in terms of a minimum distance or "impact parameter" between the perturber and atom (Weisskopf, 1932). Figure 2.4 shows a charged particle passing an emitting atom at

constant velocity $v$ and minimum distance $\rho$.

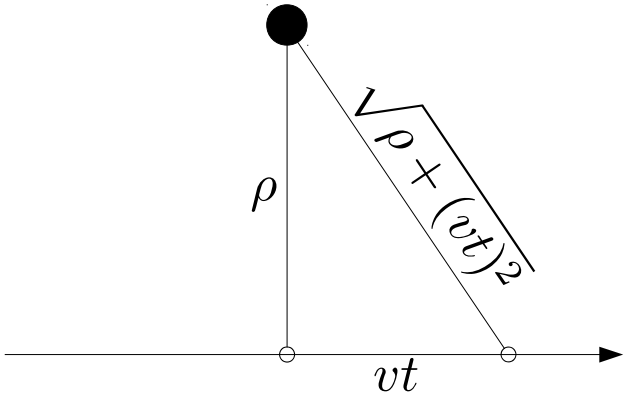


**Figure 2.4:** Impact geometry. Perturber of velocity $v$ passing within a distance $\rho$ of an emitting atom.

At any instant of time, it is assumed that the shift in the angular frequency of emission $\Delta\omega$ is modeled by a power law

$$\Delta\omega = \frac{C_s}{R^s}, \tag{2.72}$$

where $R(t)$ is the distance between the atom and perturber, $s$ is the strength of the relationship between distance and frequency shift, and $C$ the constant of proportionality. From Figure 2.4, $R = \sqrt{\rho^2 + (vt)^2}$, where $vt$ is the linear distance traveled by the perturber since its closest approach along a straight-line trajectory.

A shift in the angular frequency of emission is $\Delta\omega = \dfrac{\Delta\phi}{\Delta t}$. Therefore, the total

phase shift of the wave train caused by a perturbation event is

$$\Delta\phi = \int_{-\infty}^{\infty} \Delta\omega \, \mathrm{d}t = \int_{-\infty}^{\infty} \frac{C_s}{(\rho^2 + v^2 t^2)^{s/2}} \, \mathrm{d}t = \alpha_s \frac{C_s}{v\rho^{s-1}}, \tag{2.73}$$

where $\alpha_s = \pi, 2, \pi/2, 4/3, 3\pi/8, \ldots$ for $s = 2, 3, 4, 5, 6, \ldots$.

The value of the impact parameter $\rho$ for $\Delta\phi = 1$ radian follows from Equation 2.73 as

$$\rho_0 = \left( \frac{\alpha_s C_s}{v} \right)^{1/(s-1)} \tag{2.74}$$

and is called the *Weisskopf radius*. $s = 2, 3, 4, 6$ corresponds to the linear Stark effect, resonance broadening, the quadratic Stark effect, and van der Waals broadening, respectively. The Weisskopf radius is used to quantitatively distinguish between strong and weak perturbations of the emitting atoms.

A unified theory of Stark broadening that subsumes quasi-static and impact approximations does not yet exist due to diverse conditions observed within cosmic plasmas. Of the two approximations, electron-impact Stark broadening is found to predict the observed behavior of high-order RRLs (Alexander and Gulyaev, 2016), reproduced in Section 4.2.[4]

If the total phase shift $\Delta\phi$ is caused by an accumulation of discrete phase shifts

[4] In-depth discussion of the Stark broadening quasi-static approximation is found, among others, in Peach (1975); Mihalas (1978).

while an atom radiates, then the impact model describes perturbations due to collisions. The impact approximation model makes the following assumptions (Sobel'man et al., 1995):

1. An impact involves one perturber and one atom at a time, a binary interaction.

2. While an atom is radiating, it experiences a series of discrete and weak collisions. The duration of each collision is much less than the interval between them.

3. Each collision causes an instantaneous phase shift in the electromagnetic wave train. Between collisions, the wave-train oscillation continues unperturbed.

4. The temporal distribution of the collisions is described by a probability function.

The theory of impact broadening for spectral lines in plasmas originated in the 1950's to address optical transitions (Anderson, 1949; Griem et al., 1959; Griem, 1960). These works indicate that collisions with electrons cause line broadening at low electron densities characteristic of cosmic plasmas. Calculations from these works were used to predict Stark broadening effects in RRLs shortly before their detection in 1964. It was found that electron-impact Stark broadening would be significant for $n > 100$ RRLs (Sorochenko and Borodzich,

1965). In Section 4.2 I show that electron-impact broadening theory accurately predicts observed RRL widths.

This theory (Griem, 1967) predicts the Lorentzian width of a RRL to be

$$w_{\mathrm{L}} \propto n^4 \ln\left(\frac{\rho_{\max}}{\rho_{\min}}\right) \propto n^{\beta}, \tag{2.75}$$

where $\beta$ depends on the choice of maximum, $\rho_{\max}$, and minimum, $\rho_{\min}$, cut-off radii (impact parameters). The minimum cut-off radius is typically chosen as

$$\rho_{\min} = \sqrt{\frac{5}{6}}\frac{n^2\hbar}{mv_e}, \tag{2.76}$$

where $\hbar$ is Planck's constant, and $m$ and $v_e$ are electron mass and velocity (Griem, 1967).

There are different approaches with respect to the choice of $\rho_{\max}$ leading to different dependences of the electron-impact width on $n$. If

$$\rho_{\max} = \frac{v_e}{\omega_{n,n\pm1}} \propto n^3, \tag{2.77}$$

where $\omega_{n,n\pm1} = 2\pi\nu_{n,n\pm1}$ is the angular frequency of transition $n \rightarrow n\pm1$ (Griem, 1967), substitution of Equation 2.76 and Equation 2.77 into Equation 2.75 results in $\rho_{\max}/\rho_{\min} \propto n$ and $\beta > 4$. For a typical HII region electron temperature

of $T_e = 10^4\,\mathrm{K}$, Equation 2.75 predicts

$$w_\mathrm{L} \propto n^{4.4} \tag{2.78}$$

for $n \rightarrow n \pm 1$ transitions ($n \gg 1$) (Griem, 1967).

If the Debye radius $R_\mathrm{D}$ is used instead as the maximum cut-off radius, then

$$\rho_\mathrm{max} = R_\mathrm{D} = \sqrt{\frac{kT_e}{8\pi N_e e^2}}, \tag{2.79}$$

where $k$ is the Boltzmann constant and $e$ is the elementary charge (Hey, 2012; Peach, 2015); in this case, $\rho_\mathrm{max}/\rho_\mathrm{min} \propto n^{-2}$ and $\beta < 4$.

For a typical HII region electron density of $N_e = 10^4\,\mathrm{cm}^{-3}$, Equation 2.75 predicts $w_\mathrm{L} \propto n^{3.97}$ (Peach, 2015). Watson (2006) provides a theoretical expression for electron-impact widths valid for $n \leq 70$. His proposed formula for $n > 70$ (Equations (16) and (17) in Watson (2006) results in $w_\mathrm{L} \propto n^{3.97}$, consistent with theoretical results of Peach (2015).

Peach (2015) also tests a stronger condition, the NN (nearest neighbor) radius $R_\mathrm{NN}$ as the maximum cut-off radius,

$$\rho_\mathrm{max} = R_\mathrm{NN} = \left(\frac{3}{4\pi N_e}\right)^{1/3}. \tag{2.80}$$

Gee et al. (1976) provides a useful approximation for collisional cross-sections for inelastic electron impacts. Using a power law presentation, one can write

$$\langle \sigma(n)v \rangle \propto n^{\gamma}. \tag{2.81}$$

The collisional line width for the transition $n+\Delta n \rightarrow n$ is then

$$w_{\rm L} = N_e \left[ \langle \sigma(n+\Delta n)v \rangle + \langle \sigma(n)v \rangle \right] \propto N_e n^{\gamma} \left( 1 + \frac{\gamma}{2}\frac{\Delta n}{n} + \frac{\gamma(\gamma-1)}{2\cdot 2!}\left(\frac{\Delta n}{n}\right)^2 + \ldots \right), \tag{2.82}$$

using a Taylor series expansion (Sobel'man et al., 1995). The first two terms of this expansion in Equation 2.82 were used by Smirnov et al. (1984) in their approximate formula for the Lorentz width (Equation (2.60) in Gordon and Sorochenko (2009)),

$$w_{\rm L} = 8.2 N_e \left(\frac{n}{100}\right)^{\gamma} \left( 1 + \frac{\gamma}{2}\frac{\Delta n}{n} \right) \propto n^{\beta}. \tag{2.83}$$

For H$n\alpha$ lines, one can ignore the difference between exponents $\beta$ and $\gamma$ used in different presentations of the line width (cf. Equation 2.75 and Equation 2.82); for example, if $n = 100$ the exponent $\beta = 4.41$ when $\gamma = 4.40$. However, when considering the widths of the sequence of high-order RRLs, the difference between $\beta$ and $\gamma$ should be taken into account. For example, for my sequence

of RRLs at 6 GHz, $\beta = 4.50$ when $\gamma = 4.40$. For the interval $\beta = 3.8...4.5$ considered here, the relationship

$$\beta - \gamma = 0.10 \tag{2.84}$$

holds for the high-order RRL series. This is used below when comparing my results with theoretical findings of Griem (1967); Gee et al. (1976); Watson (2006); Peach (2015) and with observational data of Smirnov et al. (1984); Bell et al. (2011).

To extract Lorentz widths $w_{\rm L}$ (FWHM) from the observed high order RRL profiles, I use the approximate formula of Kielkopf (1973) presented by Smirnov (1985) as

$$w_{\rm L} = 7.786\, w_{\rm V} \left[ 1 - \sqrt{1 - 0.240 \left( 1 - (w_{\rm D}/w_{\rm V})^2 \right)} \right], \tag{2.85}$$

where $w_{\rm V}$ is the Voigt width (FWHM) of the spectral line determined by the fitting procedure and $w_{\rm D}$ is the Doppler width (FWHM). Given Lockman and Brown (1975)'s Orion nebula model has a temperature gradient, Doppler widths are different for different regions, so the Doppler width $w_{\rm D}$ used in Equation 2.85 is an "effective" Doppler width. For my observations at $5.5 - 6.5\,$GHz, the intermediate (second) region of the modified and original (Lockman and Brown,

1975) models dominates in terms of RRL and continuum flux, so the effective Doppler width is close to that of the intermediate region.

# 3 Methodology: observations & processing of ATCA/CABB data

"A man should learn to detect and watch that gleam of light which flashes across his mind from within, more than the lustre of the firmament of bards and sages. Yet he dismisses without notice his thoughts, because it is his. In every work of genius we recognize our own rejected thoughts..." *Ralph Waldo Emerson (1803-1882)*

## 3.1 Observations

We observed the central brightest continuum region of M42 (RA = 05:35:17.3, Dec = −05:23:28, J2000) at 6 GHz using the ATCA between 2013 late June

and early July. Over three consecutive days of observing, we obtained about 17 hours of integration. Accounting for calibration overheads, I obtained about 15 hours of integration on M42. The upper plot in Figure 3.1 shows the 5.5 $\rightarrow$ 6 GHz bandpass without bandpass calibration from day two of a total of three days of observations. The three circles in this upper plot, from left to right, indicate bright H$(n,\alpha)$ and weaker He$(n,\alpha)$ & C$(n,\alpha)$ RRL detections of the $(105,1)$, $(104,1)$ and $(103,1)$ transitions. These narrow lines, and all other detected higher-order RRLs, have widths (FWHM) between $\sim$ 17 channels and $\sim$ 30 channels. This bandpass contains a noticeable ripple with a "period" of $\sim$ 1000 channels. This period is $>$ 30 times greater than the width of the widest RRL we detected (30 channels). The subplot in the bottom right part of the figure is the power spectrum of the bandpass spectrum. The 1000-channel ripple period manifests itself in the power spectrum as a triple peak marked with a large circle. There is also a short-period ($\sim$ 14 channels) ripple shown in the bottom-left subplot in the figure. In the powers spectrum, it corresponds to a peak we mark with a small circle. The shadowed region in the power spectrum corresponds to the range of detected RRL widths (18...40 channels). There are no "competing" statistically significant periodic signals in the shadowed region, which can cause confusion when extracting the detected RRL from the uncalibrated spectrum.

It is suspected that the 1000-channel ripple in the spectrum is due to the standing

waves introduced on all antennas between the focus cabin and the dish surface. It's not surprising to see this on a source which has strong continuum emission. There is no explanation yet for the 14-channel ripple. If it was also due to a standing wave, the required distance between reflections would be around 370 m (Warwick Wilson, 2014, private communication).

We used a 1 GHz bandpass option of the ATCA's Compact Array Broadband Backend (CABB) (Wilson et al., 2011). CABB's wideband mode uses two simultaneous IF (intermediate frequencies), providing two bandpasses, each 544 MHz wide. One IF was centered on 5744 MHz and the other on 6260 MHz, creating a 28 MHz overlap. This enormous bandpass allowed simultaneous observations of multiple RRL with the same $\Delta n$ including six $\alpha$-lines, seven $\beta$-lines, and so on, up to eleven $\Delta n = 5$ lines. The choice of frequency range was dictated by the intention to minimize the number of overlapping RRL in the band.

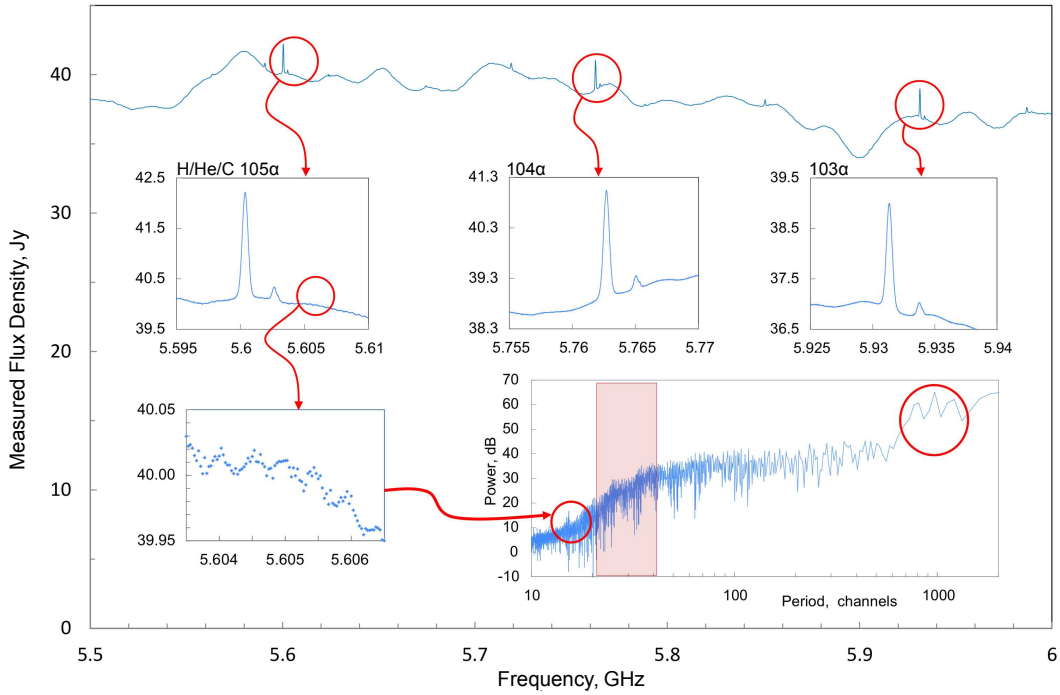


**Figure 3.1:** Bandpass and its power spectrum without bandpass calibration, M42. Shows one of two 0.5 GHz-wide bandpasses *without* bandpass calibration (upper plot). The $x$-axes are frequency in GHz and $y$-axes are flux density, Jy; output of Miriad postprocessing. Bright H$n\alpha$ and weaker He$n\alpha$ & C$n\alpha$ lines are circled and shown as magnified subplots. The spectrum contains a noticeable ripple with a "period" of $\sim$ 1000 channels. The bottom-right subplot shows the power spectrum of the bandpass. The 1000-channel ripple "period" manifests itself as a peak in the power spectrum and is marked with a large circle. There also is a short-period (14-channel) ripple clearly visible in the bottom-left sublpot. Its corresponding peak in the power spectrum is marked with a small circle. The shadowed region in the power spectrum corresponds to the range of detected RRL widths (18...40 channels).

For maximum brightness sensitivity, we used the compact H75 configuration with a beam-size of $7.8'$ per telescope and synthesized beam-size of $1.8' \times 2.1'$ at 6 GHz. At the start of each observation time slot, we observed a primary calibrator, the unresolved (for ATCA) quasar PKS 1934-638 (RA = 19:39:25.0, Dec = $-$63:42:46, J2000; $\sim$ 5 Jy at 6 GHz ) for $\sim$ 15 min and used it to correct

(prior to observing M42) residual delays due to differences in signal propagation times through ATCA's electronic pathways (Fomalont and Perley, 1999). After every 30 min of integration on M42, we observed a secondary calibrator, the quasar PKS 0539-057 (RA = 05:41:38.1, Dec = −05:41:49.43, J2000; $\sim 1$ Jy at 6 GHz) for $\sim 2$ min, to correct time-dependent gain and phase changes over the course of these multi-hour/multi-day observations. Postprocessing was done using Miriad (Sault et al., 1995) and Python's Astropy package (Astropy Collaboration et al., 2013).

Bandpass calibration was initially obtained using the primary calibrator, but find that its S/N, relative to that of the source, M42, is too low for detecting the weakest (highest $\Delta n$) RRL reported here. Figure 3.2 shows a photocopy from one of my notebooks showing M42 bandpass results before and after bandpass calibration when using the PKS 1934-638 data. The relatively low S/N of 1934-638 causes all H($\Delta n > 1$) RRLs to be undetectable when used as bandpass calibrator. Though smoothing the PKS 1934-638 data significantly improves the resulting bandpass calibration, a superior solution was suggested by Peter Thomasson (private communication, 2014). For this reason, PKS 1934-638 is not used as a bandpass calibrator in the analysis presented here.

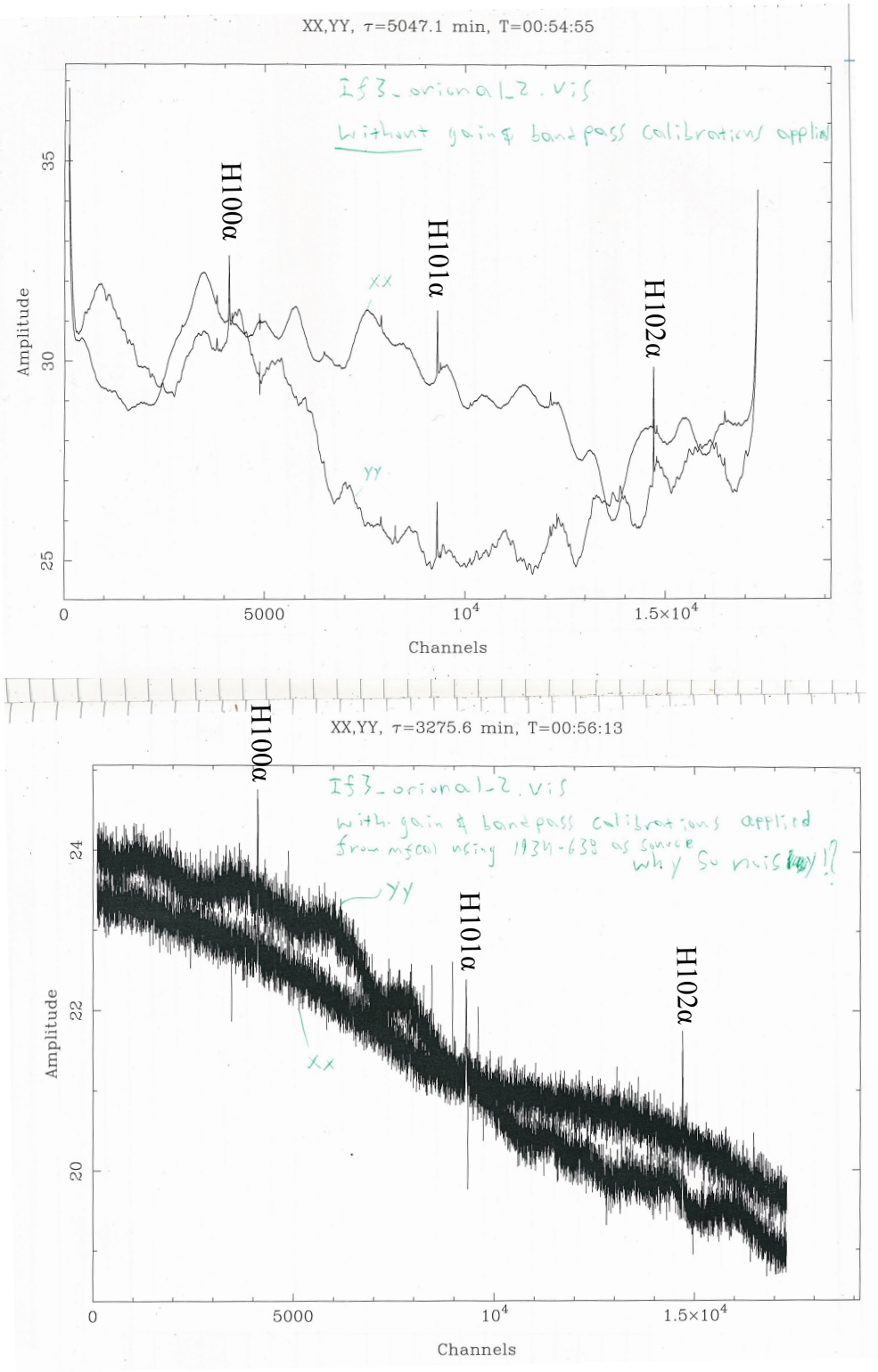


**Figure 3.2:** M42 bandpass using PKS 1934-638 as bandpass calibrator. Bandpass result from day one of three before (*upper* plot) and after (*lower* plot) bandpass calibration of M42 data using the unsmoothed PKS 1934-638 data; x-axes are spectral channels ($\approx 31$ kHz per channel) and y-axes are flux density, Jy; xx and yy polarizations are indicated, as are the predicted positions of H100$\alpha$, H101$\alpha$, H102$\alpha$ RRLs; Red lab book, pages 92-3, August 2013.

Instead, we used the unresolved (for ATCA) quasar PKS 1253-055 (RA = 12:56:11.2, Dec = −05:47:21.5; ∼ 15 Jy at 6 GHz) observed a day prior to the start of the observations reported here — see Section 5.2. Signal-to-noise of this calibrator was further improved by smoothing with a 16 channel moving average window. Flux calibration was obtained using the primary calibrator.

The yy polarization M42 data is significantly noisier than the xx polarization, as shown in Figure 3.2 and Figure 3.3. It is noisier from a channel-to-channel prospective, but more importantly, the yy polarization data contains ripples over a range of wavelengths that are significantly greater in amplitude than the xx polarization data, which do not reduce with time integration. When the yy polarization data is included, sensitivity to the weakest/broadest recombination lines is significantly compromised. For this reason, the yy polarization data is excluded from the analysis reported here.[1]

[1]Because free-free and H bound-bound radiation from HII regions is not significantly polarized, excluding one orthogonal of polarization does not effect spectral line shapes.

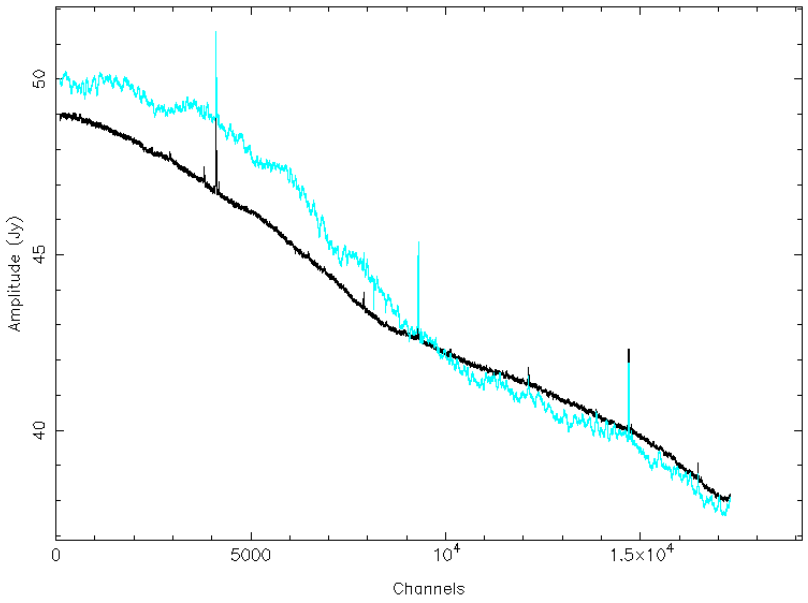


**Figure 3.3:** M42 bandpass 5.5 $\rightarrow$ 6 GHz using PKS 1253-055 as the bandpass calibrator that resulted from the final day of three consecutive observation days. Black curve is the xx polarization and turquoise curve is the yy polarization. The x-axis is spectral channels, where 1 channel width is $\approx$ 31 kHz and y-axis is flux density, Jy.

As discussed in Westpfahl (1999), the S/N of the bandpass calibrator must be similar or greater than the S/N of the source of interest. To improve the S/N of PKS 1253-055 as a bandpass calibrator, a moving average smoothing algorithm was applied to the data. Channel-by-channel data smoothing using a moving-average is not supported by Miriad. To overcome this limitation, we imported the ATCA/CABB data into the interactive high-level general-purpose programming language, Python. This required exporting the data as FITS formatted files from within Miriad and then importing these files into a Python session using the Astropy package (Astropy Collaboration et al., 2013). Finally, the FITS formatted smoothed data were imported back into Miriad to generate the

final bandpasses using the *uvspec* task to generate vector averaged spectra of the smoothed complex visibility datasets. Figure 3.4 shows a pipeline of the RRL data processing implemented in this dissertation.

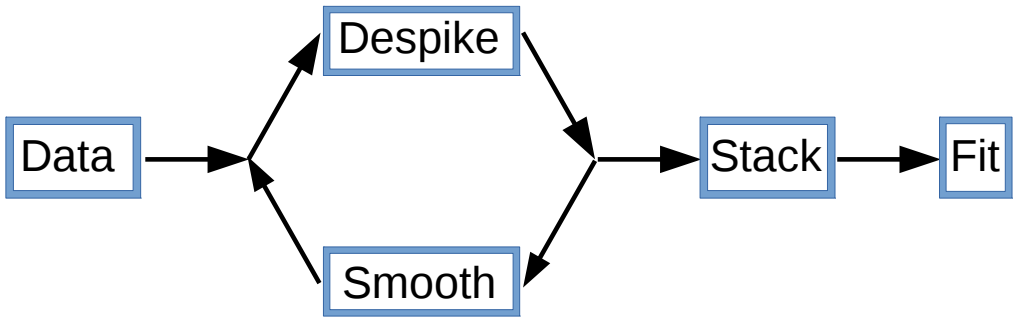


**Figure 3.4:** RRL data processing pipeline. Spectral data is exported from Miriad into Python using FITS formatted files where each ten-second long integration record is despiked and smoothed in a multi-step process. All processed records are imported back into Miriad to generate final bandpasses. All spectra of a given H$\Delta n$ transition are then isolated and stacked after removing those few spectra containing blends with other competing RRL transitions. Stacked results are then fit with Voigt profiles to extract spectral line parameters and their uncertainties.

## 3.2 Data structure

Every ten seconds, the ATCA/CABB produces a ten-second-long integration of the complex visibility data recorded from each of its fifteen baselines. Each record, or spectrum, consists of real and imaginary amplitudes versus 17,409 frequency channels per baseline for xx, yy, xy and yx polarizations. An imported data cube within Python is a multidimensional array; Table 3.1 indicates the structure of this array.

**Table 3.1:** Data cube structure imported into Python from Miriad

| Dimension | 0 | 1 | 2 | 3 | 4 | 5 |
|---|---|---|---|---|---|---|
| quantity | baseline(time) | N/A | N/A | spectral channel | polarization | amplitude |
| # of indices | 15 * (total integraton time) /10 s | 0 | 0 | 17,409 | 4; xx, yy, xy, yx | 3; real, imag, N/A |

## 3.3 Despiking

Figure 3.5 shows a typical raw visibility spectrum, which sparsely contains single bad channels, or "spikes", of enormous amplitude that must be removed before smoothing with a moving average. For example, in Figure 3.5 the spike at channel 4096 will significantly increase the amplitudes of neighboring channels when smoothed, if not initially removed.[2] Spikes are removed by first calculating the median of a given record to find the MAD (median absolute deviation). MAD is significantly less influenced, than the STD (standard deviation), by the enormous spiked deviations present in the visibility data. For example, given that

$$\mathrm{MAD}\,(y) \equiv \mathrm{median}\,(|y_i - \mathrm{median}\,(y)|)\,, \tag{3.1}$$

[2]Spikes on the edges of spectra are unimportant as these data are ignored given the ATCA/CABB data is consistently unreliable here — see Figure 3.5.

where $y_i$ is the amplitude at channel $i$, then, for the spectrum in Figure 3.5, the MAD is more than an order-of-magnitude less than the STD.

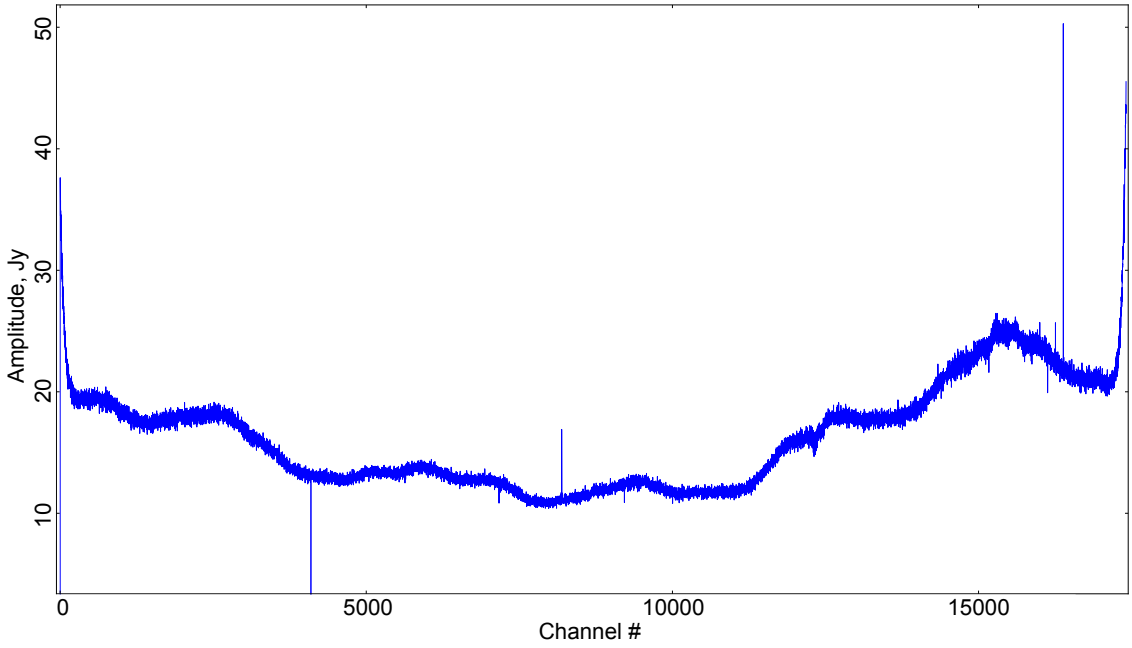


**Figure 3.5:** Typical raw ten second visibility record (real amplitude, xx polarization) showing single bad channels prior to removal and smoothing; amplitudes outside the range of this plot at channels 0 and 4096 are -7317 and -87, respectively. The x-axis is spectral channels, where 1 channel width is $\approx 31\,\mathrm{kHz}$ and y-axis is flux density, Jy.

Leveraging this statistic, the following algorithm is used for despiking and then smoothing the visibility data:

1. Estimate fluctuations as "S/N" per MAD of each channel $i$ using,

$$\mathrm{S/N}_i = \left| \frac{y_i - \mathrm{median}\,(y)}{\mathrm{MAD}\,(y)} \right| \tag{3.2}$$

2. Coarse despiking: locate channels with $\mathrm{S/N}_i$ greater than some $\mathrm{cutoff}_1$ and

set the value of those channels to their nearest-neighbor channel means.

3. Smooth resulting spectrum using a moving average of some window width. Amplitudes of remaining spikes to be removed add significant amplitude to channels within half a window-width centered about each spike during this smoothing step; these artifacts are removed in step 6.

4. Subtract the smoothed spectrum from the unsmoothed spectrum to approximate a spectrum of zero median. Artifacts generated in step 3 are now inverted.

5. Fine despiking: Locate channels with $S/N_i$ greater than $\text{cutoff}_2 < \text{cutoff}_1$ and set the value of these channels to zero.

6. Recover despiked and smoothed bandpass by adding result of step 3 to result of step 5. Artifacts generated in step 3 are significantly removed in this step.

Using the raw spectrum in Figure 3.5, this algorithm is demonstrated as follows. Figure 3.6 shows the result of step 2 and 3, where $\text{cutoff}_1 = 10$ and the window width is 16 channels.

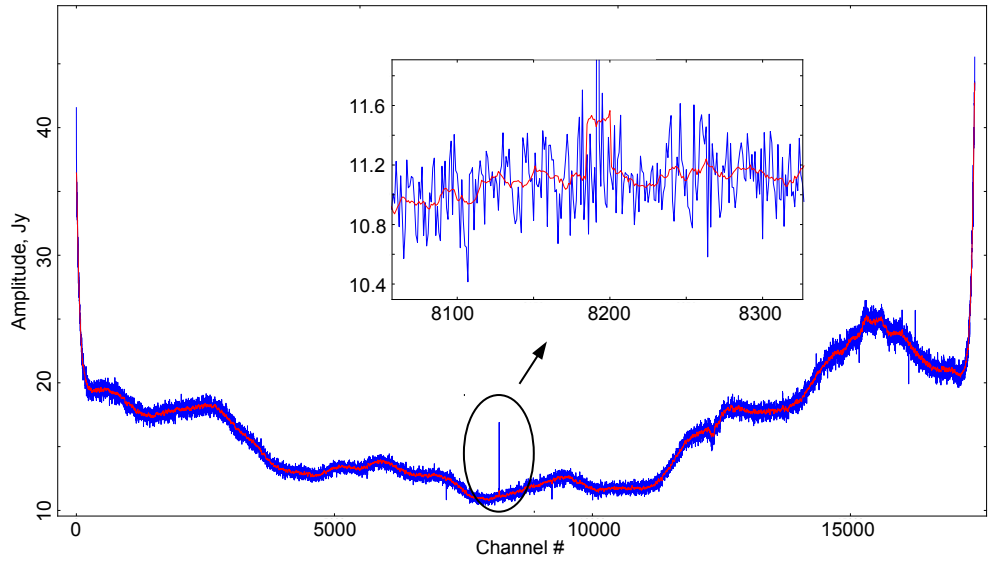


**Figure 3.6:** Raw ten second visibility record (blue line) after coarse despiking and moving average smoothing (red line). Inset plot reveals how moving average is effected by a spike. The x-axes are spectral channels, where 1 channel width is $\approx 31$ kHz and y-axes are flux density units, Jy.

Results of step 4, 5 and 6 are shown in Figure 3.7.

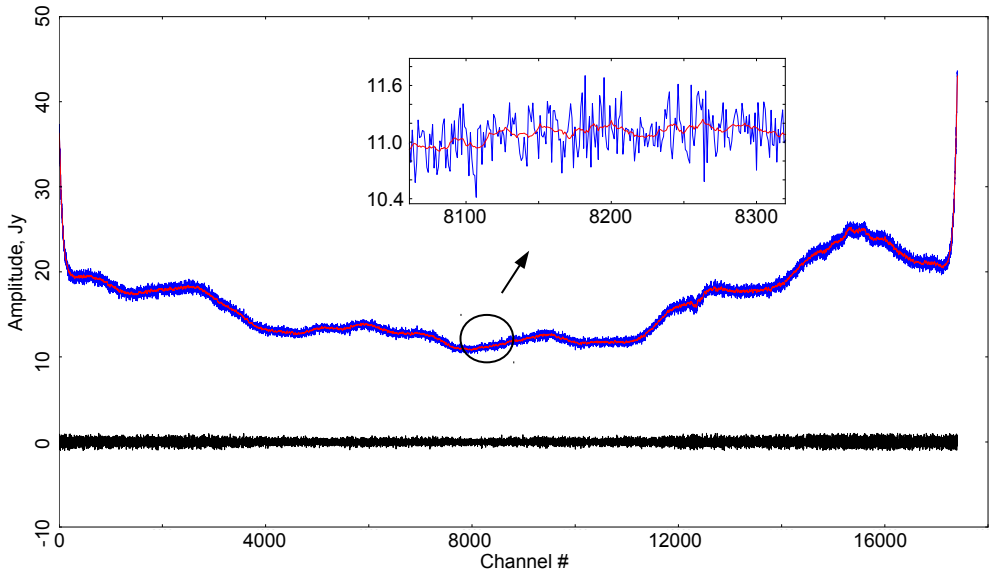


**Figure 3.7:** Raw ten second visibility record (blue line) after fine despiking and updated moving average smoothing (red line). Inset plot reveals how moving average is effected by a spike. The x-axes are spectral channels, where 1 channel width is $\approx 31$ kHz and y-axes are flux density, Jy.

## 3.4 Spectral line stacking

Given the enormous bandpass of the data from 5.5 to 6.5 GHz, the presence of 63 RRLs is predicted for $\Delta n \leq 7$ — Section 4.2, Figure 1. However, given that RRL intensities decrease rapidly as roughly $I_{\Delta n} \propto \Delta n^{-2.5}$ (see section 3.5), statistically significant detections at the highest $\Delta n$ lines require averaging or "stacking" together of individual RRLs of equal $\Delta n$. It turns out that frequency dependent artifacts introduced by stacking are negligible — see Section 4.2, part 2.

In Figure 3.8 to Figure 3.14, I show all bandpasses where RRLs of equal $\Delta n \leq 7$ are predicted, including the stacked bandpasses for each H$\Delta n$ family of principal quantum numbers, $n$. In the case of H $\Delta n = 6$ and $\Delta n = 7$ RRLs, I struggled to convince myself of their detections. The extraction of RRL shape parameters was from fitting Gauss or Voigt functions to spectral features in each bandpass, including each stacked bandpass. Although I found that polynomial plus Voigt profiles resulted in the lowest residuals, extracted line widths were insensitive to the choice of Gauss or Voigt fitting functions.

The fitting results shown in Figure 3.8 to Figure 3.14 are from analysis tools I developed using Scilab, an open-source software for numerical computation (Scilab Enterprises, 2012). Non-linear least squares optimization of parameters use the Levenberg-Marquardt method (Bevington and Robinson, 2003). The

parameter uncertainties are estimated using bootstrap statistics (Efron and Tibshirani, 1994).

I explored different fitting approaches applied to the stacked spectra, including (a) varying all fitting parameters during least-squares minimization, or (b) fixing line centers to those Doppler corrected frequencies predicted by Rydberg's formula (Equation 1.1), or (c) fixing line widths to those expected by spectral line broadening theory, or (d) fixing line intensities to those also expected from spectral line broadening theory. For the $\Delta n = 1$ to $\Delta n = 5$ bandpasses, all three cases gave self-consistent results, within the limits of statistical significance. However, this was not the case for the $\Delta n = 6$ and $\Delta n = 7$ bandpasses, including combinations of (b), (c) and (d). On this basis, I rule out the detection of H $\Delta n = 6$ and $\Delta n = 7$ RRLs.

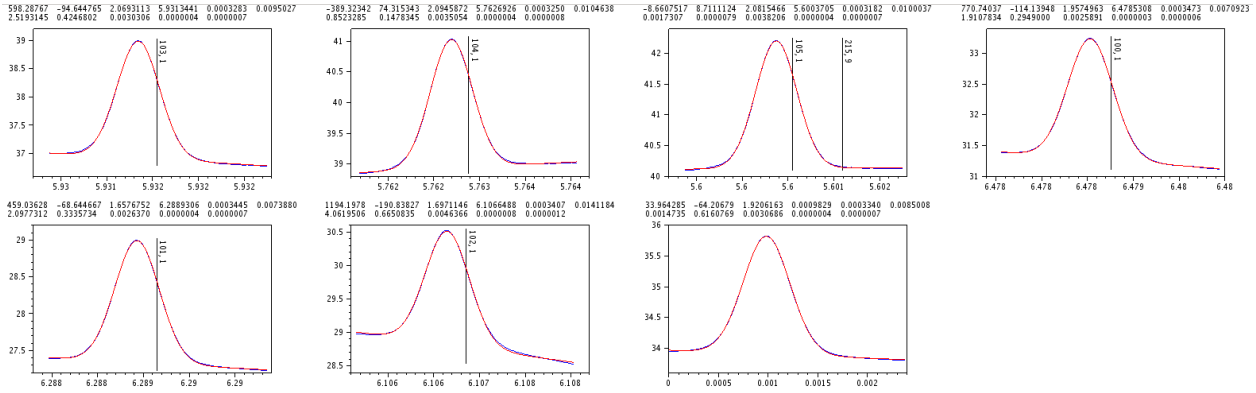

**Figure 3.8:** H $(n, \Delta n = 1)$ RRL bandpasses and stacked result (blue lines). The x-axes are frequency in GHz and y-axes are flux density, Jy. Vertical lines are predicted line-center frequencies from Rydberg's formula for hydrogen. Stacked result appears without a vertical line. Each two rows of numbers above each plot lists the best-fit linear plus Guassian profile (red-line) parameters: $a + bx + c \exp\left[-\left(\frac{x-d}{f}\right)^2\right]$. *Upper* row lists these five parameters, with the last value being the standard deviation of the difference between the data and fit. *Lower* row lists the parameter's one standard deviation uncertainties. Helium RRLs are just outside the high frequency end of each bandpass, so they do not appear here.

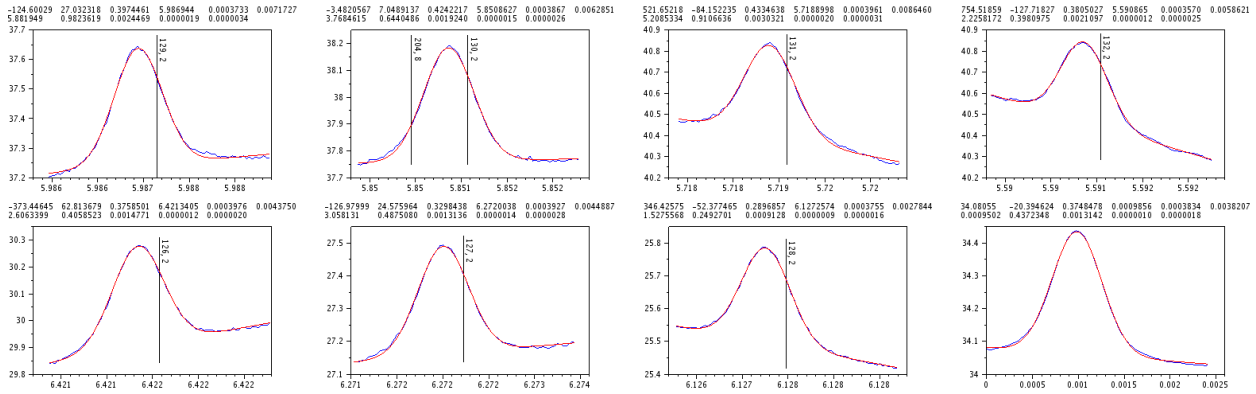

**Figure 3.9:** As in Figure 3.8: H $(n, \Delta n = 2)$ RRL bandpasses.

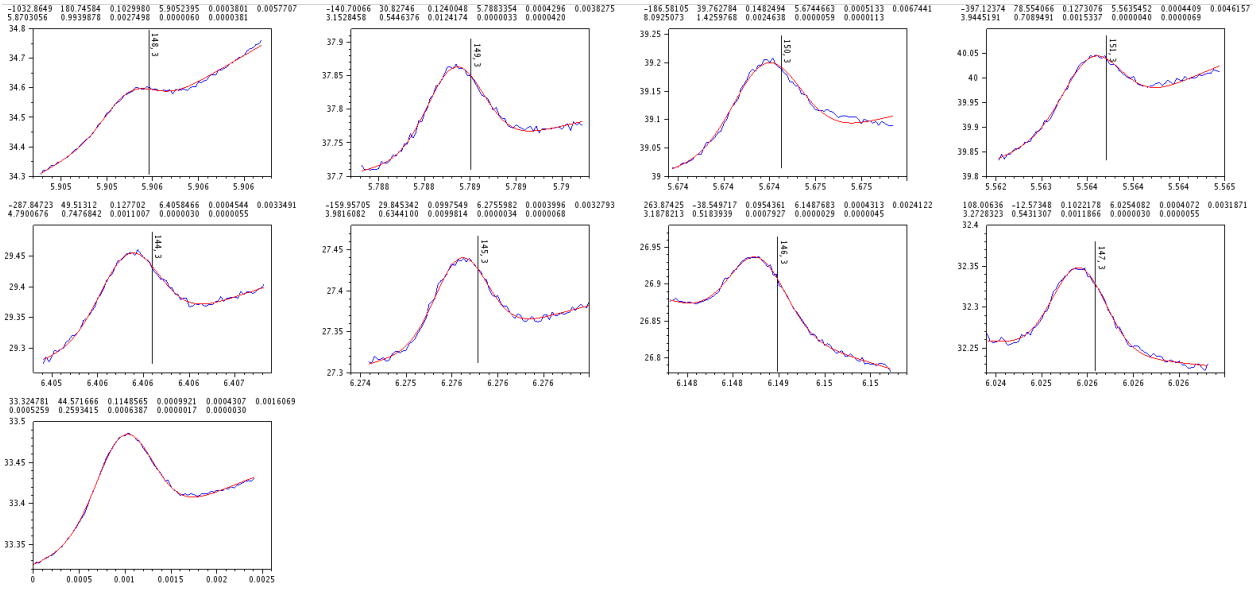

**Figure 3.10:** As in Figure 3.8: H$(n, \Delta n = 3)$ RRL bandpasses.

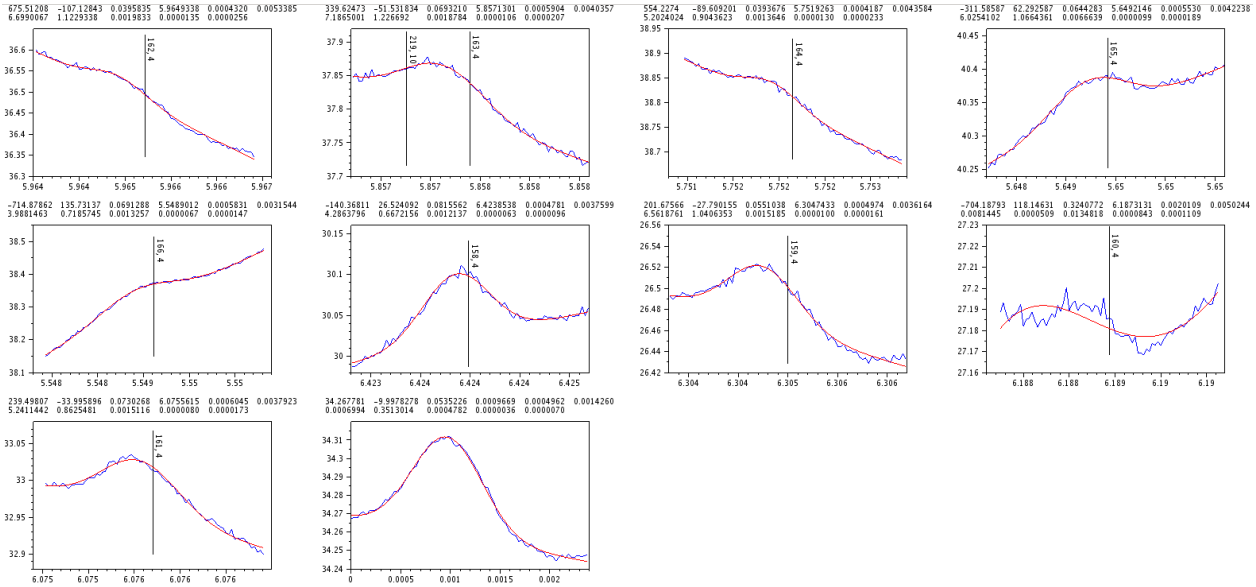

**Figure 3.11:** As in Figure 3.8: H$(n, \Delta n = 4)$ RRL bandpasses.

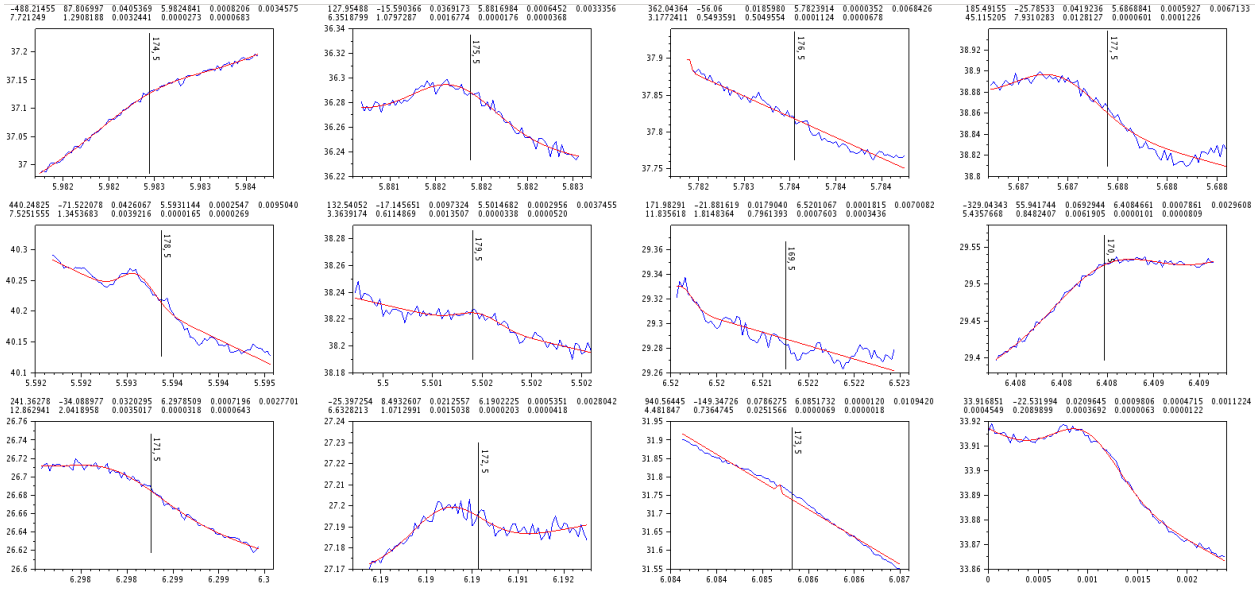

**Figure 3.12:** As in Figure 3.8: H$(n, \Delta n = 5)$ RRL bandpasses.

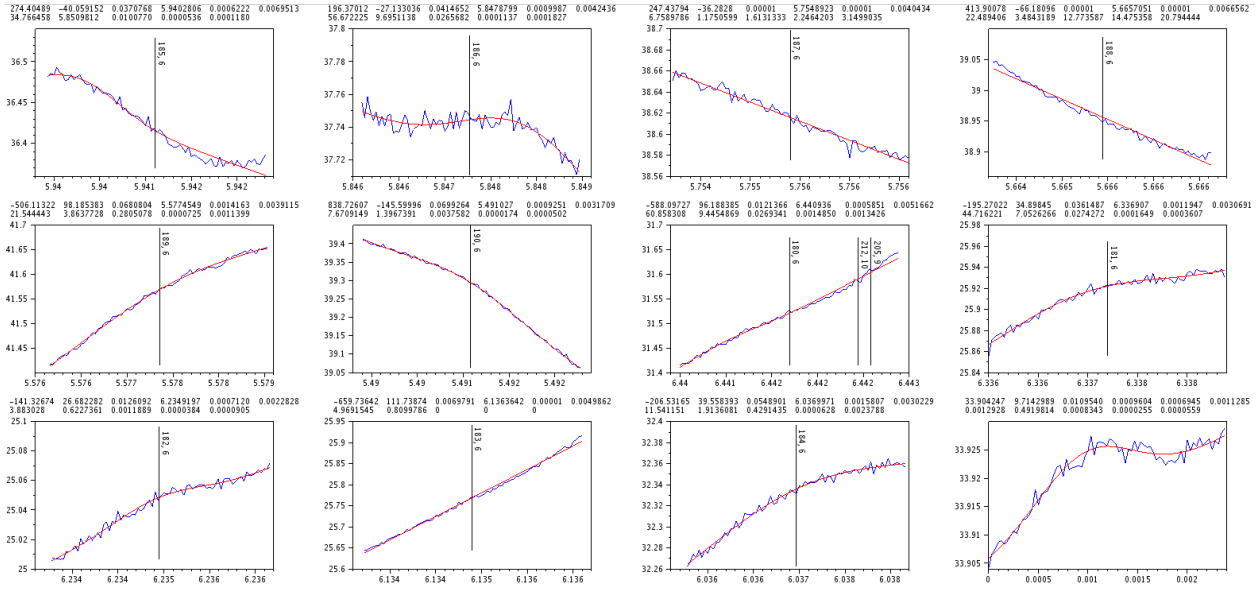

**Figure 3.13:** As in Figure 3.8: H$(n, \Delta n = 6)$ RRL bandpasses.

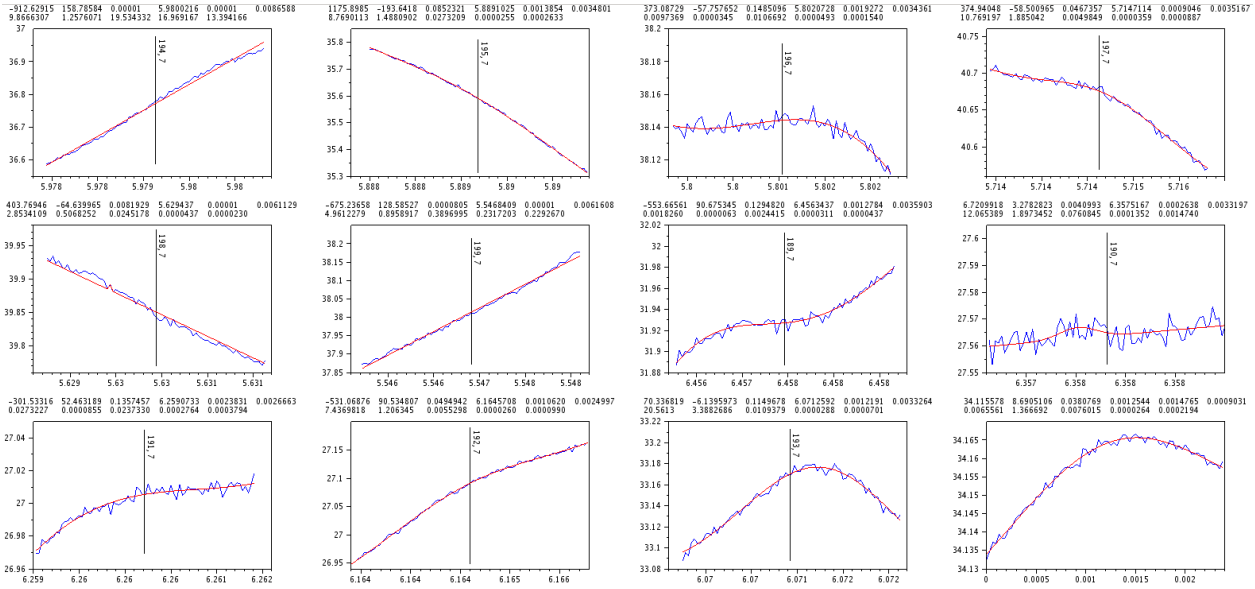

**Figure 3.14:** As in Figure 3.8: H$(n, \Delta n = 7)$ RRL bandpasses.

## 3.5 Measured spectral line intensities

At fixed frequency, integrated line intensities decrease with increasing $\Delta n$ as a power law,

$$I_{\Delta n} \propto \Delta n^{-k}, \tag{3.3}$$

where $k$ ranges approximately between 2 for pure Doppler broadening and 3 for pure Stark broadening; see Section 4.2, part 1. Using the intensity of the $\Delta n = 1$ line as the constant of proportionality, where Stark broadening is expected to be minimal, gives $I_{\Delta n} = I_1 \Delta n^{-k}$. A log-log plot of $I_{\Delta n}/I_1$ versus $\Delta n$ is shown in Figure 3.15. Also shown are power law fits to the data with fit results shown

in Table 3.2. We compare the option of a constant power $k$ with $k = a + b\Delta n$, which is more suitable for a transition from Doppler to Stark broadening. I find that at 6 GHz, the relative intensities of high-order RRLs from M42 are better modeled by a power law whose power depends linearly on $\Delta n$ — see Table 3.2, 3rd column.

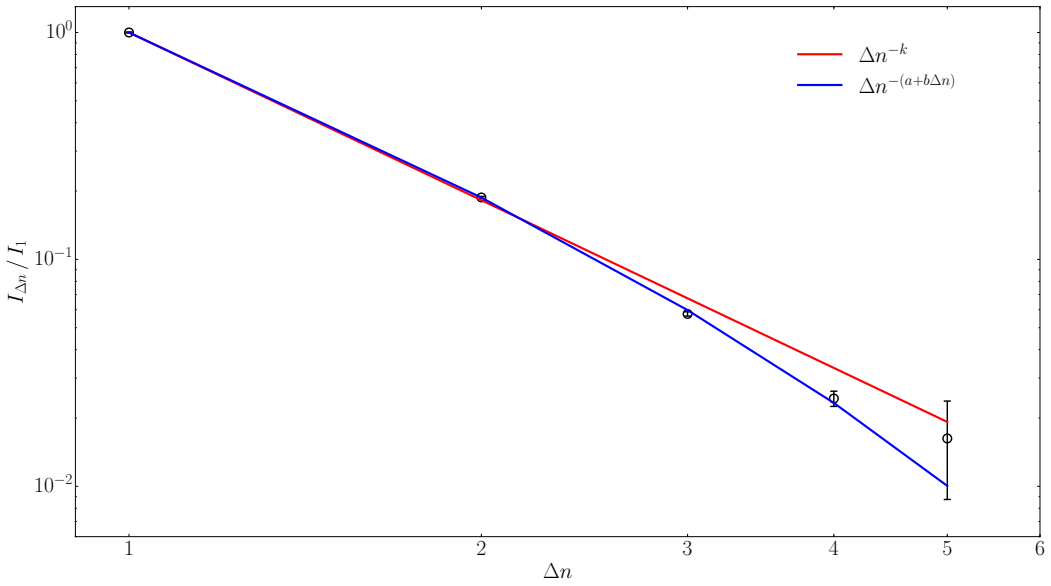


**Figure 3.15:** RRL intensity versus $\Delta n$ for M42. Error bars are $3\sigma$. Line intensity values are from Voigt fits shown in Figure 2 of Section 4.2. Red line is a weighted fit to the data using a power law with a constant power law index. Blue line is a weighted power law fit using an index that is a linear function of $\Delta n$. Fits include intensity data from $\Delta n = 1$ to $\Delta n = 4$ and are extrapolated to $\Delta n = 5$.

**Table 3.2:** Power-law index values for fits shown in Figure 3.15. Uncertainties are $3\sigma$.

| $\Delta n$ | $k$ | $k = a + b\Delta n$ |
|---|---|---|
| 1 | | $2.3 \pm 0.2$ |
| 2 | | $2.4 \pm 0.2$ |
| 3 | $2.5 \pm 0.2$ | $2.6 \pm 0.3$ |
| 4 | | $2.7 \pm 0.3$ |
| 5 | | $2.9 \pm 0.3$ |

# 4 Published papers

"Black hole spit me out; You better move over; Find your shades;
You'll be amazed; 'Cause I'm going Super Nova."

*Kate Stone (1962 — ....)*

In this chapter, I summarize two papers published during the dissertation, which are reproduced in Sections 4.1 and 4.2.

In the first paper (Alexander and Gulyaev, 2012), I demonstrate that the observed RRL narrowing first reported by Bell et al. (2000) is an artifact of their data processing. I accomplish this by creating a theoretical model of the multiple FS (frequency shifting) technique, originally developed by Bell (1997), which I then implemented as a computer simulation.[1] I co-created a theoretical model of the Orion nebula which includes mechanisms of spectral line broadening and non-equilibrium thermodynamics effects. This model was then used to numer-

[1] This technique copies a spectral line bandpass, shifts it in frequency by an offset, and adds it to the unshifted bandpass. This process is called an overlap. The output of this process is then fed back to itself multiple times. Six overlaps where used by Bell et al. (2000).

ically solve the radiative transfer problem to simulate RRLs. These simulated lines are then processed through the multiple FS model, the results of which are called "processed" lines. I then used Monte Carlo simulation to estimate how simulated noise influences the processed line widths and amplitudes.

From these models and simulations, I demonstrate that multiple FS does not preserve broadening when the original line width is greater than the FS-offset. In this case, I find the processed results manifest the narrowing reported by Bell et al. (2000), by reducing broad spectral wings characteristic of Stark broadened RRLs. I also find that the S/N of processed lines *reduces* weakly with the number of overlaps as a result of adding *dependent* samples. This means the S/N of processed lines as a function of $\Delta n$, at fixed frequency, decreases faster than for unprocessed lines, such that a given statistical insignificance level is reached more quickly.

Given this analysis, I argue Bell et al. (2000)'s $\Delta n > 11$ lines are artifacts of their technique. I now suggest in the second paper that these artifacts are present for their $\Delta n > 7$ lines. I conclude that their reported findings, upon re-examination of their novel data processing technique, do not indicate a need to revise Stark broadening theory.

In the second paper (Alexander and Gulyaev, 2016) I present original observations of high-order RRLs from the Orion nebula to test the theory of Stark

broadening in cosmic plasmas. I use a wide 1 GHz bandpass centered at 6 GHz to significantly improve the accuracy of measurements by stacking up to eleven RRLs of the same $\Delta n$. I find no evidence of spectral line narrowing, confirming the conclusion of my first paper. I show that all statistically significant data from my observations and four-sets of previous observations of high-order RRLs (Smirnov et al., 1984; Bell et al., 2011) are in agreement and demonstrate how Stark broadening theory is consistent with these observations. I find that Lockman and Brown (1975)'s H RRL model of the Orion nebula over a large range of radio frequencies and $\Delta n \leq 2$ requires the addition of small-scale density inhomogeneities (clumps) and turbulence to adequately predict my observed H RRLs for $\Delta n \leq 5$.

I demonstrate that the power law predicted by electron-impact broadening theory is consistent with the five-sets of high-order RRLs analyzed here. My data do not allow distinguishing between two approaches to the cut-off parameters (nearest neighbor versus Debye radius) when predicting line broadening from electron impacts. Specifically, these data do not allow an unambiguous choice between the theoretical results of Griem (1967); Gee et al. (1976) and Watson (2006); Peach (2015). This ambiguity arises from small differences in the radiative transfer nebula model parameters. It is currently impossible to independently determine turbulent velocities and other physical & geometric parameters of the Orion nebula with enough accuracy to choose between the

two predications of electron-impact broadening theory. This situation represents an ill-posed inverse problem that is currently unsolvable (Brown et al., 1978). However, I show that Peach (2015)'s model for electron-plus-proton impacts significantly deviates from the Lorentz-width trend in my data. Reassessing this model is incumbent on plasma theorists.

## 4.1 Alexander, J. & Gulyaev, S. 2012, *ApJ*, 745, 194

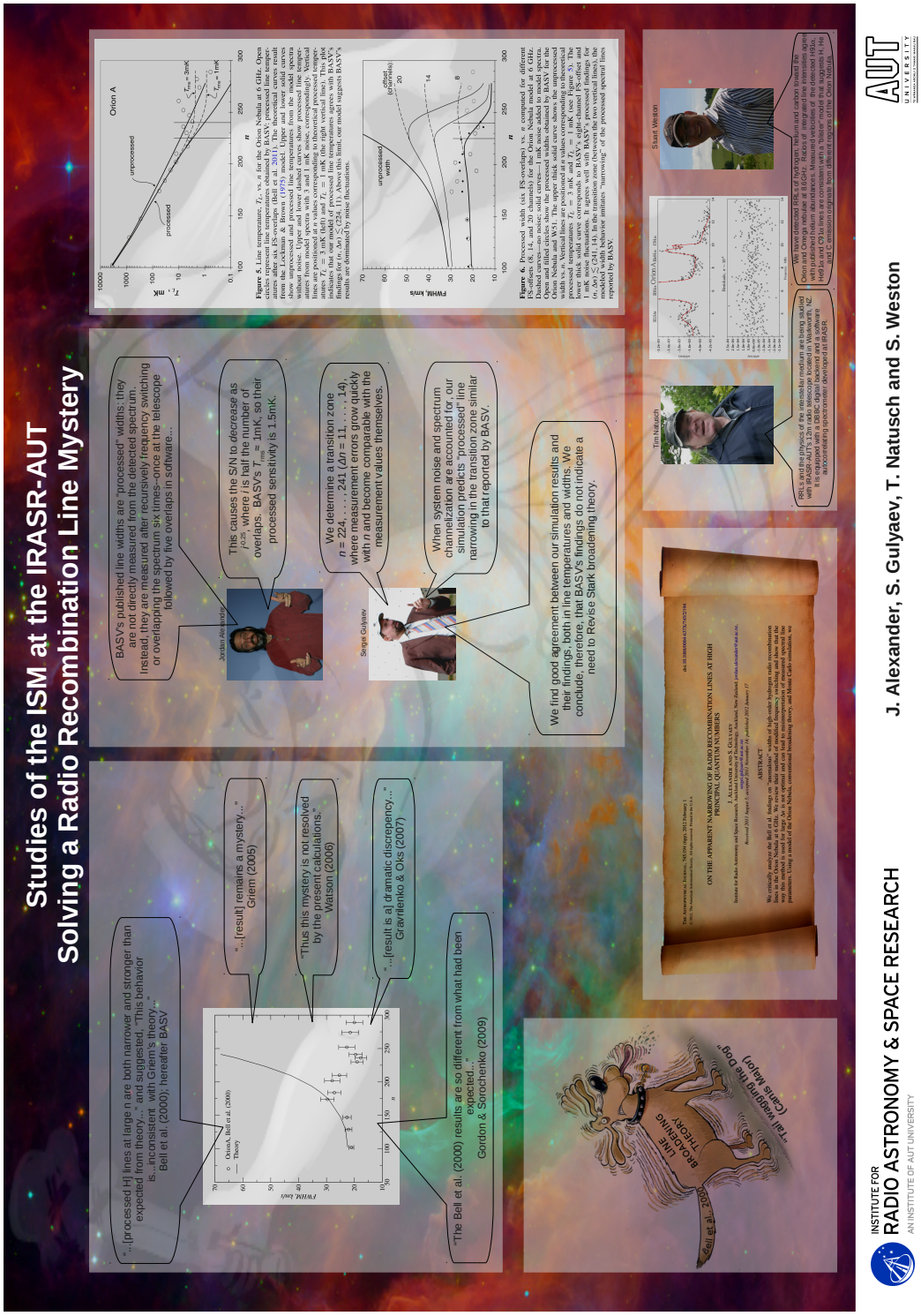


**Figure 4.1:** Poster, J. Alexander et al. 2012

The Astrophysical Journal, 745:194 (6pp), 2012 February 1 doi:10.1088/0004-637X/745/2/194


# ON THE APPARENT NARROWING OF RADIO RECOMBINATION LINES AT HIGH PRINCIPAL QUANTUM NUMBERS

J. Alexander and S. Gulyaev
Institute for Radio Astronomy and Space Research, Auckland University of Technology, Auckland, New Zealand; jordan.alexander@aut.ac.nz, sergei.gulyaev@aut.ac.nz
*Received 2011 August 5; accepted 2011 November 14; published 2012 January 17*

## ABSTRACT

We critically analyze the Bell et al. findings on "anomalous" widths of high-order hydrogen radio recombination lines in the Orion Nebula at 6 GHz. We review their method of modified frequency switching and show that the way this method is used for large $\Delta n$ is not optimal and can lead to misinterpretation of measured spectral line parameters. Using a model of the Orion Nebula, conventional broadening theory, and Monte Carlo simulation, we determine a transition zone $n = 224, \ldots, 241$ ($\Delta n = 11, \ldots, 14$), where measurement errors grow quickly with $n$ and become comparable with the measurement values themselves. When system noise and spectrum channelization are accounted for, our simulation predicts "processed" line narrowing in the transition zone similar to that reported by Bell et al. We find good agreement between our simulation results and their findings, both in line temperatures and widths. We conclude, therefore, that Bell et al.'s findings do not indicate a need to revise Stark broadening theory.

*Key words:* H II regions – line: profiles – methods: data analysis – methods: statistical – radio lines: ISM – techniques: spectroscopic

## 1. INTRODUCTION

In the 1990s, Morley Bell and coauthors developed a technique for measuring weak spectral lines by reducing broad baseline variations (Bell 1997). This technique was referred to as "modified frequency switching" and was used to detect weak atomic and molecular/maser lines in spectra of gaseous nebulae, circumstellar envelopes, and star formation regions (see, e.g., Bell & Feldman 1991; Bell et al. 1992, 1993).

Bell and coauthors used this technique to measure radio recombination line (RRL) widths and temperatures (Bell et al. 2000, hereafter BASV). At 6 GHz, they found that the "...[processed H] *lines at large n are both narrower and stronger than expected from theory...*" and suggested, "*This behavior is... inconsistent with Griem's theory...*." This publication, with its subtitle: "Confrontation with theory at high principal quantum numbers" induced a wave of publications where BASV's finding was called an "anomaly," "puzzle," and even "mystery." For example, Oks (2004) paper is titled "On the puzzle of the observed narrowing of radio recombination lines," Griem (2005) concludes his paper by writing that the result "...remains a mystery...," Gavrilenko & Oks (2007) calls the result a "dramatic discrepancy," and Watson (2006) concludes his abstract with "Thus this mystery is not resolved by the present calculations."

While some authors have sought an explanation of these findings in the revision of Stark broadening theory (e.g., Oks 2004; Watson 2006), some remain skeptical about the modified frequency switching technique or suggest that it requires verification. For example, von Procházka et al. (2010) writes "...it is easy to distort the RRL line shape using data reduction techniques (Bell et al. 2000)." Griem (2005) referred to private communication with Bell stressing that "...measurement errors related to large reduction factors from unprocessed to processed Voigt profile widths can probably not be excluded (M. B. Bell 2004, private communication)." In their book, Gordon & Sorochenko (2009) concluded: "The Bell et al. (2000) results are so different from what had been expected, and the observing technique is so new, that we suggest waiting for an independent confirmation of the observations before accepting a fault in the present theory of RRL Stark broadening."

BASV's findings are based on frequency switched or "processed" observational data, which were recently presented in Bell et al. (2011) and re-interpreted in Bell (2011). Their findings result from recursive frequency switching, in software, of observational data that were initially recorded at the telescope using hardware frequency switching.

In this paper, we investigate the frequency switching technique and demonstrate that, if applied correctly, it has a number of advantages. Frequency switching removes many gain variations and does not require subjective estimates of the zero level of a spectrum. Though the technique helped BASV to detect RRLs with $\Delta n$ greater than $\Delta n = 6$ (Smirnov et al. 1984), the way the method was used was not optimal and, as such, cannot be used to test the theory of spectral line broadening. We present simulations based on the Lockman & Brown (1975) model of the Orion Nebula and conventional theory of spectral line broadening. We apply observational specifications from BASV and Bell et al. (2011), including frequency range, channel width, frequency switching offset, number of frequency switching overlaps, and noise temperature rms. Results of our simulation demonstrate good agreement with BASV's findings, both in line width and temperature. The computed "processed" widths exhibit narrowing similar to that reported in BASV. We show that BASV's spectral line "narrowing" is the result of the way the observational data were processed and that BASV's findings do not contradict the existing Stark broadening theory.

## 2. SOFTWARE FREQUENCY SWITCHING

In this section, we introduce the data reduction technique used by BASV to systematically acquire information about weak spectral features in the presence of baseline fluctuations. Bell (1997) established and named this technique SOFMOR ("small-offset frequency switching multiple overlap reduction"). This technique was then called "modified frequency

switching" (MFS) in BASV. SOFMOR and MFS are frequency switching techniques that use a frequency offset fixed in the receiver hardware (see, e.g., Robinson 1964), followed by recursive frequency switching in software. Here, we refer to this technique (whether conducted in hardware or software) as FS (frequency switching).

In FS, the original spectrum is subtracted from a copy which is shifted by a number of channels (an offset). Mathematically, it can be related to a finite difference iteration.

If the offset is $h$, then the notation

$$f_p = f(x + p\,h) \tag{1}$$

can be used. Formulae for the results of $m$ FS iterations ($m$ finite differences) are then

$$\begin{aligned} f^{(1)} &= f_1 - f_0 \\ f^{(2)} &= f_2 - 2f_1 + f_0 \\ f^{(3)} &= f_3 - 3f_2 + 3f_1 - f_0 \\ f^{(4)} &= f_4 - 4f_3 + 6f_2 - 4f_1 + f_0 \end{aligned}$$

and so on (see, e.g., Beyer 1987, p. 449; Zwillinger 2002, p. 705), therefore

$$f^{(m)} = \sum_{k=0}^{m} f_k \binom{m}{k} (-1)^{m+k}. \tag{2}$$

When $f(x)$ is given with uncertainty $\pm\sigma_0$, where $\sigma_0$ is standard deviation, the resulting uncertainty in $f^{(m)}$ can be derived from the error propagation rule (see, e.g., Taylor 1997, p. 75) as

$$\sigma_m = \sigma_0 \sqrt{\sum_{k=0}^{m} \left(\frac{\partial f^{(m)}}{\partial f_k}\right)^2} = \sigma_0 \sqrt{\sum_{k=0}^{m} \binom{m}{k}^2} = \sigma_0 \sqrt{\binom{2m}{m}}. \tag{3}$$

Given that an FS spectrum overlaps with itself, the case of *dependent* samples must be applied (see below).

If $f(x)$ is a single channel feature (digital analog of $\delta$-function), that is

$$f(x) = \delta(x_0) = \begin{cases} 1, & x = x_0 \\ 0, & \text{otherwise}, \end{cases}$$

following Equation (2), $m$ FS-overlaps generate a series of equidistant peaks with amplitudes $\binom{m}{k}(-1)^{m+k}$. This is illustrated in the following Pascal's triangle for six consecutive overlaps or three cycles:

| overlap, m | | | | | | | cycle, $i$ |
|---|---|---|---|---|---|---|---|
| 0 | | | 1 | | | | 0 |
| 1 | | | −1 | 1 | | | |
| 2 | | 1 | −2 | 1 | | | 1 |
| 3 | | −1 | 3 | −3 | 1 | | |
| 4 | 1 | −4 | 6 | −4 | 1 | | 2 |
| 5 | −1 | 5 | −10 | 10 | −5 | 1 | |
| 6 | 1 | −6 | 15 | −20 | 15 | −6 | 1 3 |

Each cycle of two overlaps results in a symmetric pattern with a prominent central feature. The amplitude of the central feature after $i$ FS-cycles is the central binomial coefficient:

$$|A_i| = \binom{2i}{i} = 2,\ 6,\ 20,\ \ldots \qquad (i = 1,\ 2,\ 3, \ldots). \tag{4}$$

According to Equation (3), the standard deviation after $i$ FS-cycles

$$\sigma_i = \sqrt{\binom{4i}{2i}} = \sqrt{6},\ \sqrt{70},\ \sqrt{924}, \ldots \quad (i = 1,\ 2,\ 3,\ 4, \ldots), \tag{5}$$

resulting in a signal-to-noise ratio (S/N) of

$$\mathrm{S/N}_i = \frac{\binom{2i}{i}}{\sqrt{\binom{4i}{2i}}} = 0.82,\ \ 0.72,\ \ 0.66, \ldots \quad (i = 1,\ 2,\ 3, \ldots). \tag{6}$$

Using Stirling's formula (see, e.g., Abramowitz & Stegun 1965) we obtain

$$\mathrm{S/N}_i \approx \left(\frac{2}{\pi i}\right)^{1/4} = 0.89\, i^{-1/4}. \tag{7}$$

Therefore, BASV's S/N tends to *decrease* with the number of FS-cycles, $i$, as $i^{-1/4}$.

When *independent* samples are superimposed, the standard deviation is scaled as $\sigma_i = 2,\ 4,\ 8, \ldots$, which results in the growth of the S/N: $\mathrm{S/N}_i = \binom{2i}{i}/2^i = 1,\ 1.5,\ 2.5,\ \ldots$ ($i = 1,\ 2,\ 3,\ \ldots$). This common approach is not applicable to the FS technique used in BASV. Instead, they overlap the once recorded spectrum with itself and therefore the case of dependent samples must be used, as derived in Equations (5)–(7).

Though the first overlap in BASV occurs in hardware, where two independent samples are mixed, the S/N remains unchanged because the first overlap of two samples produces a $\sqrt{2}$ increase in the resulting standard deviation regardless of whether the two samples are dependent (software FS) or independent (hardware FS).

Figure 1 shows a Gaussian feature characterized by its full width at half-maximum (FWHM), $w$, and its transformation after 2, 4, and 6 FS-overlaps are applied to the initial feature. The frequency offset or FS-offset, $h$, is chosen to be much greater than the width, $h \gg w$. Additional features appear offset from the central feature, whose offsets are multiples of $h$. All the features are shifted relative to the position of the original feature, $x_0$. After $i$ FS-cycles, the central feature is located at $x = x_0 - i\,h$. These shifts are removed in Figures 1 and 2, such that all features are centered vertically. Additionally, all features are normalized and inverted (where necessary) to compare their shapes and widths.

If $h \gg w$, the additional features (referred to as "reference images" in Bell 1997) can be removed by adding or subtracting scaled versions of the central feature to them—a process referred to as "cleaning" in Bell (1997). For example, after two FS-overlaps, the additional features shown in Figure 1 can be removed by adding the central feature divided by 2. Dividing this result by −2 recovers the original feature exactly. After four overlaps, shown in Figure 1, the additional features are removed by adding $-1/6$ and $4/6$ of the central feature to them. Dividing the central feature by 6 recovers the original feature exactly.

This normalization procedure keeps the central feature's amplitude unchanged regardless of the number of FS-cycles, $i$. However, according to Equation (7), the noise level grows as $i^{1/4}$.

NRAO's 140 ft telescope was used by BASV to observe the Orion Nebula at 6 GHz. Based on the 140 ft data archive of the

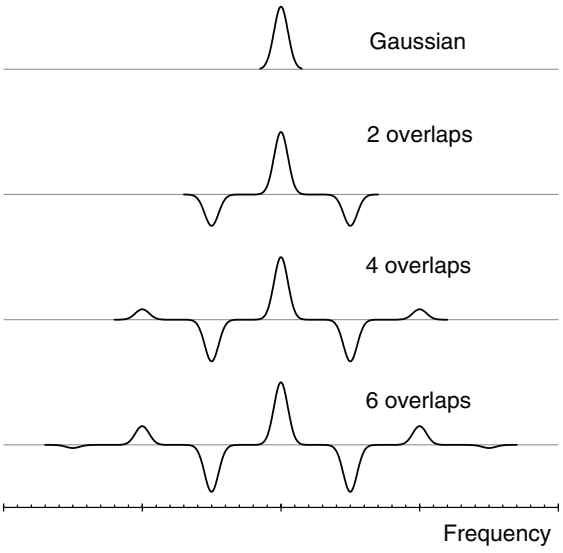


**Figure 1.** Transformation of a Gaussian shape after 2, 4, and 6 FS-overlaps. The initial width, $w$, is much less than the FS offset, $h$; $w/h = 0.2$. This plot is a graphical depiction of Pascal's triangle in Section 2. To compare the shapes and widths, we invert (where necessary) the resulting spectra and normalize the peak intensity of the central feature to the intensity of the initial Gaussian.

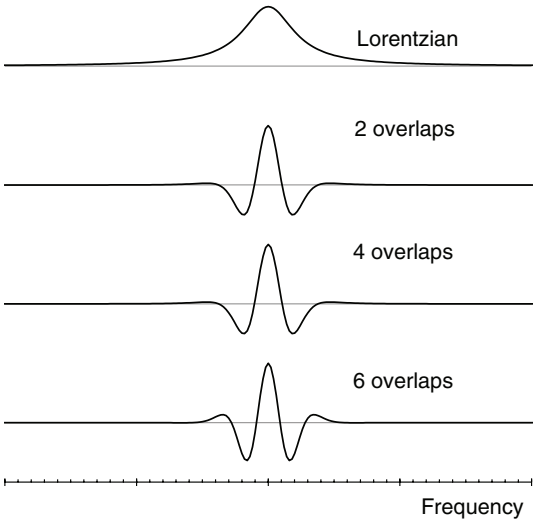


**Figure 2.** Transformation of a Lorentzian shape after 2, 4, and 6 FS-overlaps. The initial width, $w$, is greater than the offset, $h$. The ratio $w/h = 4$ is used, which corresponds to BASV's $\Delta n = 20$ case. To compare the shapes and widths, we invert (where necessary) the resulting spectrum and normalize the peak intensity of the central feature to the intensity of the initial Lorentzian.

1992 April observation (integration time of ~48 hours, system temperature of ~120 K, and channel width of ~78 kHz), a noise temperature $T_{\rm rms} \approx 1$ mK could be achieved. Given that BASV used six overlaps (one hardware and five software FS-overlaps) or three cycles, Equation (7) implies an "frequency-switched" temperature rms of $T_{\rm rms} \approx 1.5$ mK.

Figure 2 illustrates the case when the FS-offset is less than the original line width, $h < w$, specifically $h = w/4$. This figure shows the transformation of a Lorentzian feature after 2, 4, and 6 FS-overlaps. To compare the shapes and widths, we normalize the peak intensity of the central feature to the intensity of the initial feature. Figure 2 shows that the central feature of the processed line is much narrower than the width of the original Lorentzian. Given that FS processing reduces line widths and amplitudes when $h < w$, BASV refer to them as "processed" widths and amplitudes.

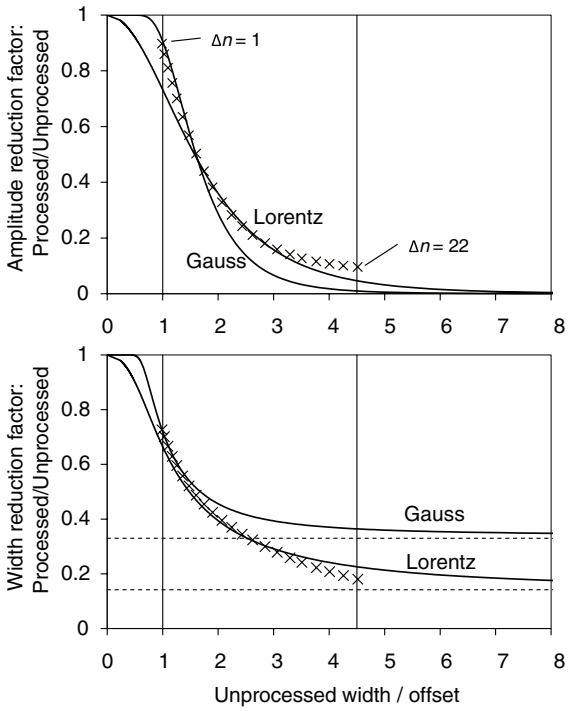


**Figure 3.** Reduction factors (processed over unprocessed) for the peak line temperature (top plot) and the line width (bottom plot) as a function of the normalized unprocessed width, $w/h$. Both plots are calculated for six FS-overlaps. Vertical lines show minimal and maximal values of $w/h$ for BASV's observations: $1 \lesssim w/h \lesssim 4.5$. Crosses show reduction factors predicted by the three-component Orion Nebula model of Lockman & Brown (1975). Horizontal dashed lines in the bottom plot are the asymptotes for Gaussian and Lorentzian curves as $w/h \to \infty$. These plots demonstrate that, for a fixed FS-offset $h$, significant reduction in spectral line intensity and width results from FS as the unprocessed line width increases due to Stark broadening.

The Voigt profile, which models the RRL shape, is a convolution of Gaussian and Lorentzian profiles, where the Gaussian represents the Doppler-broadened contribution and the Lorentzian represents the impact-broadened contribution (Gordon & Sorochenko 2009). Figure 3 shows how the amplitudes and widths of FS-processed Gaussian and Lorentzian profiles vary as a function of the normalized unprocessed width, $w/h$. These plots show amplitude and width reduction factors (processed to unprocessed ratio) calculated for six FS-overlaps. The vertical lines show the limits of BASV's experiment: $1 \lesssim w/h \lesssim 4.5$. Crosses are reduction factors predicted by the Lockman & Brown (1975) Orion Nebula model (see the next section). Horizontal dashed lines in the bottom plot are the asymptotes for Gaussian and Lorentzian cases as $w/h \to \infty$.

## 3. APPLICATION OF FS TO MODEL SPECTRA

The frequency switching technique used in BASV consists of two independent steps: (1) overlapping the spectrum and (2) "cleaning" the overlapped spectrum. Overlapping six times creates a set of "reference images" for each line feature in the spectrum. The result of overlapping (step 1) is illustrated in

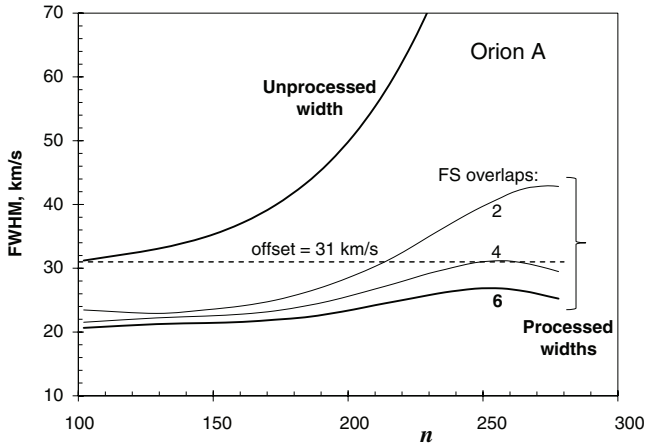


**Figure 4.** Processed width vs. $n$ for different numbers of FS-overlaps at 6 GHz. Simulation is conducted for the Orion Nebula model of Lockman & Brown (1975); no noise is taken into account. Dashed line shows BASV's FS-offset (eight channels = 31.2 km s$^{-1}$). The upper (thick) curve shows the unprocessed width $w$ vs. $n$. The lower curve corresponds to the BASV's case of six FS-overlaps. This plot demonstrates that when $h < w$, the processed width is *increasingly* insensitive to the significantly changing unprocessed width as the number of overlaps increase. This indicates that the FS technique in BASV's case is a poor probe of line broadening.

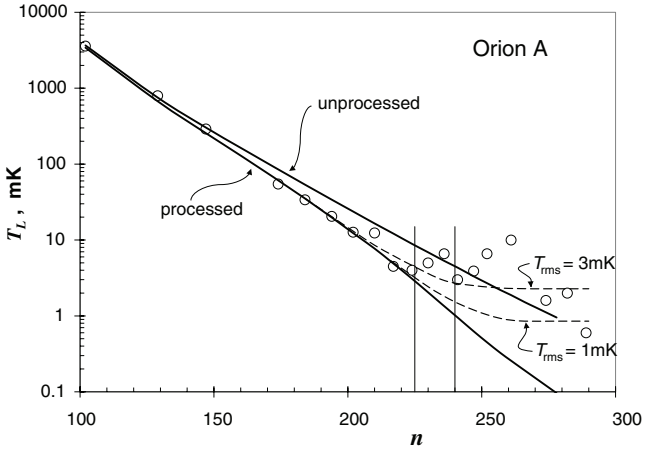


**Figure 5.** Line temperature, $T_L$, vs. $n$ for the Orion Nebula at 6 GHz. Open circles represent line temperatures obtained by BASV: processed line temperatures after six FS-overlaps (Bell et al. 2011). The theoretical curves result from the Lockman & Brown (1975) model. Upper and lower solid curves show unprocessed and processed line temperatures from the model spectra without noise. Upper and lower dashed curves show processed line temperatures from model spectra with 3 and 1 mK noise, correspondingly. Vertical lines are positioned at $n$ values corresponding to theoretical processed temperatures $T_L = 3$ mK (left) and $T_L = 1$ mK (the right vertical line). This plot indicates that our model of processed line temperatures agrees with BASV's findings for $(n, \Delta n) \lesssim (224, 11)$. Above this limit, our model suggests BASV's results are dominated by noise fluctuations.

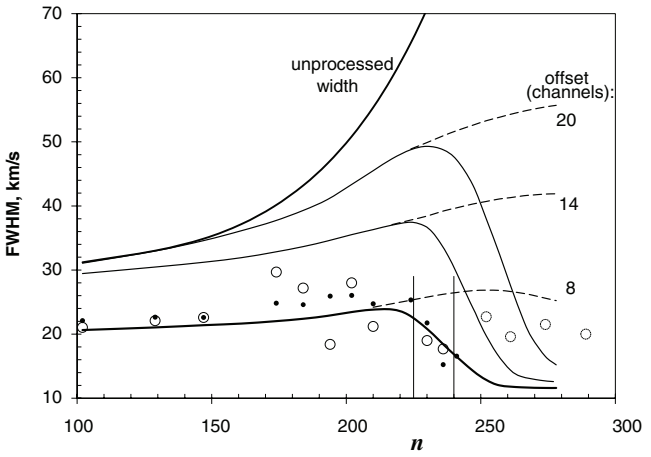


**Figure 6.** Processed width (six FS-overlaps) vs. $n$ computed for different FS-offsets (8, 14, and 20 channels) for the Orion Nebula model at 6 GHz. Dashed curves—no noise; solid curves—1 mK noise added to model spectra. Open and filled circles show the processed widths obtained by BASV for the Orion Nebula and W51. The upper thick solid curve shows the unprocessed width vs. $n$. Vertical lines are positioned at $n$ values corresponding to theoretical processed temperatures $T_L = 3$ mK and $T_L = 1$ mK (see Figure 5). The lower thick solid curve corresponds to BASV's eight-channel FS-offset and 1 mK noise fluctuations. It agrees well with BASV's processed findings for $(n, \Delta n) \lesssim (241, 14)$. In the transition zone (between the two vertical lines), the modeled width behavior imitates "narrowing" of the processed spectral lines reported by BASV.

Figures 1($h \gg w$) and 2 ($h < w$). When $h < w$ (BASV's case), overlapping reduces the line widths to below the FS-offset, $h$.

After overlapping, the reference images are removed. In Bell (1997) and BASV, this "cleaning" procedure was done manually, one line at a time, starting with the strongest line and working to the weakest. BASV's reported line widths after cleaning are in the range of 18–30 km s$^{-1}$, which is less than or about the Doppler width and less than the FS-offset (Figures 2 and 4 in BASV). The conclusion made in BASV about line "narrowing" is based on interpretation of these "processed" widths.

A multi-component non-LTE radiative transfer simulator was created to explore the effect of FS on model RRL spectra. For the Orion Nebula we use the three-component model of Lockman & Brown (1975), which simulates the beam size of the 140 ft radio telescope. The model consists of a compact (0.043 pc) dense ($N_e = 10^{4.5}$ cm$^{-3}$) symmetric core located behind two extended (0.56 and 2.50 pc) layers of gas of lower density ($N_e = 10^{3.5}$ and $10^{2.3}$ cm$^{-3}$). The corresponding temperatures are $T_e = 7500$ K (core), 10,000 K, and 12,500 K (outer layer). This model predicts continuum emission and H$n\alpha$ and H$n\beta$ spectra in agreement with observations between 1 and 90 GHz (Lockman & Brown 1975).

Figures 4–6 show the model results for processed line temperatures and processed widths versus principal quantum number, $n$, for the Orion Nebula model at 6 GHz. To avoid ambiguity associated with the cleaning procedure, we process each modeled spectral line separately. The processed line width is the FWHM of the central feature measured above the zero level (see Figure 2).

Figure 4 shows the processed widths (FWHM) for 2, 4, and 6 FS-overlaps (1, 2, and 3 cycles). Following BASV, we used six overlaps and an offset of 625 kHz = 31.2 km s$^{-1}$, which corresponds to eight spectral channels (channel width of 78.13 kHz = 3.9 km s$^{-1}$). Noise was not added to the model spectra when computing these curves. The dashed line shows BASV's FS-offset (eight channels = 31.2 km s$^{-1}$). After six FS-overlaps, the processed width (FWHM) remains at the level of $\sim$70%, ..., 85% of the offset, reaching a maximum at $n \simeq 260$, then drops down to 81% at higher $n$. This behavior reflects a growing contribution to the line shape from the nebula's low-density outer layer at very high $n$. The greater contribution of the outer low-density layer at high $n$ also explains the deviation of the reduction factors (crosses) in Figure 3 from the "Lorentzian" behavior.

Figure 5 shows the line temperature, $T_L$, versus $n$ for the Orion Nebula. Open circles are BASV's processed $T_L$. Solid curves show unprocessed (upper curve) and processed $T_L$ for

the model spectra without noise. Dashed curves show processed $T_L$ for model spectra with 1 and 3 mK noise added. These curves are obtained using the following Monte Carlo method. For each modeled spectral line feature, normally distributed noise is added, then FS-overlapped six times. $T_L$ and $w$ of this processed feature are then estimated by a Gaussian fit, as done by BASV. The least-squares-fitting algorithm searches for the best fit within a $\pm 2$ channel interval about the central line frequency. These steps were trialed 1000 times to determine the mean and standard deviation values of $T_L$ and $w$ for each processed spectral line feature. This method was carried out for the expected 1 mK noise rms and, additionally, a 3 mK noise rms. Two vertical lines in Figure 5 are positioned at $n$ values corresponding to the processed, noise-free model temperatures $T_L = 3$ mK (left line) and $T_L = 1$ mK (right line). Given BASV's $T_{\rm rms} \sim 1$ mK, the vertical lines represent the $3\sigma$ and $1\sigma$ limits. The corresponding limiting values of $n = 224$ ($\Delta n = 11$) and $n = 241$ ($\Delta n = 14$) are also indicated by vertical lines in Figure 6.

Processed widths versus $n$ for 8, 14, and 20 channel offsets are shown in Figure 6 for the 6 GHz Orion Nebula model. For comparison, the thick upper solid curve is unprocessed noise-free model widths. Dashed curves in Figure 6 correspond to processed noise-free model widths, while solid curves are the corresponding processed widths resulting from the Monte Carlo method described above using 1 mK noise added to the model spectra. Open and filled circles in Figure 6 are BASV's processed widths for the Orion Nebula and W51 (see also Bell et al. 2011). The left and right vertical lines show the $3\sigma$ and $1\sigma$ confidence limits from Figure 5.

## 4. DISCUSSION

The multiple frequency switching technique reduces amplitudes of broad baseline variations and therefore can be used to systematically "flatten" baselines (Bell & Feldman 1991; Bell et al. 1992, 1993). Compared to standard spline/polynomial baseline fitting, which allows for subjective decisions, the FS technique reduces baseline variations objectively. For spectral features that are much wider than the offset, $h$, FS can be likened to differentiation, which acts as a high-pass filter in the frequency domain (see, e.g., Hamming 1998; Owen 1995). In this case, six overlaps approximates the sixth derivative with respect to frequency, which makes FS an efficient high-pass filter. This not only reduces broad variations in the spectrum, but in BASV's case (six overlaps, $h < w$), it also reduces broad spectral line wings larger than the FS-offset, which manifests as line narrowing (see, e.g., Figure 2).

We use the Lockman & Brown (1975) model of the Orion Nebula and simulate the conditions of BASV's observations at 6 GHz: telescope beam size, frequency range, channel width, offset, number of overlaps, and noise temperature. When modeling, we can avoid some difficulties that BASV faced when they processed the real spectrum. The real spectrum is abundant with spectral lines; after overlapping six times, the resulting spectrum is crowded with lines and reference lines. This situation is further complicated when significant noise fluctuations are present, which is BASV's case when $\Delta n > 11$, so cleaning becomes a non-trivial and subjective procedure. In our case cleaning is trivial as we can model and clean each RRL individually, with and without noise.

For all H$n\Delta n$ lines studied in BASV, the unprocessed width (i.e., before FS) is greater than the FS-offset used. We show that the processed width weakly depends on $n$ and $\Delta n$ (see Figure 4, the six FS-overlaps case). In fact, it remains about $0.8\,h$ for a wide range of $n$ and $\Delta n$. This property of the FS technique makes it insensitive to changes in RRL widths when $h < w$. (It is for this reason that we justify the inclusion of BASV's processed widths for W51 at 6 GHz in Figure 6.) The FS technique can be used to systematically eliminate broad baseline variations to detect weak lines, however, in BASV's case (six overlaps, $h < w$), this technique is not well suited to study RRL broadening. If one's purpose is to test the theory of spectral line broadening, the choice of the offset made in BASV ($h < w$) is not optimal.

It is shown in the previous sections that FS reduces the S/N (see Equation (6)) and spectral line amplitudes (Figure 3). As a result of amplitude reduction, the processed line temperature drops rapidly to the noise temperature $T_{\rm rms} = 1$ mK as $n$ and $\Delta n$ grow (the lower solid curve in Figure 5). The model processed line amplitude reaches 3 mK ($3\sigma$ level) at $n = 224$ ($\Delta n = 11$) and 1 mK ($1\sigma$ level) at $n = 241$ ($\Delta n = 14$). The interval between $n = 224$ and 241 (between $\Delta n = 11$ and 14) is a transition zone between observable spectral lines and noise. Figure 6 shows that the processed width behavior in the transition zone imitates "narrowing" of the processed spectral lines observed by BASV in spectra of the Orion Nebula and W51 at 6 GHz. This "narrowing" is the result of "forcing" a program to fit Gaussians to features dominated by noise fluctuations—the procedure used by BASV.

Spectra presented in Bell (1997), BASV and Bell et al. (2011) result from the overlapping and cleaning steps explained in Section 3. Though BASV applied overlapping to the entire spectrum, cleaning was applied selectively to features located near the expected spectral line frequencies, even if the processed line temperatures were below $3\sigma$. This subjective and selective approach could create "spectral lines" from random fluctuations at the $\lesssim 3\,\sigma$ level, which are abundant in the spectrum.

For $\Delta n \geqslant 14$, the width errors predicted by our Monte Carlo simulation are comparable to the widths themselves. Therefore, BASV's data points for $\Delta n \geqslant 14$ shown in Figures 5 and 6 are likely to be misinterpreted noise features.

In conclusion, FS is a useful technique for detecting and measuring weak spectral features, if required corrections are minimal, that is if the FS offset is greater than the line width: $h \gtrsim w$. Based on our simulation results, we argue that BASV's $T_{\rm rms} \approx 1$ mK observations of hydrogen RRLs from the Orion Nebula at 6 GHz are limited to $\Delta n < 14$. Within this limit, we find good agreement between their results and a Monte Carlo simulation based on conventional Stark broadening theory and, therefore, we argue that BASV's findings do not necessitate a revision of RRL Stark broadening theory. We suggest that further tests of line broadening theory above this limit will require observations with sub-mK sensitivity and improved baseline stability.

We thank Morley Bell for helpful communications when learning about FS. We thank Johannes Buchner for enlightening discussions about FS and various software tools. We thank Ron Maddalena for assistance with NRAO's 140 ft data archive. Finally, we thank Miller Goss for many encouraging and valuable discussions.

## REFERENCES

Abramowitz, M., & Stegun, I. A. 1965, An Introduction to Error Analysis: The Study of Uncertainties in Physical Experiment (2nd ed.; New York: Dover)
Bell, M. 2011, Ap&SS, 335, 451

Bell, M. B. 1997, PASP, 109, 609
Bell, M. B., Avery, L. W., MacLeod, J. M., & Vallée, J. P. 2011, Ap&SS, 333, 377
Bell, M. B., Avery, L. W., Seaquist, E. R., & Vallée, J. P. 2000, PASP, 112, 1236
Bell, M. B., Avery, L. W., & Watson, J. K. G. 1993, ApJS, 86, 211
Bell, M. B., & Feldman, P. A. 1991, ApJ, 367, L33
Bell, M. B., Feldman, P. A., & Avery, L. W. 1992, ApJ, 396, 643
Beyer, W. H. 1987, CRC Standard Mathematical Tables (28th ed.; Boca Raton, FL: CRC Press)
Gavrilenko, V. P., & Oks, E. 2007, Phys. Scr., 76, 43
Gordon, M. A., & Sorochenko, R. L. 2009, Radio Recombination Lines: Their Physics and Astronomical Applications (New York: Springer)
Griem, H. R. 2005, ApJ, 620, L133
Hamming, R. W. 1998, Digital Filters (3rd ed.; Mineola, NY: Courier Dover Publications)
Lockman, F. J., & Brown, R. L. 1975, ApJ, 201, 134
Oks, E. 2004, ApJ, 609, L25
Owen, A. J. 1995, Uses of Derivative Spectroscopy, Technical Report 5963-3940E, Agilent Technologies
Robinson, B. J. 1964, ARA&A, 2, 401
Smirnov, G. T., Sorochenko, R. L., & Pankonin, V. 1984, A&A, 135, 116
Taylor, J. 1997, An Introduction to Error Analysis: The Study of Uncertainties in Physical Experiment (2nd ed.; Sausalito, CA: Univ. Science Books)
von Procházka, A. A., Remijan, A. J., Balser, D. S., et al. 2010, PASP, 122, 354
Watson, J. K. G. 2006, J. Phys. B: At. Mol. Opt. Phys., 39, 1889
Zwillinger, D. E. 2002, Difference Equations and Numerical Differentiation, 3.9 and 8.3.2 in CRC Standard Mathematical Tables and Formulae (Boca Raton, FL: CRC Press)

## Errata

1. In Equation 5, the left-hand-side should be $\frac{\sigma_i}{\sigma_0}$, instead of $\sigma_i$.

2. The first citation of the REFERENCES section should read:

   "Abramowitz, M. and Stegun, I. A. 1965. Handbook of mathematical functions with formulas, graphs, and mathematical tables. Dover, New York, corrected edition"

3. I discovered an earlier (the first?) published reference to the apparent narrowing of cosmic RRLs: Bell et al. (1991).

## 4.2 Alexander, J. & Gulyaev, S. 2016, *ApJ*, 828, 40


**Figure 4.2:** "Dennis Brown", Ruchell Alexander 1996

The Astrophysical Journal, 828:40 (7pp), 2016 September 1 doi:10.3847/0004-637X/828/1/40


# STARK BROADENING OF HIGH-ORDER RADIO RECOMBINATION LINES TOWARD THE ORION NEBULA

J. Alexander and S. Gulyaev
Institute for Radio Astronomy and Space Research, Auckland University of Technology, Auckland, New Zealand; jordan.alexander@aut.ac.nz, sergei.gulyaev@aut.ac.nz
*Received 2016 May 5; revised 2016 June 20; accepted 2016 June 28; published 2016 August 26*

## ABSTRACT

We report the results of observations and analyses of 41 $\Delta n = 1, \ldots, 5$ hydrogen radio recombination lines from the Orion nebula (M42) at 5.5 to 6.5 GHz, with a spectral sensitivity (channel-to-channel standard deviation) of $\approx$2 mJy. Observations were conducted at the Australia Telescope Compact Array. A 1 GHz bandwidth allowed simultaneous detection of up to 11 spectral lines of equal $\Delta n$ that were stacked to enable accurate measurement of line widths. Collisional widths in the range of principal quantum numbers $n$ from 100 to 179 are found to be consistent with predictions of electron impact Stark broadening theory. An Orion nebula model with density inhomogeneities (clumps) and gradients of temperature and density is consistent with our data. We reanalyze the data of Smirnov et al. and Bell et al. and find excellent agreement between all statistically significant measurements and theory. Our findings confirm the absence of line narrowing for $n = 100...179$.

*Key words:* H II regions – ISM: atoms – methods: data analysis – radio lines: ISM – techniques: spectroscopic

## 1. INTRODUCTION

Rydberg atoms and Stark broadening of hydrogen and hydrogen-like spectral lines continue to attract the attention of atomic physicists and astrophysicists, given their use in quantum computer gates (Goldschmidt et al. 2015) and probing cosmic and laboratory plasmas, including thermonuclear reactor plasma (Lisitsa et al. 2012). Since the pioneering work of Griem (e.g., Griem 1960), theoretical approaches for computing spectral line widths have been refined (see e.g., Watson 2006; Peach 2015), and so have the ways of testing them in space and laboratory observations (see, e.g., Peach et al. 2009; Lisitsa et al. 2012). Radio recombination lines (RRLs) have been used for testing Stark broadening theory since the 1960s (Gordon & Sorochenko 2009). Initially, observations of RRLs stimulated significant improvement in the theory (Griem 1967; Minaeva et al. 1967). Observations generally confirmed the revised theory (Smirnov et al. 1984) with the exception of one observational result of Bell et al. (2000), later explained by Alexander & Gulyaev (2012).

Galactic H II regions are suitable objects for testing spectral line broadening theory. However, their complex geometry with gradients of density and temperature (Lockman & Brown 1975; Wilson et al. 2011), small-scale inhomogeneities (Gulyaev & Sorochenko 1974; Matsakis et al. 1982), and turbulence (Sorochenko & Berulis 1969; Wink et al. 1983; Castaneda 1988; Wilson et al. 2012) complicate the interpretation of observational data. Thus, careful modeling is needed when interpreting observations over a wide range of frequencies. Such modeling requires solving the non-LTE radiation transfer problem for a nebula model for each spectral line that accounts for beamwidth dependence of a radio telescope on principal quantum number $n$ and the frequency dependence of optical depth $\tau(\nu)$. Extraction of Stark broadening is therefore ambiguous, given these free parameters.

High-order RRLs offer the best solution for minimizing these difficulties. In a narrow range of frequencies, a number of RRLs with different $n$ and $\Delta n$ can be observed because $n \propto \Delta n^{1/3}$ when $\nu \approx$ constant, therefore, e.g., H100$\alpha$ ($\Delta n = 1$) and H200$\theta$ ($\Delta n = 8$) lines have close frequencies. A constant frequency means an unchanging telescope beamwidth and continuum optical depth, allowing direct comparison of RRLs with different $n$ and a simple extraction of the dependence of the Stark widths on $n$ without complex modeling, particularly if continuum and line optical depths ($\tau_C$, $\tau_L$) $\ll 1$.

Rapid decrease of line peak intensity with $\Delta n$ makes observations of high-order RRLs challenging. Line-to-continuum integral intensity for ($\tau_C$, $\tau_L$) $\ll 1$ is given by

$$\frac{\int I_{\rm L} d\nu}{I_{\rm C}} = 1.301 \times 10^5 \Delta n \, \frac{f_{n,n+\Delta n}}{n} \, \frac{\nu^{2.1}}{T_e^{1.15}} \, F \, \exp\left(\frac{1.579 \times 10^5}{n^2 T_e}\right), \quad (1)$$

where $f_{n,n+\Delta n}$ is the oscillator strength, $T_e$ is electron temperature, and $F \approx 0.925$ corrects for the contribution of ionized helium (Gordon & Sorochenko 2009). Assuming a constant frequency and using an expression for the oscillator strength as a function of $n$ and $\Delta n$ (Menzel 1969), it follows that the line integral intensity is $\int I_{\rm L} d\nu \propto \Delta n^{-1.9}$. For small $n$, Doppler broadening dominates with the Doppler width, $w_{\rm D} \propto \nu =$ constant, so the line peak intensity drops as approximately $\Delta n^{-1.9}$. For large $n$, Stark broadening dominates with line width, $w_{\rm L}$, growing as $w_{\rm L} \propto n^4 \propto \Delta n^{4/3}$, so the line peak intensity drops rapidly, as approximately $\Delta n^{-3.2}$. Therefore, detecting high ($n$, $\Delta n$) RRLs requires low system noise, baseline stability and a careful data reduction procedure.

Smirnov et al. (1984) observed high-order RRLs for $n = 90, \ldots, 174$ and $\Delta n = 1, \ldots, 6$. They used different radio telescopes at different frequencies such that the RT beamwidths remained nearly constant. They used high-frequency RRLs H56$\alpha$ and H66$\alpha$ to estimate the Doppler width to be removed from the higher-$n$ spectral lines to extract Lorentz widths from the assumed Voigt profiles, and then analyzed them to test Stark broadening theory.

Rood et al. (1984) searched for the 8.7 GHz hyperfine line of $^3He^+$ in the Orion nebula and other galactic H II regions. In this

search they detected high-order RRLs from H114$\beta$ to H178$\theta$, but did not address Stark broadening.

Bell et al. (2000, 2011) observed high-order RRLs at 6 and 17.6 GHz using a novel frequency switching (FS) method. Mathematically, this method is equivalent to applying a finite difference—a discrete analog of differentiation—to the observed spectrum (Alexander & Gulyaev 2012). In Bell et al. (2000, 2011), FS was applied to the same spectrum six times successively (a 6th order finite difference), which made their method *increasingly insensitive* to line broadening as the line width increased and exceeded the FS offset parameter. Alexander & Gulyaev (2012) demonstrate that the narrowing of RRLs reported by Bell et al. (2000, 2011) is apparent: their method effectively filtered out Stark broadening for $n \gtrsim 200$. Most of the width measurements reported in Bell et al. (2000, 2011) for $n \gtrsim 200$ were below Doppler width and increasingly below $3\sigma$ in signal-to-noise ratio (S/N), which is a manifestation of limitations in the use of the multiple FS method.

Here we report on observations of high-order RRLs in the Orion nebula (M42), obtained with the ATCA (Australia Telescope Compact Array; Wilson et al. 2011) in the frequency range 5.47—6.53 GHz. Within this band we identify and analyze 41 $\Delta n = 1,\ldots,5$ spectral lines of hydrogen. We increase S/N by stacking spectral lines of equal $\Delta n$ detected in the 1 GHz bandpass. We extract Lorentz widths and compare them with the observational findings of Smirnov et al. (1984) and Bell et al. (2000, 2011) and the predictions of electron impact broadening theory (Griem 1967, 1974; Gee et al. 1976; Watson 2006; Peach 2015). We find excellent agreement between theory and our results. Our findings are consistent with an absence of line narrowing for $n = 100...179$.

## 2. OBSERVATIONS AND DATA PROCESSING

We observed the central brightest continuum region of M42 (R.A. = 05:35:17.3, decl. = −05:23:28, J2000) at 6 GHz using the ATCA between 2013 late June and early July. Three observational time periods totaled 17 hr; accounting for calibration overheads, we obtained 15 hr of integration on M42. For maximum sensitivity, we used the compact H75 configuration with a beam-size of 7.″8 per telescope and a synthesized beam-size of 1.″8 × 2.″1 at 6 GHz. At the start of each observation time slot, we observed a primary calibrator, the unresolved (for ATCA) radio source PKS 1934-638 (R.A. = 19:39:25.0, decl. = −63:42:46, J2000; ∼5 Jy at 6 GHz) for ∼15 minutes, and used it to correct (prior to observing M42) residual delays due to differences in signal propagation times through ATCA's electronic pathways (Fomalont & Perley 1999). After every 30 minutes of integration on M42, we observed a secondary calibrator, the quasar PKS 0539-057 (R.A. = 05:41:38.1, decl. = −05:41:49.43, J2000; ∼1 Jy at 6 GHz) for ∼2 minutes, to correct time-dependent gain and phase changes. Postprocessing was done using Miriad (Sault et al. 1995) and Python's Astropy package (Astropy Collaboration et al. 2013).

Bandpass calibration was initially obtained using the primary calibrator, but we find that its S/N is too low for detecting the weakest (highest $\Delta n$) RRLs reported here. Instead, we used the unresolved (for ATCA) quasar PKS 1253-055 (R.A. = 12:56:11.2, decl. = −05:47:21.5; ∼15 Jy at 6 GHz), observed a day prior to the start of the observations reported here. The S/N of this calibrator was further improved by smoothing with a 16 channel moving average window. Flux calibration was obtained using the primary calibrator.

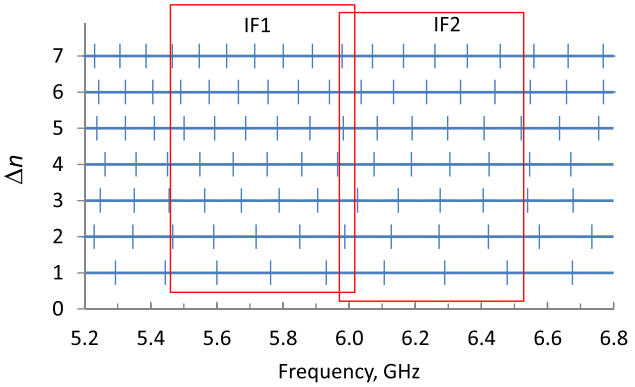


**Figure 1.** RRL frequencies and bandpasses (IF1 and IF2) used in our observations. Short vertical lines show rest frequencies of RRLs ($x$-axis); the $y$-axis shows $\Delta n$ for these lines up to $\Delta n = 7$.

**Table 1**
Hydrogen RRLs Recorded and Analyzed in this Paper

| $\Delta n$ | 1 | 2 | 3 | 4 | 5 |
|---|---|---|---|---|---|
| Range of $n$ | 100–105 | 126–132 | 144–151 | 158–166 | 169–179 |
| # of stacked lines | 6 | 7 | 8 | 9 | 11 |
| FWHM, kHz | 538 ± 2 | 610 ± 7 | 694 ± 22 | 798 ± 52 | 920 ± 135 |

**Note.** The last row provides measured widths (FWHM) of stacked lines for each $\Delta n$. Errors are provided at the level of $3\sigma$.

We used a 1 GHz bandpass option of the ATCA's Compact Array Broadband Backend (CABB; Wilson et al. 2012). CABB's wideband mode uses two simultaneous IF (intermediate frequencies), providing two bandpasses, each 544 MHz wide. One IF was centered on 5744 MHz and the other was centered on 6260 MHz, creating a 28 MHz overlap. This enormous bandpass allowed simultaneous observations of multiple RRLs with the same $\Delta n$, including 6 $\alpha$-lines, 7 $\beta$-lines, and so on, up to 11 $\Delta n = 5$ lines. Our choice of frequency range was dictated by our intention to minimize the number of overlapping RRLs in the band.

Figure 1 shows schematically the two bandpasses (IF1 and IF2) used in our observations. Short vertical lines show theoretical rest frequencies of RRLs in the spectrum ($x$-axis) for different $\Delta n$ ($y$-axis).

To reliably measure line profiles and widths, in each bandpass we concatenated 16 half-overlapped 64 MHz wide "zoom windows" with 31.25 kHz channel-widths (CFB 64M-32 configuration). This spectral resolution (1.5 km s$^{-1}$ at 6 GHz) is noticeably higher than that in the aforementioned works of Bell et al. (2000, 2011; 3.9 km s$^{-1}$ at 6 GHz and 5.32 km s$^{-1}$ at 17.6 GHz), Rood et al. (1984; 2.7 km s$^{-1}$), or Smirnov et al. (1984; 3.8 km s$^{-1}$ at 5 GHz and 2.1 km s$^{-1}$ at 9 GHz).

Table 1 summarizes the data presented in Figure 1 and provides the range of principal quantum numbers for the transitions $n + \Delta n \rightarrow n$, and the number of hydrogen lines for each $\Delta n$ in the 1 GHz bandpass. To improve S/N, RRLs of

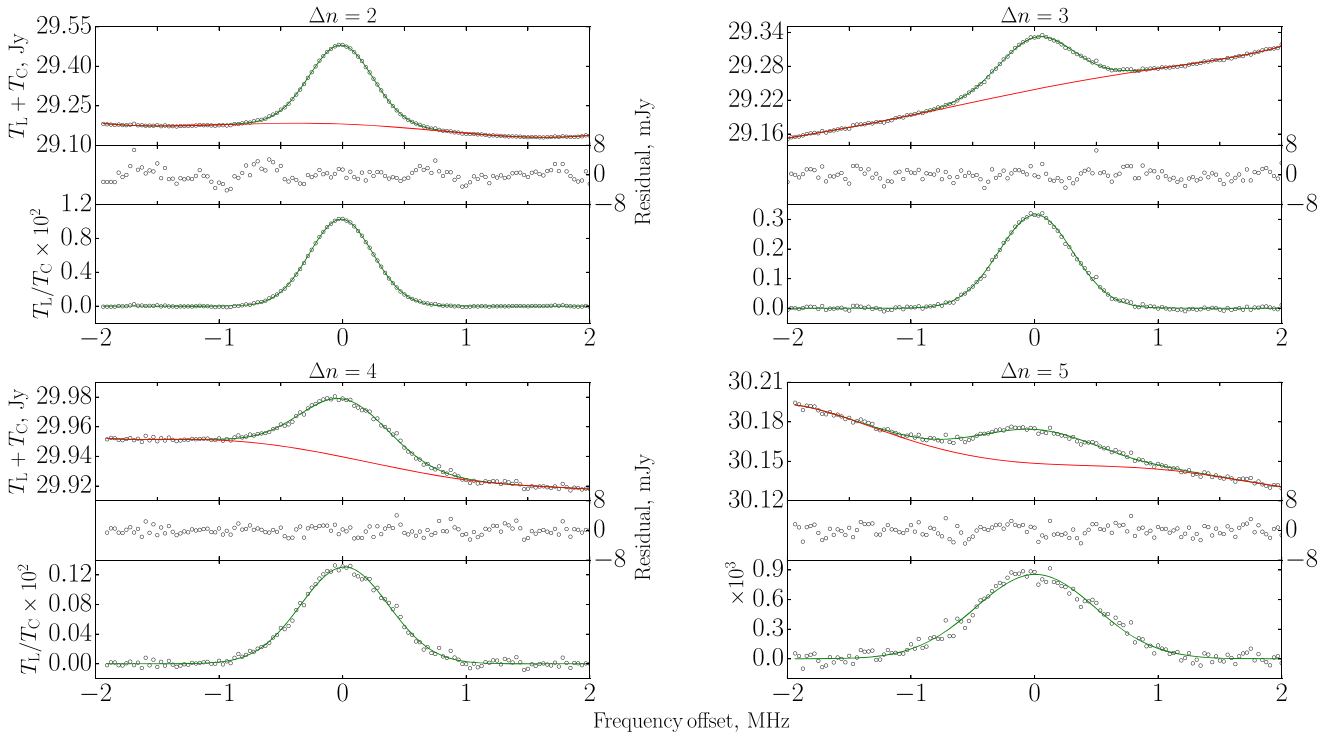


**Figure 2.** Profiles of stacked lines of equal $\Delta n$ for $\Delta n = 2, \ldots, 5$. For each $\Delta n$, the upper subplot shows the profile prior to baseline removal, the lower subplot shows the profile after baseline removal, and the middle subplot shows residuals. Red lines are 5th order polynomial baseline fits and green lines are Gaussian profile fits. $T_L$ and $T_C$ are in units of flux density, Jy; residuals are in mJy.

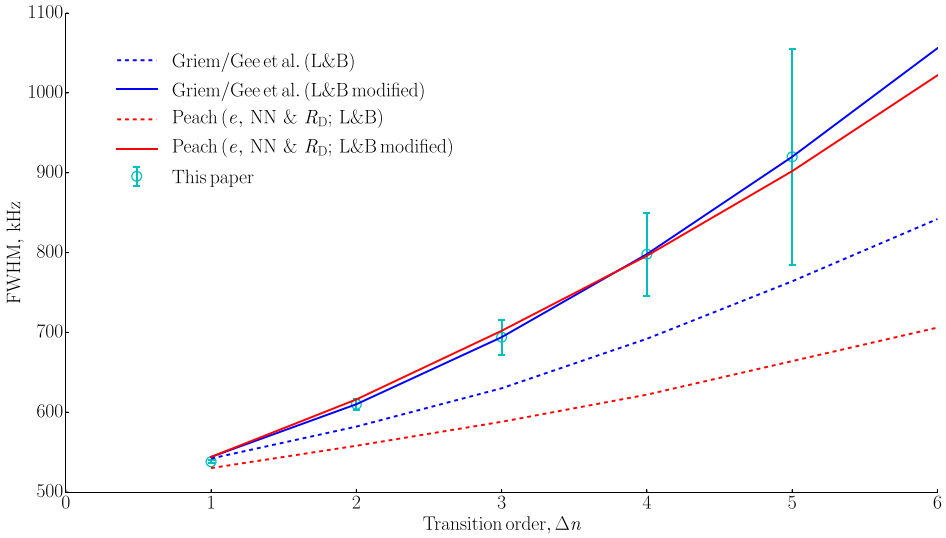


**Figure 3.** Our measurements (open circles with $3\sigma$ error bars) and model the results of the widths (FWHM) of stacked high-order RRL. The dashed curves show the results of the original Lockman & Brown (1975) model. Solid curves show the results of a modified Orion Nebula model with inhomogeneities and a filling factor. The theoretical results of Gee et al. (1976) and Peach (2015) are used for calculating impact broadening widths.

equal $\Delta n$ were stacked with respect to the theoretical central frequencies of individual lines. In the bottom row of Table 1 we provide the measured widths (FWHM) of the resulting stacked lines for each $\Delta n$. Statistical errors are indicated at the $\pm 3\sigma$ level.

Results in Table 1 (bottom row), as well as those in Figures 2–4 (below), are derived from and related to the stacked line profiles. "Effective" values of principal quantum numbers, $n_{\rm eff}$, are used in these figures: we model the stacking theoretically using the Lockman & Brown (1975) model of M42 and find that stacked line widths correspond to the widths of individual spectral lines near the bandpass' center. For example, for $\Delta n = 1$, the principal quantum numbers are in the interval $n = 100, \ldots, 105$, so $n_{\rm eff} = 102$.

We detect a systematic shift of line centers for H$n\alpha$ lines—values of $V_{\rm LSR}$ determined from positions of the line centers gradually decrease from the H100$\alpha$ to the H105$\alpha$ line. The $V_{\rm LSR}$ trend may be explained as an optical depth effect in an expanding nebula (Berulis & Ershov 1983; Gulyaev & Sorochenko 1985). All RRLs across the bandpass experience

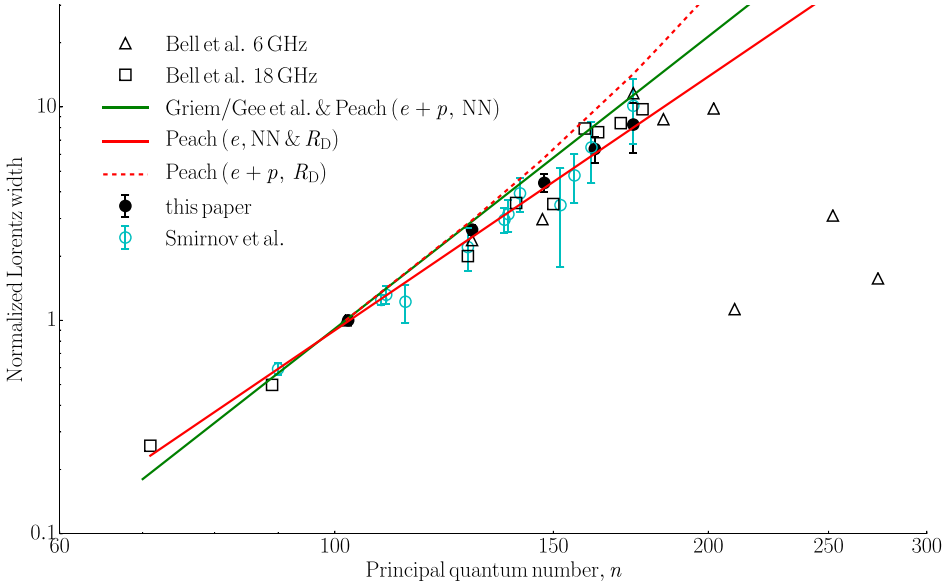


**Figure 4.** Normalized Lorentz widths of high-order RRL as a function of the principal quantum number of the lower atomic level $n$. Our observations are shown as filled diamonds with error bars ($\pm 3\sigma$). Open circles with error bars ($\pm 3\sigma$) show observations of Smirnov et al. (1984) at 5 and 9 GHz. Observations of Bell et al. (2011) are shown with open squares (17.6 GHz) and open triangles (6 GHz). The upper (green) solid line shows the theoretical prediction of Gee et al. (1976), with $w_{\rm L} \propto n^{4.55}$. The red solid line is the power law $w_{\rm L} \propto n^{3.97}$ that corresponds to Peach's (2015) theoretical calculation for electron impact broadening. It coincides with the trendline for our observations, $w_{\rm L} \propto n^{3.97\pm0.08}$, when the modified Orion nebula model with $w_{\rm D} = 25.3$ km s$^{-1}$ is used. The dashed line shows Peach's (2015) calculation of electron-plus-proton impact broadening for $\Delta E = 0$ and $\Delta E \neq 0$ transitions when the Debye radius is used as a cutoff parameter. The $n > 202$ triangles are three of seven widths reported by Bell et al. (2011) as evidence of "narrowing"; the four remaining widths cannot be shown here, as their values are below the Doppler width, and therefore formal use of Equation (11) leads to non-physical *negative* Lorentz widths.

a similar trend, i.e., stacking leads to an increased resulting-profile width. This increase is $\leqslant 1$ km s$^{-1}$ and may be ignored in the analysis of spectral line broadening.

## 3. RESULTS

Figure 2 shows stacked line profiles after baseline removal for $\Delta n = 2, \ldots, 5$. Line widths were estimated by fitting a Gaussian profile to each stacked line and a 5th order polynomial to approximate the stacked baseline shape.

Figure 3 shows our measurements (open circles with $3\sigma$ error bars) for the FWHM widths of stacked high-order RRLs. The dashed lines in Figure 3 correspond to the Orion Nebula model of Lockman & Brown (1975). This model consists of three cylindrical regions—(1) inner, (2) intermediate, and (3) outer—with densities of $N_e = 10^{4.5}$, $10^{3.5}$, and $10^{2.3}$ cm$^{-3}$, temperatures of $T_e = 7500$, 10,000 and 12,500 K, diameters = 0.043, 0.56, and 2.5 pc (0.33, 4.3, and 19.1 arcmin), and depths along the line of sight = 0.043, 0.28, and 1.25 pc, respectively. Two options for calculating impact broadening widths are used: Gee et al. (1976) and Peach (2015)—see Section 4.

The solid lines in Figure 3 correspond to the Lockman & Brown (1975) model modified to fit our data. To fit our observations we introduce a volume filling factor, $\eta$, for the Lockman & Brown (1975) model's second region, and modify its electron density. The volume filling factor is chosen as $\eta = [10^{3.5}\ {\rm cm}^{-3}/N_e({\rm region\ 2})]^2$, so the emission measure, EM, of the intermediate region remains as that of the Lockman & Brown (1975) model. This model with a filling factor is similar to an earlier three-component Orion nebula model with clumps proposed by Gulyaev & Sorochenko (1974). Unchanged EM means that the model continuum spectrum and line integral intensities remain unchanged. This modification does not noticeably effect intensities or widths of H$n\alpha$ lines computed in the Lockman & Brown (1975) model. However, we find that high-order RRLs considered here are a sensitive indicator for the presence of clumps in the central part of the Orion nebula, which was theoretically predicted and explained by Pikel'ner (1973) and Pikel'ner & Sorochenko (1973), and later confirmed by high-resolution observations at optical (e.g., Hester et al. 1991; O'dell & Wen 1994) and radio wavelengths (e.g., Churchwell et al. 1987; Garay et al. 1987; Felli et al. 1993).

To fit the theoretical (model) widths to our data in Figure 3, we use $N_e = 5000$ cm$^{-3}$ when applying the electron impact broadening of Gee et al. (1976) and $N_e = 7500$ cm$^{-3}$ when applying the impact broadening of Peach (2015). The filling factors are, correspondingly, 0.40 and 0.18.

## 4. DISCUSSION

In the electron impact broadening theory (Griem 1967), the spectral line (Lorentz) width

$$w_{\rm L} \propto n^4 \ln\left(\frac{\rho_{\rm max}}{\rho_{\rm min}}\right) \propto n^{\beta}, \qquad (2)$$

where $\beta$ depends on the choice of maximum, $\rho_{\rm max}$, and minimum, $\rho_{\rm min}$, cutoff radii (impact parameters). The minimum cutoff radius is typically chosen as

$$\rho_{\rm min} = \sqrt{\frac{5}{6}}\,\frac{n^2\hbar}{mv_e} \qquad (3)$$

(Griem 1967), where $\hbar$ is Planck's constant, and $m$ and $v_e$ are electron mass and velocity.

There are different approaches with respect to the choice of $\rho_{\rm max}$ that lead to different dependences of the electron impact

**Table 2**
Doppler Widths, $w_D$, and the Exponent $\beta$ from Equation (2), Computed for Five Sets of High-order RRL Observations

| Frequency (GHz) | Range of $\Delta n$ | Range of $n_{low}$ | $w_D$ (km s$^{-1}$) | $\beta$ | References |
|---|---|---|---|---|---|
| 5 | 1–4 | 109–174 | 26.0 ± 0.25 | 3.86 ± 0.16 | Smirnov et al. (1984) |
| 5.5–6.5 | 1–5 | 100–179 | 25.3 | 3.97 ± 0.08 | This paper |
| 6 | 1–6 | 102–194 | 25.8 | 3.97 ± 0.54 | Bell et al. (2011) |
| 9 | 1–6 | 90–161 | 25.2 ± 0.5 | 4.15 ± 0.22 | Smirnov et al. (1984) |
| 17.6 | 1–17 | 71–177 | 24.0 | 3.97 ± 0.18 | Bell et al. (2011) |

width on $n$. If

$$\rho_{max} = \frac{v_e}{\omega_{n,n\pm1}} \propto n^3, \quad (4)$$

(Griem 1967), where $\omega_{n,n\pm1} = 2\pi\nu_{n,n\pm1}$ is the angular frequency of transition $n \rightarrow n \pm 1$, substitution of (3) and (4) into (2) results in $\rho_{max}/\rho_{min} \propto n$ and $\beta > 4$. For a typical H II region electron temperature of $T_e = 10^4$ K, Equation (2) predicts

$$w_L \propto n^{4.4} \quad (5)$$

(Griem 1967) for $n \rightarrow n \pm 1$ transitions ($n \gg 1$). If the Debye radius, $R_D$, is used instead as the maximum cutoff radius, then

$$\rho_{max} = R_D = \sqrt{\frac{kT_e}{8\pi N_e e^2}}, \quad (6)$$

(Hey 2012; Peach 2015), where $k$ is the Boltzmann constant and $e$ is the elementary charge. In this case, $\rho_{max}/\rho_{min} \propto n^{-2}$, and $\beta < 4$. For a typical H II region electron density of $N_e = 10^4$ cm$^{-3}$, Equation (2) predicts $w_L \propto n^{3.97}$ (Peach 2015). Watson (2006) provides a theoretical expression for electron impact widths valid for $n \leqslant 70$. His proposed formula for $n > 70$ (Equations (16) and (17) in Watson 2006) results in $w_L \propto n^{3.97}$, consistent with the theoretical results of Peach (2015).[1]

Peach (2015) also tests a stronger condition—the NN (nearest neighbor) radius, $R_{NN}$, as the maximum cutoff radius:

$$\rho_{max} = R_{NN} = \left(\frac{3}{4\pi N_e}\right)^{1/3}.$$

Gee et al. (1976) provide a useful approximation for collisional cross-sections for inelastic electron impacts. Using a power-law presentation, one can write:

$$\langle \sigma(n) v \rangle \propto n^{\gamma}. \quad (7)$$

The collisional line width for the transition $n + \Delta n \rightarrow n$ is then (Sobel'man et al. 1995)

$$w_L = N_e [\langle \sigma(n + \Delta n) v \rangle + \langle \sigma(n) v \rangle] \propto N_e\, n^{\gamma} \times \left(1 + \frac{\gamma}{2}\frac{\Delta n}{n} + \frac{\gamma(\gamma - 1)}{2 \cdot 2!}\left(\frac{\Delta n}{n}\right)^2 + \ldots\right) \quad (8)$$

using a Taylor series expansion. The first two terms of this expansion in Equation (8) were used by Smirnov et al. (1984) in their approximate formula for the Lorentz width (Equation (2.60) in Gordon & Sorochenko 2009):

$$w_L = 8.2\, N_e \left(\frac{n}{100}\right)^{\gamma}\left(1 + \frac{\gamma}{2}\frac{\Delta n}{n}\right) \propto n^{\beta}. \quad (9)$$

For H$n\alpha$ lines, one can ignore the difference between exponents $\beta$ and $\gamma$ used in different presentations of the line width (see (2) and (8)). For example, for $n = 100$, the exponent $\beta = 4.41$ when $\gamma = 4.40$. However, when considering the widths of the sequence of high-order RRL, the difference between $\beta$ and $\gamma$ should be taken into account. For example, for our sequence of RRLs at 6 GHz, $\beta = 4.50$ when $\gamma = 4.40$. For the interval $\beta = 3.8 \ldots 4.5$ considered here, the relationship

$$\beta - \gamma = 0.10 \quad (10)$$

holds for the high-order RRL series. We use it below when comparing our results with the theoretical findings of Griem (1967), Gee et al. (1976), Watson (2006), and Peach (2015), and with the observational data of Smirnov et al. (1984) and Bell et al. (2011).

To extract Lorentz widths $w_L$ (FWHM) from the observed high-order RRL profiles, we use the approximate formula of Kielkopf (1973) presented by Smirnov (1985) as

$$w_L = 7.786\, w_V [1 - \sqrt{1 - 0.240(1 - (w_D/w_V)^2)}], \quad (11)$$

where $w_V$ is the Voigt width (FWHM) of the spectral line determined by the fitting procedure and $w_D$ is the Doppler width (FWHM). Given that the Lockman & Brown (1975) Orion nebula model has a temperature gradient, Doppler widths are different for different regions, so the Doppler width $w_D$ used in (11) is an "effective" Doppler width. For our observations at 5.5–6.5 GHz, the intermediate (second) region of both the modified and the original Lockman & Brown (1975) models dominates in terms of RRL and continuum flux, so the effective Doppler width is close to that of the intermediate region.

Following Watson (2006) and Peach (2015), we normalize Lorentz widths $w_L$ to the Lorentz width of H102$\alpha$, where $n = 102$ corresponds to the effective $n$ of the series of H $n\alpha$ lines in our case.

Using Equation (11) we re-calculate Lorentz widths from data provided by Smirnov et al. (1984) at 5 and 9 GHz (Table 2 in Smirnov et al. 1984) and by Bell et al. (2011) at 6 and 17.6 GHz ("corrected" widths in Tables 2 and 4 of Bell et al. 2011).[2] We normalize the calculated $w_L$ values by the Lorentz width of H102$\alpha$ and plot them in Figure 4.

Figure 4 shows the aforementioned theoretical trends based on the impact broadening theory and five observational sets for

[1] We find two misprints in Equation (19) of Watson (2006): there should not be an electron charge $e$ in the first line of the formula and the numerical coefficient in the second line should be $3.7 \times 10^{-11}$.

[2] All re-calculated values agree with those provided in Smirnov et al. (1984), except for the widths of two lines, H137$\beta$ and H138$\beta$, which we corrected.

the high-order RRLs: Smirnov et al. (1984) data at 5 and 9 GHz (open circles with error bars), our data at 6 GHz (filled circles with error bars), and Bell et al. (2011) data at 6 GHz (open triangles) and 17.6 GHz (open squares).

Table 2 combines our results for all five sets of the high-order RRL data. The value of $\beta$ in Equation (2) depends on the Doppler width used for each data set (Column 4). The weighted least-squares method is used to find the exponent $\beta$ for each set of data (Column 5).

Smirnov et al. (1984) report a best-fit parameter $\gamma = 4.4 \pm 0.6$ for their 9 GHz lines and $\gamma = 3.78 \pm 0.16$ for their 5 GHz lines, where $\gamma$ is the exponent in the power law describing the collisional cross-section for inelastic electron impacts (7). Using the weighted least square method we reprocess the data of Smirnov et al. (1984) and find $\beta = 3.86 \pm 0.16$ for their 5 GHz measurements and $\beta = 4.15 \pm 0.22$ for the 9 GHz lines when using their values of $w_{\rm D}$ ($26.0 \pm 0.25$ km s$^{-1}$ and $25.2 \pm 0.5$ km s$^{-1}$, respectively). From Equation (10), $\gamma = 3.76 \pm 0.16$ for their 5 GHz data, which agrees with $\gamma = 3.78 \pm 0.16$ reported in Smirnov et al. (1984). Using Equation (10), we find $\gamma = 4.05 \pm 0.22$ for their 9 GHz data, while Smirnov et al. (1984) report $\gamma = 4.4 \pm 0.6$. This discrepancy is rather large, but remains inside the error margins.

Normalized widths $w_{\rm L}$ computed from Bell et al. (2011) at 6 GHz drop significantly for $n \gtrsim 200$ (Figure 4). This is expected given that the multiple FS method applied in Bell et al. (2000, 2011) is *insensitive* to line broadening and produces processed widths dominated by measurement errors when $n \gtrsim 200$. Four of seven line widths at 6 GHz with $n > 202$ reported by Bell et al. (2000, 2011) cannot be shown in Figure 4 because their widths are narrower than the Doppler width, resulting in *negative* Lorentz widths when using Equation (11). The remaining three lines are outliers. Though they have positive Lorentz widths, they are significantly effected by the six-times-FS applied by Bell et al. (2000) and do not represent meaningful line widths (Alexander & Gulyaev 2012).

Bell et al. (2000, 2011) do not provide errors for individual width measurements. However, in their Figure 1 caption, Bell et al. (2000) state "the measured errors in the line widths increase from ~8% at low $n$-values to 25%–30% at high $n$." Using this indication, we computed weighted fittings to their results at 6 and 17.6 GHz. When using $w_{\rm D} = 24.0$ km s$^{-1}$ for their 17.6 GHz data, we find $w_{\rm L} \propto n^{3.97 \pm 0.18}$. Using $w_{\rm D} = 25.8$ km s$^{-1}$ for their 6 GHz data and excluding the three obvious outliers, we get $w_{\rm L} \propto n^{3.97 \pm 0.54}$ (Table 2).

The effective Doppler widths used here to extract Lorentz widths from our data and the data of Smirnov et al. (1984) and Bell et al. (2011) vary between 24 and 26 km s$^{-1}$ (Table 2). The lower-frequency data show higher $w_{\rm D}$ and the higher-frequency data require lower $w_{\rm D}$, which agrees with the Orion nebula model used here. At lower frequencies, the role of the outer (third) region with its higher temperature becomes more important and therefore $w_{\rm D}$ increases. At higher frequencies, the role of the central region with its lower temperature becomes more important and therefore $w_{\rm D}$ decreases.

The observational data presented in Figure 4 best agree with the computations of Peach (2015) for electron impact broadening (solid red line), with the Debye or nearest neighbor radius as the maximum impact parameter and $w_{\rm L} \propto n^{3.97 \pm 0.54}$.

A question arises: can Doppler widths $w_{\rm D}$ in Equation (11) be chosen such that the Lorentz widths of the five sets of high-order RRLs satisfy the power law $w_{\rm L} \propto n^{4.55}$ predicted from Gee et al. (1976)? The answer is probably "yes." By slightly changing the parameters of the nebula model, agreement with the $w_{\rm L} \propto n^{4.55}$ law for Lorentz widths can be reached (Figure 3). However, the Doppler widths in Table 2 agree better with the values of $w_{\rm D}$ used by Smirnov et al. (1984) to interpret their 5 GHz ($w_{\rm D} = 26 \pm 0.2$ km s$^{-1}$) and 9 GHz ($w_{\rm D} = 25.2 \pm 0.5$ km s$^{-1}$) data. To get $\beta = 4.55$ for their 5 and 9 GHz data, the Doppler width in Equation (11) should be taken as high as $w_{\rm D} = 26.7$ and 25.4 km s$^{-1}$ for their 5 and 9 GHz data, respectively, which does not agree well with Doppler widths determined by Smirnov et al. (1984).

We conclude that the power law predicted by electron impact broadening theory is consistent with the five sets of high-order RRLs analyzed here. Our data do not allow an unambiguous choice between the theoretical results of Griem (1967) and Gee et al. (1976) ($w_{\rm L} \propto n^{4.55}$) and the results of Peach (2015) and Watson (2006) ($w_{\rm L} \propto n^{3.97}$). This ambiguity arises from the small difference in the nebula model parameters corresponding to $\beta = 3.97$ and $\beta = 4.55$. It appears to currently be impossible to determine the turbulent velocities and other physical and geometric parameters of the Orion nebula with sufficient accuracy to choose between the two predictions of electron impact broadening theory.

The dashed curve in Figure 4 corresponds to Peach's (2015) model for electron-plus-proton impacts with the Debye radius as the maximum impact parameter. This model significantly deviates from experimental trends to be considered a meaningful description of the high-order RRL observations.

We detected 41 high-order RRLs of hydrogen from the Orion nebula at 6 GHz with the ATCA using a 1 GHz wide bandpass. We stacked lines of equal $\Delta n$ and extracted Lorentz widths to test Stark spectral line broadening theory of cosmic plasma. We analyzed the results, together with those of Smirnov et al. (1984) at 5 and 6 GHz and the statistically reliable data of Bell et al. (2000, 2011) at 6 and 17.6 GHz, and demonstrate that electron impact broadening theory is consistent with the five sets of measurements considered here. These data confirm the absence of line narrowing for $n = 71...179$. We find that a model of the Orion nebula with density inhomogeneities and gradients of density and temperature (Gulyaev & Sorochenko 1974; Lockman & Brown 1975) fits our measured high-order RRL data well.

We thank Miller Goss, Warwick Wilson, and Peter Thomasson for useful discussions, and Maxim Voronkov for help with observations and data reduction. We thank the ATCA for providing observational time, which is funded by the Commonwealth of Australia for operation as a National Facility managed by CSIRO.

## REFERENCES

Alexander, J., & Gulyaev, S. 2012, ApJ, 745, 194
Astropy Collaboration, Robitaille, T. P., Tollerud, E. J., et al. 2013, A&A, 558, A33
Bell, M. B., Avery, L. W., MacLeod, J. M., & Vallée, J. P. 2011, Ap&SS, 335, 451
Bell, M. B., Avery, L. W., Seaquist, E. R., & Vallée, J. P. 2000, PASP, 112, 1236
Berulis, I. I., & Ershov, A. A. 1983, SvAL, 9, 341
Castaneda, H. O. 1988, ApJS, 67, 93

Churchwell, E., Felli, M., Wood, D. O. S., & Massi, M. 1987, ApJ, 321, 516
Felli, M., Churchwell, E., Wilson, T. L., & Taylor, G. B. 1993, A&AS, 98, 137
Fomalont, E. B., & Perley, R. A. 1999, in ASP Conf. Ser. 180, Synthesis Imaging in Radio Astronomy II, ed. G. B. Taylor, C. L. Carilli, & R. A. Perley, (San Francisco, CA: ASP), 79
Garay, G., Moran, J. M., & Reid, M. J. 1987, ApJ, 314, 535
Gee, C. S., Percival, L. C., Lodge, J. G., & Richards, D. 1976, MNRAS, 175, 209
Goldschmidt, E. A., Norris, D. G., Koller, S. B., et al. 2015, PhRvA, 91, 032518
Gordon, M. A., & Sorochenko, R. L. 2009, Radio Recombination Lines: Their Physics and Astronomical Applications (New York: Springer)
Griem, H. R. 1960, ApJ, 132, 883
Griem, H. R. 1967, ApJ, 148, 547
Griem, H. R. 1974, Spectral Line Broadening by Plasmas, Vol. 39 (New York: Academic)
Gulyaev, S. A., & Sorochenko, R. L. 1974, AZh, 51, 1237
Gulyaev, S. A., & Sorochenko, R. L. 1985, AbaOB, 59, 135
Hester, J. J., Gilmozzi, R., O'dell, C. R., et al. 1991, ApJL, 369, L75
Hey, J. D. 2012, JPhB, 45, 065701
Kielkopf, J. F. 1973, JOSA, 63, 987
Lisitsa, V. S., Bureyeva, L. A., Kukushkin, A. B., et al. 2012, JPhCS, 397, 1
Lockman, F. J., & Brown, R. L. 1975, ApJ, 201, 134
Matsakis, D. N., Palmer, P., & Harris, A. I. 1982, NYASA, 395, 210
Menzel, D. H. 1969, ApJS, 18, 221
Minaeva, L. A., Sobel'Man, I. I., & Sorochenko, R. L. 1967, AZh, 44, 995
O'dell, C. R., & Wen, Z. 1994, ApJ, 436, 194
Peach, G. 2015, JApA, 36, 555
Peach, G., Dimitrijevic, M. S., & Stancil, P. C. 2009, IAUTA, 27, 385
Pikel'ner, S. B. 1973, ApL, 15, 91
Pikel'ner, S. B., & Sorochenko, R. L. 1973, AZh, 50, 693
Rood, R. T., Bania, T. M., & Wilson, T. L. 1984, ApJ, 280, 629
Sault, R. J., Teuben, P. J., & Wright, M. C. H. 1995, in ASP Conf. Ser. 77, Astronomical Data Analysis Software and Systems IV, ed. R. A. Shaw, H. E. Payne, & J. J. E. Hayes, (San Francisco, CA: ASP), 433
Smirnov, G. T. 1985, PAZh, 11, 17
Smirnov, G. T., Sorochenko, R. L., & Pankonin, V. 1984, A&A, 135, 116
Sobel'man, I., Vainshtein, L., & Yukov, E. 1995, Excitation of Atoms and Broadening of Spectral Lines (Berlin: Springer)
Sorochenko, R. L., & Berulis, J. J. 1969, ApL, 4, 173
Watson, J. K. G. 2006, JPhB, 39, 1889
Wilson, T. L., Casassus, S., & Keating, K. M. 2012, ApJ, 744, 161
Wilson, W. E., Ferris, R. H., Axtens, P., et al. 2011, MNRAS, 416, 832
Wink, J. E., Wilson, T. L., & Bieging, J. H. 1983, A&A, 127, 211

## Errata

1. The second to last sentence in Figure 2's caption should read:

   "Red lines are 5th order polynomial baseline fits and green lines are Voigt profile fits."

2. In Footnote 1, I state that there should not be electron charge in Watson (2006), Equation 19. I thank Prof. J. D. Hey for bringing to my attention that "*e*" in this equation is the base of natural logarithm, not the charge of the electron. This footnote is thus unnecessary.

3. In addition to Hey (2012), I also add reference to Hey (2013) which explores the role of atomic polarizability in RRL spectra from HII regions. I thank Prof. Hey for bringing this to my attention.

4. The third citation in the REFERENCES section should read:

   "Bell, M. B., Avery, L. W., MacLeod, J. M. & Vallée, J. P. 2011, Ap&SS, 333, 377"

# 5 Conclusion & future work

"A look into the beyond." *Anonymous*

## 5.1 Conclusion

In Chapter 1 I introduce RRLs as a sensitive probe of laboratory and cosmic plasmas from which they emanate. This is followed by a history of the theory and observations of RRLs, starting with Soviet astronomer Kardashev's prediction of their detectability in 1959, then with their detection by Soviet astronomers in 1964 and finishing with Canadian astronomers' curious finding that the behavior of high-order RRL widths are not as expected. Chapter 2 presents the modern theory of RRLs, including the distribution of excited electronic states, transition probabilities between these states, radiative transfer, and spectral line broadening mechanisms. Chapter 3 details my original ATCA observations and processing of cosmic high-order RRLs data from the Orion neb-

ula. Chapter 4 introduces and summarizes my co-published papers contained therein. And finally, Chapter 5 concludes the dissertation by summarizing its original contribution and suggesting future prospects.

In this dissertation, I demonstrate that the apparent hydrogen RRL narrowing first reported by Bell et al. is an artifact of their data processing. I accomplish this by creating a theoretical model of the multiple FS (frequency shifting) technique, which is then implemented as a computer simulation. This technique, originally developed by Bell, copies a spectral line bandpass, shifts it in frequency by an offset, and adds it to the unshifted bandpass. The output of this process is then fed back to itself multiple times. I then co-created a theoretical model of the Orion nebula which includes mechanisms of spectral line broadening and non-equilibrium thermodynamics effects. This model is used to numerically solve the radiative transfer problem to simulate hydrogen RRLs. These simulated lines are then processed through my multiple FS model, the results of which are called "processed" lines — a term introduced by Bell. Finally, I use Monte Carlo simulation to estimate how noise influences the processed line widths and amplitudes.

From these models and simulations, I discovered that multiple FS does not preserve broadening when the original line width is greater than the FS-offset. In this case, I find the processed width results manifest the narrowing reported by Bell et al., by reducing broad spectral wings characteristic of Stark broadened

RRLs. I also discovered that the S/N of processed lines *reduces* weakly with the number of overlaps as a result of adding *dependent* samples. This means the S/N of processed lines as a function of $\Delta n$ (transition-order), at fixed frequency, decreases faster than for unprocessed lines, such that a given statistical insignificance level is reached more quickly.

Given this analysis, I argue Bell et al.'s $\Delta n > 11$ lines are artifacts of their technique. I conclude that their reported findings, upon re-examination of their novel data processing technique, do not indicate a need to revise Stark broadening theory.

I present original observations of high-order RRLs from the Orion nebula conducted by myself to test the theory of Stark broadening in cosmic plasmas. I used a wide 1 GHz bandpass centered at 6 GHz to significantly improve the accuracy of measurements by stacking up to eleven hydrogen RRLs of the same $\Delta n$. As a result of stacking and spectral resolution, the uncertainties in the measured lines widths are about two-times less than was achieved before by Smirnov et al. (1984). I find no evidence of spectral line narrowing. I show that all statistically significant data from my observations and four-sets of previous observations of high-order hydrogen RRLs (Smirnov et al., 1984; Bell et al., 2011) are in agreement and demonstrate how Stark broadening theory is consistent with these observations. I find that Lockman and Brown (1975)'s RRL model of the Orion nebula over a large range of radio frequencies and $\Delta n \leq 2$ requires

the addition of small-scale density inhomogeneities (clumps) and turbulence to adequately predict my observed hydrogen RRLs for $\Delta n \leq 5$.

I demonstrate that the power law predicted by electron-impact Stark broadening theory is consistent with the five-sets of high-order hydrogen RRLs analyzed here. Neither previous measurements nor my more precise data allow distinguishing between two approaches to the cut-off parameters (nearest neighbor versus Debye radius) when predicting line broadening from electron impacts. Specifically, these data do not allow an unambiguous choice between the theoretical results of Griem (1967); Gee et al. (1976) and Watson (2006); Peach (2015). This ambiguity arises from small differences in the radiative transfer nebula model parameters required to fit these theoretical predictions to observations. It is currently impossible to independently determine turbulent velocities and other physical & geometric parameters of the Orion nebula with enough accuracy to choose between the two predications of electron-impact broadening theory. This situation represents an ill-posed inverse problem that is currently unsolvable (Brown et al., 1978). However, I am able to show that Peach's model for electron-plus-proton impacts significantly deviates from the Lorentz-width trend in my data.

In summary, the original contributions of this dissertation are as follows.

1. A mathematical theory of multiple frequency switching method is devel-

oped.

2. Mathematical modeling of the MFS with the presence of noise is conducted for the first time with the use of Monte-Carlo method. It is shown that

    a) the observed line widths depend on the main MFS parameter – the frequency offset.

    b) the apparent line widths in the MFS are not greater than the frequency offset.

    c) in the presence of noise, apparent narrowing of spectral lines can take place when the S/N becomes small, consistent with unexpected Orion nebula observations reported by Bell et al.

3. ATCA/CABB is used for the first time for wide-band high-resolution precision spectroscopy. High efficiency of this technique is demonstrated.

4. For the first time the method of stacking of up to eleven high-order RRLs is used, which allowed reaching an unmatched precision in measuring spectral line parameters.

5. For the first time five sets of high-order RRL observations are brought together, and it is demonstrated that

    a) all sets of observations are in accord, including statistically significant observations of Bell et al.

b) the high-order RRLs are broadened according to the electron-impact Stark broadening theory.

c) Peach's results on electron-plus-proton broadening deviates significantly from observations.

d) Bell et al.'s results demonstrate apparent narrowing for low S/N in accordance with prediction of our MFS mathematical theory and computational modeling.

6. For the first time, it was attempted to observationally distinguish between two approaches to the choice of maximum cut-off radius of the impact parameter: Debye radius versus nearest-neighbor. It is demonstrated that even with the highest precision achieved in the observations, this distinction is not yet achievable. The reason for this is complex geometry and inhomogeneity of the real nebulae, as well as sensitivity of spectral lines to physical parameters of the model regions in which they are formed. An important role of turbulent velocity is demonstrated.

7. A radiation transfer model of the Orion nebula with gradients of temperature and density is created and numerically solved/optimized against observational data. It is demonstrated that observations and theory agree if clumps of high density are present in the core region of the model — in accord with recent high-resolution observations of the nebula and early the-

oretical models (Pikel'ner, 1973; Gulyaev and Sorochenko, 1974; O'Dell and Wen, 1994).

8. The study of the Orion nebula conducted in this thesis can be considered a case study. The results of this study and the techniques used — theoretical, computational and observational — can be applied to other galactic and extragalactic HII regions for testing spectral line theory in extreme physical conditions of plasmas, from rarefied HII regions to dense and hot plasmas of controlled thermonuclear fusion reactors.

## 5.2 Future work

More investigations can be done with the data I obtained when observing the Orion nebula with the ATCA (Australia Telescope Compact Array). In this dissertation, I concentrate on H RRLs and their widths & shapes. However, I also have high quality He and C RRL data, which can be used for modeling and determination of He and C abundances.

My H RRL data collected with ATCA and analyzed here is for $n \leq 179$, $\Delta n \leq 5$ at 6 GHz. Initially, I thought I had also detected $\Delta n = 6$ and $\Delta n = 7$ RRLs in the same data set. However, further analysis of the curve-fitting results indicated the amplitudes and wavelengths of bandpass fluctuations due to receiver instabilities become comparable to the RRL shapes themselves, such that these

weak lines are "lost in the noise". This is caused by insufficient S/N in the observed bandpass calibrator compared with the S/N of the observed source, the Orion nebula. Ideally, the S/N of a bandpass calibrator and source needs to be comparable (Westpfahl, 1999), which was not the case for my Orion observation due to limited time-allocation at the ATCA. Although I addressed this issue by smoothing the bandpass calibrator, residual bandpass fluctuations ultimately limited my detection to $\Delta n \leq 5$. Ideally, future observations of high-order RRL from this nebula using this bandpass calibrator will require that the calibrator be observed significantly longer.

A useful bandpass calibration requires a calibrator that does not make a significant contribution to the S/N of the uncalibrated bandpass. This requires the ratio of the S/N of the calibrator and S/N of the source (M42, Orion nebula) to be greater than or equal to one, i.e., $\frac{(\mathrm{S/N})_{\mathrm{cal}}}{(\mathrm{S/N})_{\mathrm{M42}}} \approx \frac{F_{\mathrm{cal}}}{F_{\mathrm{M42}}}\sqrt{\frac{\Delta t_{\mathrm{cal}}}{\Delta t_{\mathrm{M42}}}} \geq 1$, where $F_{\mathrm{cal}}$ and $F_{\mathrm{M42}}$ are the brightness of the calibrator and $\Delta t_{\mathrm{cal}}$ and $\Delta t_{\mathrm{M42}}$ are the corresponding integration times (Westpfahl, 1999). In the case of a bright source like M42, either a brighter calibrator should be used or integration time on the calibrator should be significantly increased. If PKS1934-638 is used, where $F_{\mathrm{cal}} = F_{1934-638} \approx 5\,\mathrm{Jy}$ and $F_{\mathrm{M42}} \approx 30\,\mathrm{Jy}$ at 6 GHz, then $\frac{(\mathrm{S/N})_{1934-638}}{(\mathrm{S/N})_{\mathrm{M42}}}$ attains unity when $\Delta t_{1934-638} \approx 36\Delta t_{\mathrm{M42}}$. Given my $\Delta t_{\mathrm{M42}} = 15$ hour integration on M42, 540 hours of integration on PKS 1934-638 would be required! This suggests a brighter calibrator is needed to detect $\Delta n > 5$ RRLs in Orion at 6 GHz when

using an interferometer.

A solution to the problem of $\Delta n > 5$ RRL detections has been found in the weaker source M17 (Omega nebula) and brighter calibrator PKS 1253-055.[1] One day prior to my scheduled M42 ATCA observations, serendipity occurred and I was granted unscheduled observing time on M17, using PKS 1253-055 as the bandpass calibrator.[2] At 6 Ghz, $F_{1253-055} \approx 15$ Jy and I observed M17 to be $F_{\rm M17} \approx 10$ Jy. Using the approach of the previous paragraph, the integration time required on PKS 1253-055 is about half the integration time on M17, such that their S/N ratios are comparable.

Given this ideal combination of circumstances, after about eight hours of observing, I attained a calibrated data-set superior to that of M42, which was observed over three days, totaling about 20 hours. The superiority of the M17 dataset is such that I have statistically significant, stacked H RRL detections of $\Delta n = 6$, $\Delta n = 7$ and a marginal $\Delta n = 8$ detection. Given these results and all the observing/analysis experience developed with M42, I am now working with undergraduate and graduate students to thoroughly re-analyze the visibility data and then publish these novel M17 high-order RRL findings. This will include testing predictions of high-order RRL shapes & intensities, accounting for the frequency-dependent optical depth effects on RRLs in expanding plas-

[1] During my M42 observations, this calibrator set below the local horizon while M42 rose, making it unavailable as a bandpass calibrator for same-day observations.

[2] mm-wavelength observations were scheduled at this time, but bad weather made for terrible observing. However, as it turned out, 5 cm observing was excellent.

mas (Gulyaev and Sorochenko, 1985) and developing a radiative transfer model for M17 which accounts for these high-order RRL data.

In hindsight, it can be asked why I did not originally focus on the M17 dataset? One answer is historical: the original discrepancy between measured RRL widths and theoretical prediction arose with M42 observations, so it was decided to place my focus here. Also, M42's detectability across the electromagnetic spectrum has generated a rich collection of publications, both in theory and observation that were utilized throughout this work. Another answer is naivety: I lacked familiarity with correlating interferometers, like the ATCA, particularly when choosing bandpass calibrators that minimize bandpass fluctuations to enhance detection of weak RRLs. Although the M42 dataset has been considerably more challenging from a data-processing point of view, resulting in a lower $\Delta n$-upper-limit detection than for M17, I would not have developed a deeper appreciation of the benefits and limitations of radio interferometry, the importance and propagation of statistical significance and would not have learned to write code in Python, one the most useful open-source scripting languages for the analysis and presentation of scientific data. From this perspective, the Orion nebula has been a legendary teacher.

# References

Alexander, J. and Gulyaev, S. (2012). On the apparent narrowing of radio recombination lines at high principal quantum numbers. *ApJ*, 745:194.

Alexander, J. and Gulyaev, S. (2016). Stark broadening of high-order radio recombination lines toward the orion nebula. *ApJ*, 828:40.

Aller, L. H. (1963). *Astrophysics: the atmospheres of the sun and stars*. Ronald Press, New York, 2nd edition.

Altenhoff, W. J., Mezger, P., Wendker, H., and Westerhout, G. (1960). *Veroff. Univ. Sternwarte Bonn*, (Technical report 59).

Anderson, P. W. (1949). Pressure Broadening in the Microwave and Infra-Red Regions. *Phys. Rev.*, 76:647–661.

Astropy Collaboration, Robitaille, T. P., Tollerud, E. J., Greenfield, P., Droettboom, M., Bray, E., Aldcroft, T., Davis, M., Ginsburg, A., Price-Whelan, A. M., Kerzendorf, W. E., Conley, A., Crighton, N., Barbary, K., Muna, D.,

Ferguson, H., Grollier, F., Parikh, M. M., Nair, P. H., Unther, H. M., Deil, C., Woillez, J., Conseil, S., Kramer, R., Turner, J. E. H., Singer, L., Fox, R., Weaver, B. A., Zabalza, V., Edwards, Z. I., Azalee Bostroem, K., Burke, D. J., Casey, A. R., Crawford, S. M., Dencheva, N., Ely, J., Jenness, T., Labrie, K., Lim, P. L., Pierfederici, F., Pontzen, A., Ptak, A., Refsdal, B., Servillat, M., and Streicher, O. (2013). Astropy: A community Python package for astronomy. *A&A*, 558:A33.

Baker, J. G. and Menzel, D. H. (1938). Physical processes in gaseous nebulae. III. The balmer decrement. *ApJ*, 88:52.

Barklem, P. S., Belyaev, A. K., Guitou, M., Feautrier, N., Gadéa, F. X., and Spielfiedel, A. (2011). On inelastic hydrogen atom collisions in stellar atmospheres. *A&A*, 530:A94.

Bell, J. R. (1960). *Seven into space*. Ebury Press, London.

Bell, M., Avery, L., Moore, T., and MacLeod, J. (1991). Impact broadening of hydrogen recombination lines with $\Delta n \leq 17$ in orion and w51. *JRASC*, 85:200.

Bell, M. B. (1997). A technique for removing strong continuum-related baseline structure from single-dish spectra without fitting sinusoids or polynomials. *PASP*, 109(735):609.

Bell, M. B., Avery, L. W., MacLeod, J. M., and Vallée, J. P. (2011). Sensitive

observations of radio recombination lines in orion and w51: the data and detection of systematic recombination line blueshifts proportional to impact broadening. *Ap&SS*, 333(2):377–388.

Bell, M. B., Avery, L. W., Seaquist, E. R., and Vallée, J. P. (2000). A new technique for measuring impact-broadened radio recombination lines in HII regions: Confrontation with theory at high principal quantum numbers. *PASP*, 112:1236.

Bevington, P. R. and Robinson, D. K. (2003). *Data reduction and error analysis for the physical sciences*. McGraw-Hill Higher Education. McGraw-Hill, New York, 3rd edition.

Bohr, N. (1913). On the constitution of atoms and molecules. *Phil. Mag.*, 26:1.

Bohr, N. (1914). On the spectrum of hydrogen. *Fysisk Tidsskrift*, 12:97.

Bohr, N. (1922). 7th Guthrie lecture: the effect of electric and magnetic fields on spectral lines. *Proc. Phys. Soc., London*, 35:275–302.

Boltzmann, L. E. (1868). Studien über das gleichgewicht der lebendigen kraft zwischen bewegten materiellen punkten. *Wiener Berichte*, 58:517–560.

Brocklehurst, M. and Seaton, M. J. (1972). On the interpretation of radio recombination line observations. *MNRAS*, 157:179.

Brown, R. L., Lockman, F. J., and Knapp, G. R. (1978). Radio recombination lines. *ARA&A*, 16(1):445–485.

Brunthaler, A., Reid, M. J., Menten, K. M., Zheng, X.-W., Bartkiewicz, A., Choi, Y. K., Dame, T., Hachisuka, K., Immer, K., Moellenbrock, G., Moscadelli, L., Rygl, K. L. J., Sanna, A., Sato, M., Wu, Y., Xu, Y., and Zhang, B. (2011). The bar and spiral structure legacy (bessel) survey: mapping the milky way with vlbi astrometry. *Astron. Nachr.*, 332:461.

Burgess, A. and Summers, H. P. (1976). The recombination and level populations of ions. I - hydrogen and hydrogenic ions. *MNRAS*, 174:345–391.

Carroll, B. W. and Ostlie, D. A. (1996). *An introduction to modern astrophysics*. Addison-Wesley Publishing Company, Inc., Reading.

Chandrasekhar, S. (1960). *Radiative transfer*. Dover, New York.

Chapman, S. and Cowling, T. G. (1970). *The mathematical theory of non-uniform gases*. University Press, Cambridge, 3rd edition.

Condon, J. J. and Ransom, S. M. (2016). *Essential radio astronomy*. Princeton University Press, Princeton.

Cooper, K. (2016). The rise of rydberg physics. *Physics World*, 29(4):22.

Cowley, C. R. (1970). *The theory of stellar spectra*. Gordon and Breach Science Publishers, New York.

Davies, R. D. (1971). Observations of radio recombination lines with $\Delta n = 1$ to 5. *ApJ*, 163:479.

Dicke, R. H. (1946). The measurement of thermal radiation at microwave frequencies. *Rev. Sci. Instrum.*, 17:268–275.

Dravskikh, Z. V. and Dravskikh, A. F. (1964). *Astron. Tsirk.*, 282:2.

Dupree, A. K. (1969). Radiofrequency recombination lines from heavy elements: carbon. *ApJ*, 158:491.

Efron, B. and Tibshirani, R. (1994). *An Introduction to the Bootstrap*. Chapman & Hall/CRC Monographs on Statistics & Applied Probability. Taylor & Francis, Boca Raton.

Feron, B. (2013). Computationally intensive problems of physics and astronomy: oscillator strengths and departure coefficients of the hydrogen atom in the interstellar medium. Master's thesis, Auckland University of Technology, Auckland.

Fomalont, E. B. and Perley, R. A. (1999). Calibration and Editing. In Taylor, G. B., Carilli, C. L., and Perley, R. A., editors, *Synthesis Imaging in Radio Astronomy II*, volume 180 of *ASP Conf. Ser.*, pages 79–110.

Fousse, L., Hanrot, G., Lefèvre, V., Pélissier, P., and Zimmermann, P. (2007). Mpfr: A multiple-precision binary floating-point library with correct rounding. *ACM Trans. Math. Softw.*, 33(2).

Garabedian, P. R. (2003). Computational mathematics and physics of fusion reactors. *Proceedings of the National Academy of Science*, 100:13741–13745.

GAVO Data Center (2008). Dexter for your data. VO resource provided by the GAVO Data Center.

Gee, C. S., Percival, L. C., Lodge, J. G., and Richards, D. (1976). Theoretical rates for electron excitation of highly-excited atoms. *MNRAS*, 175:209–216.

Goldberg, L. (1966). Stimulated emission of radio-frequency lines of hydrogen. *ApJ*, 144:1225–1231.

Goldschmidt, E. A., Norris, D. G., Koller, S. B., Wyllie, R., Brown, R. C., Porto, J. V., Safronova, U. I., and Safronova, M. S. (2015). Magic wavelengths for the 5*s*-18*s* transition in rubidium. *Phys. Rev. A*, 91(3):032518.

Gordon, M. A. (1988). The continuum spectra of warm cloud complexes associated with radio-bright H II regions. *ApJ*, 331:509–522.

Gordon, M. A. and Sorochenko, R. L. (2002). *Radio Recombination Lines: Their Physics and Astronomical Applications*. Kluwer Academic Publishers, Dordrecht, 1st edition.

Gordon, M. A. and Sorochenko, R. L. (2009). *Radio Recombination Lines: Their Physics and Astronomical Applications*. Springer, New York, 2nd edition.

Griem, H. R. (1960). Stark broadening of higher hydrogen and hydrogen-like lines by electrons and ions. *ApJ*, 132:883.

Griem, H. R. (1967). Stark broadening by electron and ion impacts of $n\alpha$ hydrogen lines of large principal quantum number. *ApJ*, 148:547.

Griem, H. R. (2005). On the narrowing of radio recombination lines at high principal quantum numbers. *ApJ*, 620:L133–L134.

Griem, H. R., Kolb, A. C., and Shen, K. Y. (1959). Stark broadening of hydrogen lines in a plasma. *Phys. Rev.*, 116:4–16.

Gulyaev, S. A. (1976). Profile of the Hn$\alpha$ radio lines in a static ion field. *Soviet Ast.*, 20:573.

Gulyaev, S. A. (1990). Review of the Populations of Highly-Excited States of Atoms in Low Density Plasmas. In Gordon, M. A. and Sorochenko, R. L., editors, *IAU Colloq. 125: Radio Recombination Lines: 25 Years of Investigation*, volume 163 of *Ap&SSL*, page 37.

Gulyaev, S. A. and Sorochenko, R. L. (1974). Intensity and width of the excited hydrogen radiolines in Orion nebulae. *AZh*, 51:1237–1244. English translation: 1975 Soviet Ast. 18:737–741.

Gulyaev, S. A. and Sorochenko, R. L. (1985). Catalogue of radio recombination lines: first results of a data analysis. *Bull. Abastumani Astrophys. Obs.*, 59:135–140.

Gündel, H. (1970). Zustandssumme und effektive ionisierungsspannung eines

atoms im plasma und möglichkeiten ihrer experimentellen überprüfung. Teil I. *Beiträge aus der Plasmaphysik*, 10(6):455–467.

Gündel, H. (1971). Zustandssumme und effektive ionisierungsspannung eines atoms im plasma und möglichkeiten ihrer experimentellen überprüfung. II. Experiment. *Beiträge aus der Plasmaphysik*, 11(1):1–12.

Heisenberg, W. (1927). Über den anschaulichen inhalt der quantentheoretischen kinematik und mechanik. *Z. Phys.*, 43:172–198.

Hey, J. D. (2012). On the role of atomic metastability in the production of Balmer line radiation from 'cold' atomic hydrogen, deuterium and hydrogenic ion impurities in fusion edge plasmas. *J. Phys. B*, 45(6):065701.

Hey, J. D. (2013). Does atomic polarizability play a role in hydrogen radio recombination spectra from galactic HII regions? *J. Phys. B*, 46(17):175702.

Hoang-Binh, D. (1972). The broadening of radio recombination lines emitted by HII regions. In *Les Spectres des Astres dans l'Infrarouge et les Microondes*, pages 367–370.

Hoang-Binh, D. (1990). An exact calculation of hydrogenic radial integrals and oscillator strengths, for principal quantum numbers up to $n \approx 1000$. *A&A*, 238:449–451.

Höglund, B. and Mezger, P. G. (1965). Hydrogen emission line $n_{110} -> n_{109}$: detection at 5009 megahertz in galactic HII regions. *Science*, 150:339–340.

Jeans, J. H. (1905). On the partition of energy between matter and ether. *Phil. Mag.*, 10:91.

Kaplan, S. A. and Pikel'ner, S. B. (1970). *Matter in space - The interstellar medium.* Translated from the Russian edition: Harvard University Press, Cambridge, MA.

Kardashev, N. S. (1959). On the possibility of detection of allowed lines of atomic hydrogen in the radio-frequency spectrum. *AZh*, 36:838, English translation: 1960 Soviet Ast. 3:813.

Kielkopf, J. F. (1973). New approximation to the voigt function with applications to spectral-line profile analysis. *J. Opt. Soc. Am.*, 63:987–995.

Kirchhoff, G. (1860). Ueber das verhältniss zwischen dem Emissionsvermögen und dem absorptionsvermögen der körper für wärme und Licht. *Ann. der Phys.*, 185:275–301.

Landau, L. D. and Lifshitz, E. M. (1980). *Statistical Physics, Part 1*. Reed Educational and Professional Publishing, Oxford, 3rd edition.

Lilley, A. E., Menzel, D. H., Penfield, H., and Zuckerman, B. (1966). Detection of hydrogen emission lines $n_{159} -> n_{158}$ and $n_{157} -> n_{156}$ in galactic H II regions. *Nature*, 209:468–470.

Liszt, H. (1997). Recovering line profiles from frequency-switched spectra. *A&AS*, 124:183.

Lockman, F. J. and Brown, R. L. (1975). The radio recombination line spectrum of orion a - observations and analysis. *ApJ*, 201:134–150.

Lorentz, H. A. (1906). The absoption and emission lines of gaseous bodies. *Proc. Acad. Sci. Amsterdam*, 8:591–611.

Martinson, I. and Curtis, L. J. (2005). Janne Rydberg: his life and work. *Nucl. Instrum. Methods Phys. Res. B*, 235:17–22.

Maxwell, J. C. (1860). Illustrations of the dynamical theory of gases. Part I. On the motions and collisions of perfectly elastic spheres. *Philos. Mag.*, 4:19–32.

McGee, R. X. and Gardner, F. F. (1967). Hydrogen recombination lines 126$\alpha$ and 166$\alpha$ observed in galactic HII regions. *Nature*, 213:579.

Menzel, D. H. (1968). Oscillator strengths for high-level transitions in hydrogen. *Nature*, 218:756–757.

Menzel, D. H. and Pekeris, C. L. (1935). Absorption coefficients and hydrogen line intensities. *MNRAS*, 96:77.

Mihalas, D. (1978). *Stellar atmospheres*. W. H. Freeman, San Francisco, 2$^{nd}$ edition.

Minaeva, L. A., Sobel'Man, I. I., and Sorochenko, R. L. (1967). The discrete radio-frequency spectrum of atomic hydrogen. *AZh*, 44:995.

O'Dell, C. R. (1966). Electron temperatures derived from observations of low-density H II regions and planetary nebulae. *ApJ*, 143:168.

O'Dell, C. R. and Wen, Z. (1994). Postrefurbishment mission hubble space telescope images of the core of the orion nebula: proplyds, herbig-haro objects, and measurements of a circumstellar disk. *ApJ*, 436:194–202.

Oks, E. (2004). On the puzzle of the observed narrowing of radio recombination lines. *ApJ*, 609:L25–L28.

Peach, G. (1975). The width of spectral lines. *Contemp. Phys.*, 16:17–34.

Peach, G. (2015). Radio recombination lines of hydrogen. *J. Astrophys. Astron.*, 36:555–563.

Pikel'ner, S. B. (1973). Origin of the fluctuations of density and of the radial filaments in planetary nebulae. *Astrophys. Lett.*, 15:91.

Planck, M. (1901). Ueber das gesetz der energieverteilung im normalspectrum. *Ann. Phys.*, 309:553–563.

Rayleigh, J. W. S. (1900). Remarks upon the law of complete radiation. *Phil. Mag.*, 49:539.

Riley, K. F., Hobson, M. P., and Bence, S. J. (2006). *Mathematical methods for physics and engineering*. University Press, Cambridge, 3rd edition.

Rydberg, J. R. (1890). On the structure of the line-spectra of the chemical elements. *Phil. Mag.*, 29(179).

Sault, R. J., Teuben, P. J., and Wright, M. C. H. (1995). A retrospective view of MIRIAD. In Shaw, R. A., Payne, H. E., and Hayes, J. J. E., editors, *As-*

*tronomical Data Analysis Software and Systems IV*, volume 77 of *ASP Conf. Ser.*, page 433.

Scilab Enterprises (2012). *Scilab: free and open source software for numerical computation*. Scilab Enterprises, Orsay.

Seaton, M. J. (1959). Radiative recombination of hydrogenic ions. *MNRAS*, 119:81.

Seaton, M. J. (1964). Recombination spectra, III. *MNRAS*, 127:177.

Shaver, P. A. (1975). Theoretical intensities of low frequency recombination lines. *Pramana*, 5:1–28.

Simpson, J. P. (1973a). The effects of stark broadening in the radio recombination line temperatures. *Ap&SS*, 20:187–203.

Simpson, J. P. (1973b). Spectrophotometry of the orion nebula. *PASP*, 85:479.

Smirnov, G. T. (1985). Electron density in two HII regions, dr21 and w3, from stark-broadened radio recombination lines. *Pis'ma v Astron. Zh.*, 11:17–26.

Smirnov, G. T., Sorochenko, R. L., and Pankonin, V. (1984). Stark broadening in radio recombination lines towards the Orion Nebula. *A&A*, 135:116–121.

Sobel'man, I. I., Vainshtein, L. A., and Yukov, E. A. (1995). *Excitation of Atoms and Broadening of Spectral Lines*. Springer-Verlag, Berlin.

Sorochenko, R. L. and Borodzich, E. V. (1965). *Dokl. Akad. Nauk SSSR*, 163:603, English translation: 1966 Sov. Phys. – Dokl. 10, 588.

Stark, J. (1913). Observation of the separation of spectral lines by an electric field. *Nature*, 92:401.

Stepkin, S. V., Konovalenko, A. A., Kantharia, N. G., and Udaya Shankar, N. (2007). Radio recombination lines from the largest bound atoms in space. *MNRAS*, 374:852–856.

Strelnitski, V., Alexander, J., Gezari, S., Holder, B. P., Moran, J. M., and Reid, M. J. (2002). $H_2O$ masers and supersonic turbulence. *ApJ*, 581:1180–1193.

Strelnitski, V. S., Ponomarev, V. O., and Smith, H. A. (1996a). Hydrogen masers. I. theory and prospects. *ApJ*, 470:1118.

Strelnitski, V. S., Smith, H. A., and Ponomarev, V. O. (1996b). Hydrogen masers. II. mwc 349a. *ApJ*, 470:1134.

Tsivilev, A. P., Parfenov, S. Y., and Krasnov, V. V. (2016). The physical conditions of the central part of the orion a hii region by radio recombination line at 8 and 13. *Odessa Astron. Publ.*, 29:163.

van Atta, C. M., Hablanian, M. in Lerner, R. G., and Trigg, G. L. e. (1991). *Encyclopaedia of physics: vacuums and vacuum technology*. VCH Publisher, New York.

van de Hulst, H. C. (1945). Radio waves from space: origin of radiowaves. *Ned. Tijd. voor Natuurkunde*, 11:210–221.

Watson, J. K. G. (2006). Electron-impact broadening of radio recombination lines of atomic hydrogen. *J. Phys. B*, 39:1889.

Weisskopf, V. (1932). Zur theorie der kopplungsbreite und der stoßdämpfung. *Zeitschrift für Physik*, 75:287–301.

Weisskopf, V. and Wigner, E. (1930). Berechnung der natürlichen linienbreite auf grund der diracschen lichttheorie. *Zeitschrift für Physik*, 63:54–73.

Westpfahl, D. J. (1999). Spectral-line observing I: introduction. In Taylor, G. B., Carilli, C. L., and Perley, R. A., editors, *Synthesis Imaging in Radio Astronomy II*, volume 180 of *ASP Conf. Ser.*, pages 201–228.

Wilson, W. E., Ferris, R. H., Axtens, P., Brown, A., Davis, E., Hampson, G., Leach, M., Roberts, P., Saunders, S., Koribalski, B. S., Caswell, J. L., Lenc, E., Stevens, J., Voronkov, M. A., Wieringa, M. H., Brooks, K., Edwards, P. G., Ekers, R. D., Emonts, B., Hindson, L., Johnston, S., Maddison, S. T., Mahony, E. K., Malu, S. S., Massardi, M., Mao, M. Y., McConnell, D., Norris, R. P., Schnitzeler, D., Subrahmanyan, R., Urquhart, J. S., Thompson, M. A., and Wark, R. M. (2011). The australia telescope compact array broad-band backend: description and first results. *MNRAS*, 416:832–856.